Mengxiong ZHAO

Ultrasonic Fatigue Study of Inconel 718

Étude de la Fatigue Ultrasonique de l'Inconel 718

Thèse présentée et soutenue publiquement le 11/09/2018
en vue de l'obtention du doctorat de Mécanique, Génie Mécanique, Génie Civil
de l'Université Paris Nanterre
sous la direction de M. Olivier POLIT (Université Paris Nanterre)
et de M. Emmanuel VALOT (Université Paris Nanterre)

Jury :

Président	M. Thierry PALIN-LUC	Prof., Arts et Métiers ParisTech, France
Rapporteur	M. Jens BERGSTROM	Prof., Karlstadt University, Sweden
Rapporteur	M. Tieying WU	Prof., Nanjing University of Aeronautics and Astronautics, China
Examinatrice	Mme. Stéphanie SAILLY	Docteur, MECATEST, France
Examinateur	M. Vincent BONNAND	Docteur, ONERA DMAS/MCE, France
Directeur	M. Olivier POLIT	Prof., Université Paris Nanterre, France
Codirecteur	M. Emmanuel VALOT	Ass.Prof., Université Paris Nanterre, France

Acknowledgement

Abstract

Inconel 718 is widely used in many industries, for example for example aeronautics and energy, due to its high resistance to corrosion, oxidation, creep and high mechanical strength at elevated temperature. The total cycle of these mechanical components is up to $10^9 \sim 10^{10}$ during its whole lifetime. In the aeronautical context, a lot of work has been done on high-amplitude low-frequency loading including centrifugal force or thermal stress, neglecting low-amplitude high-frequency loading came from vibration of blade.

In this work, the very high cycle fatigue (VHCF) behaviour of Inconel 718 with self-heating phenomenon without any cooling is studied using ultrasonic fatigue system at 20 kHz. Acquisition system is improved using NI® capture card with LabView™ for monitoring the frequency, temperature, displacement and so on during all the tests. Keyence laser sensor with two probes at the top and bottom surfaces of the specimens is used to reveal the frequency and vibration mode. The difference of mean values between these two probes is the elongation of the specimen caused by self-heating phenomenon.

Three sets of materials with different heat treatment, As-Received (AR), Directly Aged (DA) and Directly Aged High Quality (DAHQ) are compared. The difference of grain size, phase, precipitate particle, etc. is investigated by metallographic micrograph using optical microscope (OM) and scanning electron microscope (SEM). Quasi-static uniaxial tensile property and cyclic stress-strain response is also proposed. The transition from cyclic hardening to cyclic softening appears after aged heat treatment. Finally, fracture surfaces are observed using optical camera and scanning electron microscope in order to identify the mechanism of fracture of Inconel 718 in the VHCF domain.

Keywords: Very High Cycle Fatigue (VHCF); Ultrasonic; Inconel 718; Heat Treatment; Self-heating

ii

Résumé

L'Inconel 718 est utilisé dans de nombreuses industries, par exemple aéronautique et énergétique, notamment pour sa haute résistance à la corrosion, à l'oxydation, au fluage et sa haute résistance mécanique à très haute température. Le nombre total de cycles de ces composants mécaniques s'élève à $10^9 \sim 10^{10}$ durant sa vie. Dans le contexte aéronautique, de nombreux travaux ont portées sur des chargements de grande amplitude à faible fréquence, comme les forces centrifuges ou les contraintes thermiques, en négligeant des chargements de faible amplitudes à très haute fréquence, du aux vibrations des pales.

Dans ce travail, on se propose d'étudier la fatigue à très grand nombre de cycles (VHCF) de l'Inconel 718 en utilisant des machines de fatigue ultrasonique, fonctionnant à 20 kHz. Le système d'acquisition utilise des cartes NI® et le logiciel LabView™ pour superviser la fréquence, la température, les déplacements durant toute la durée des tests. Des capteurs laser Keyence utilisant deux sondes pour les faces supérieure et inférieure de l'éprouvette permettent de capturer la fréquence et les modes de vibration. La différence entre les valeurs moyennes mesurées permet d'accéder à l'allongement de l'éprouvette, dû à l'auto-échauffement.

Trois types de matériaux avec différents traitements thermiques, AR, DA et DAHQ de l'ONERA sont comparés. La différence au niveau de la taille de grain, de la phase, des précipités, … est analysée par micrographie métallographique en utilisant un microscope optique (MO) et un microscope électronique à balayage (MEB). Le comportement en traction quasi-statique et sous chargement cyclique contrainte-déformation est aussi proposé. La transition entre durcissement et adoucissement cyclique apparait à l'issue du traitement thermique. Finalement, les surfaces de ruptures sont observées en utilisant des caméras optiques et un MEB afin d'identifier les mécanismes de ruptures de l'Inconel 718 dans le domaine de la fatigue à très grand nombre de cycles.

__Mots-Clés:__ Fatigue à très grand nombre de cycles; Ultrasonique; Inconel 718; Traitement thermique; Auto-échauffement

iv

Nomenclature

BCC	Body Centered Cubic
CDM	Continuum Damage Mechanics
CGR	Crystallographic Growth Region
EBSD	Electron Back Scatter Diffraction
EDS / EDX	Energy Dispersive X-ray Spectroscopy
FCC	Face Centered Cubic
FCGR	Fatigue Crack Growth Rate
FCP	Fatigue Crack Propagation
FGA	Fine Granular Area
GBF	Granular Bright Facet
HCF	High Cycle Fatigue
LCF	Low Cycle Fatigue
NMI	Non Metallic Inclusion
ODA	Optical Dark Area
OM	Optical Microscope
PSB	Persistent Slip Band
SEM	Scanning Electron Microscope
SIF	Stress Intensity Factor

TCP	Topologically Close Packed
TEM	Transmission Electron Microscope
VHCF	Very High Cycle Fatigue
WDS	Wavelength Dispersive X-ray Spectroscopy

Notation

a	Fatigue Crack Length
c	Wave Velocity in the Material
C_p	Heat Capacity at Constant Pressure
C_v	Heat Capacity at Constant Volume
$[C]$	Resistance Matrix
d	Energy Dissipation
d_1	Intrinsic Dissipation
d_2	Thermal Dissipation
D	Damage Variable
$\mathrm{d}a/\mathrm{d}N$	Crack Growth Rate
$e\,/\,\varepsilon$	Engineering / True Strain
$\dot{\varepsilon}$	Strain Rate
$E\,/\,E_d$	Elastic / Dynamic Modulus
f	Frequency
F	Force
G	Shear Modulus
$HB\,/\,HR\,/\,HV$	Hardness of Brinell / Rockwell / Vickers

K	Stress Intensity
K_{eff}	Effective Stress Intensity Factor
K_t	Stress Concentration Factor
K_{th}	Stress Intensity Factor Threshold
ΔK	Stress Intensity Range
$[K]$	Stiffness Matrix
$[M]$	Mass Matrix
N / N_f	Number of Cycles to Failure
ρ	Density
Q	Heat
R	Stress Ratio
γ	Shear Strain
s / σ	Engineering / True Stress
s_N	Fatigue Strength
σ_{-1} / σ_f	Fatigue Endurance Limit Strength
σ_a	Stress Amplitude
σ_b / σ_{UTS}	Ultimate Stress
σ_k	Failure Stress
σ_m	Mean Stress
$\sigma_y / \sigma_{0.2}$	Yield Stress

t	Time
T	Temperature
τ	Shear Stress
υ	Poisson's Ratio
ω	Angular Frequency
Δ	Laplacian Operator
∇	Hamiltonian Operator

$$\Delta = \nabla \cdot \nabla = \nabla^2$$

x

Content

Introduction

Background

With the modern industry developing, the total cycle of mechanical component has already up to $10^9 \sim 10^{10}$ during whole lifetime. Aircraft engine is an example of the most advanced mechanical system, with five major components: intake, compressor, combustor, turbine and nozzle[1]. Intake and low pressure compressor have worked in the normal temperature surrounding, but the high pressure compressor, combustor chamber, blade and disk of turbine have sustained very high temperature, especially for turbine disk. The flange of turbine disk has endured 550~750ºC usually, while the temperature at the center of disk is about only 300ºC.

High temperature superalloy is widely used in the aeronautic applications, due to its high resistance to corrosion, oxidation, thermal creep deformation and high mechanical strength at even elevated temperature. Variety of superalloy is always applied together at same time, based on the different kind of requirement at the different part of engine. Total mass of all the superalloy achieves 40~60% in the developed engine, and it has occupied the irreplaceable position in the aeronautic industry.

Compressor: **Combustor:**   **Turbine:**
Incoloy   Inconel   Inconel
Inconel   Nimonic   Nimonic
Udimet   Udimet   Rene
                                            Waspaloy
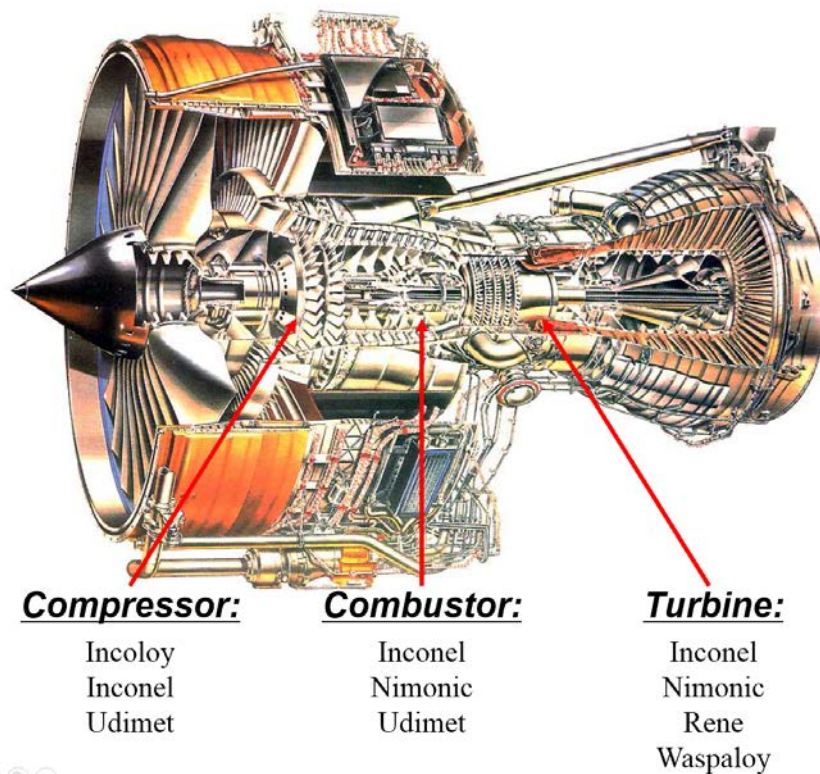
Figure 1 High Temperature Superalloy using in the Aircraft Engine[1]

The turbine disk is endured high-amplitude low-frequency load, mainly including: centrifugal force caused by high rotatory speed, thermal stress caused by high temperature gradient, tensile force transferred from rotary blade and so on. The loading cycle of these force is same with the working cycle of the airplane.

And it also endures low-amplitude high-frequency loading came from the vibration of blade during all the processing of operation, especially under the unsteady situation of takeoff and landing.

The aeronautic accident induced by structure failure is common occurrence. The importance of experimental test and accurate life prediction for turbine can be exemplified by the accident occurred at Los Angeles in 2006. The left engine of Boeing 767 airplane exploded during high powered ground run. Investigation showed that the 1st stage turbine disk had failed from an intergranular fatigue crack. "One piece of disc, which initially bounced off the ground before penetrating the airplane, completely severed the airplane's left-hand kneel beam and partially severed, the right hand kneel beam before exiting the airplane and becoming lodged in No.2 engine's exhaust duct"[2].

Therefore, to ensure the reliability and safety of structure, the investigation on very high cycle fatigue (VHCF) behaviors is of great importance.
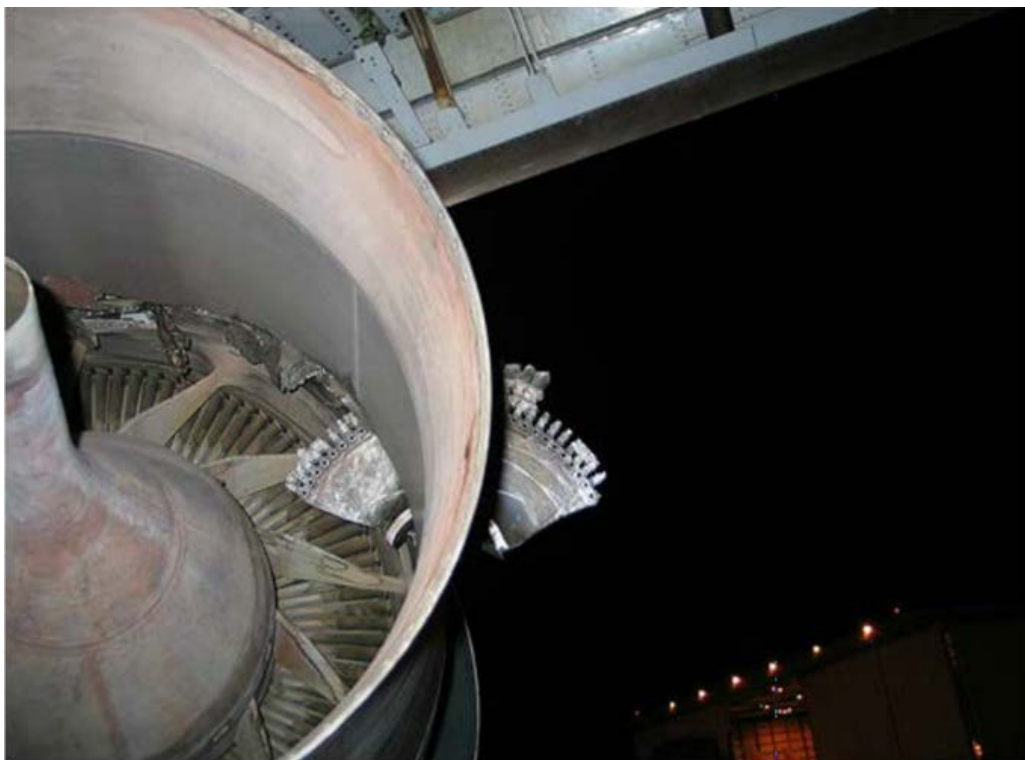
Figure 2 Failure of Turbine Disk in Los Angeles Engine Accident

Objective

In order to investigate the VHCF properties of nickel based superalloy Inconel 718 with ultrasonic loading at 20 kHz, the main objective of this project can be listed as follows:

1. Acquisition system could be improved for monitoring frequency, temperature, displacement, etc. during all the tests. Resonance frequency and vibration mode of specimen should be validated.

2. Physical and mechanical properties of Inconel 718 after different heat treatment could be compared. Microstructure of these material could be analyzed for the understanding of property difference.

3. Self-heating phenomenon of Inconel 718 with ultrasonic loading at 20 kHz could be investigated. Surface stationary temperature distribution and energy dissipation could be calculated.

4. The relation between loading Stress and Number of cycles (S-N Curve) of Inconel 718 at 20 kHz with self-heating phenomenon up to VHCF regime could be carried out. Fatigue life could be predicted to lower and higher cycles.

5. Influence factors on the fatigue life, like heat treatment or loading mode, could be analyzed. Self-heating phenomenon and very high cycle fatigue property could be correlated.

6. Mechanism of crack initiation could be disclosed. Proposal for delay the crack initiation, as well as improve the life time of the material Inconel 718 at very high cycle regime could be carried out.

Manuscript Structure

This thesis investigates the VHCF behavior of Inconel 718 with self-heating using ultrasonic test system at 20 kHz, and focus on the role of microstructure on the fatigue crack initiation life and mechanism up to VHCF range. The main structure of this thesis is listed as follow:

Chapter I

Development and mechanism of fatigue is summarized simply. Property of nickel based superalloy is shown generally. Fatigue research of Inconel 718 done by another team previously is concluded in detail.

Chapter II

Test device is introduced entirely. Theoretical calculation determines the geometry of vibration parts. Numerical simulation validates the design of specimen and obtains the influence of self-heating phenomenon.

Chapter III

Microstructure of 3 different series of Inconel 718 is taken using optical camera (OM) and scanning electron microscope (SEM). Physical properties, monotonic and cyclic behaviors are compared.

Chapter IV

Stationary temperature increase due to self-heating phenomenon is presented. S-N curve has been done up to very high cycle regime. Fracture surfaces morphology with short and long life specimen are compared.

Chapter V

Fracture mechanism under ultrasonic loading is studied. The influence factors on the fatigue life, like test temperature and loading mode, are disclosed. Fatigue life prediction and dissipated energy calculation are presented.

Chapter I Literature Review

1.1 Development of Fatigue

In 1829, Albert observed the failure of iron mine hoist chains arising from repeated small amplitude loadings. He built a machine which repeatedly loaded a chain and studied anew phenomena. That such fracture was not associated with an accidental overload, but was dependent on load and the number of repetitions of load cycles. The first publication about repeated loads effect on material strength was done in 1837[3].

The term "Fatigue" was introduced by French engineer Poncelet in 1839[4]. He describes metals as being tired under repetitive loading and since that time the term "Fatigue" has become a commonly used.

At that time, design of machines did not take into account an influence of repetitive loading that led to numerous fatigue failures in different engineering applications. Many disastrous rail road accidents were occurred. One of the most dramatic and well known catastrophe on railways due to fatigue was crash of passenger train on the Versailles railway track in 1842[5]. It has been shown, that fatigue fracture surface shows an evidences of brittle cracking. The common hypothesis to explain that was an idea about changing in iron structure under repeated loads[6]. It was erroneously assumed, that under repetitive loading a fibrous structure of iron turns to crystalline. Fracture surface of axis under monotonic tensile did not show any evidence of brittle cracking in spite of cyclic preloading.

Important work on fatigue in railway axis was published by Scottish engineer Rankine in 1843[7]. He reported that fatigue rapture of railway axis under repeated loads starts from a small surface crack. He found, that such crack mainly occurs at the section changes of axis. It is the first publication about role of stress concentration in fatigue.

The first systematic investigation on fatigue behaviour of materials is German engineer Wöhler. He studied steel shaft fatigue strength under cyclic loads and proposed Stress versus Number curve to describe the fatigue behavior in 1852[8, 9]. The first results has shown that spectrum of load consists of small amplitude loading mixed with a significant amplitude loads due to imperfection of railway track. He assumed that critical destructive influence on axis is related to significant amplitude loads. He implicitly suggested design for finite fatigue life taken into

consideration even the scatter of fatigue life. In 1870, he presented a final report of his fatigue investigations from 1858 to 1869, represented his test results in the form of tables[10].

Gerber had developed fatigue design method with considering efforts of mean stress in 1874[11]. Spangenberg plotted them as curves, although in the unusual form of linear abscissa and ordinate in 1875[12]. The S-N curves were called "Wöhler curves". Basquin found that S-N curve of metallurgic materials is in double logarithmic coordinates, and presented a linear relationship in 1910[13].

Most of fatigue tests were carried out on full-scale elements and aimed to decrease an accidents in different industries. The "fatigue" began to develop as a metal problem from 1900. Fundamental step in this kind of development was made by Ewing[14, 15]. They carried out fatigue tests on iron with periodic observations on specimen's surface by microscope. Results has shown that repeated loading initiates so-called "slip-lines" or "slip-bands" in individual crystals.

Development of the theory of dislocations allowed to explain the plasticity of crystals in terms of dislocation by Taylor and Polanyi in 1934[16-18]. Orowan applied theory of dislocation to fatigue in 1939[19]. Dislocation theory was also employed for explaining as crack initiation by Mott in 1958 [20], as well a crack propagation by Head in 1953[21].

Langer has separated fatigue life into the crack initiation and propagation phases in his work about fatigue damage accumulation in 1937[22]. He suggested a damage sum of 1 for each phase, however for application of this hypothesis crack propagation curves were necessary. Miner proposed linear cumulated damage theory in 1945[23].

Irwin has introduce a stress intensity factor (SIF) for analysis of stress field around the crack tip in 1957[24]. It was a milestone in developing of fracture mechanics. Cyclic strain hardening were credible after detection of striation by Ryder in 1958[25]. Fatigue striation has shown, that crack growth is cycle-by-cycle process.

In 1961 Paris have introduced stress intensity factor for the correlation between the crack growth rate, and the stress intensity factor range. Soon afterward this equation was called as "Paris law"[26, 27].

Plastic strain seems to be more sensitive measurement of life than the nominal stress. This idea was developed by Coffin in 1962[28] and Manson in 1964[29], introduced as "strain controlled" model of S-N curve. Plastic strain is key drive parameter instead nominal stress.

The fundamental contribution to an improved calculation of crack propagation under service like amplitudes was supplied by Elber in 1970[30, 31]. The tip of a growing fatigue crack could be closed at a positive tensile stress ("crack closure effect"), that a load cycle is only effective in driving the growth of a fatigue crack if the crack tip is fully open and defined effective range of stress and SIF.

Experimental studies on the crack growth under low ΔK values has shown that micro-cracks or short-cracks can develops even under ΔK_{th}. The first relevant paper about such micro-cracks growth was published by Pearson in 1975[32]. He has shown that these cracks occur as micro-cracks in the beginning of the fatigue life starting at the material surface or just subsurface. Micro-cracks are growing much faster than large macro cracks at nominally similar ΔK by Miller in 1982[33]

Generally, S-N curve consists of two straight parts: one inclined and one practically horizontal. The horizontal asymptote of the S-N curve is called the fatigue/endurance limit. Some materials, like aluminum and copper, eventually fail even under small stress amplitudes after sufficiently high number of cycles. Even materials known as material with distinct asymptote can be failed by alternating stress below "fatigue limit" by Naito in 1984[34]. Prof. Bathias have stated for the first time that there is no 'fatigue limit' in metallic materials in 1999[35] and 2001[36].

The recent development of experimental techniques, like in-situ tests under simultaneous scanning electron microscope observations by Provan in 1987[37, 38]; X-ray micro-tomography by Buffière from 2003[39-42], suggests further understanding of fundamental fatigue nature at micro or nano scale levels and thermal and dissipative effects by Chrysochoos from 1996[43-46].

According to the magnitude of cyclic stress loading, fatigue research can be divided into stress fatigue and strain fatigue. When maximum cyclic stress is higher than the yield stress of material, the change of strain is more significant than stress during the test. It is more appropriate to choose the strain as parameters to describe the fatigue property. The total life is always less than 1000 (or 10000) in this situation, so that the strain fatigue is also called low cycle fatigue (LCF). LCF test is controlled by deformation (strain). While, when maximum cyclic stress is lower than the yield stress of material, the change of stress is more significant. The total life is always more than 10000 cycles, so that the stress fatigue is also called high cycle fatigue (HCF). HCF test is controlled by force (stress).

Normally, fatigue failure cycles under $10^{4\sim5}$ cycles have been considered as low cycle fatigue (LCF), and between 10^5 and 10^7 is called as high cycle fatigue (HCF), while total cycles over 10^7 is very high cycle fatigue (VHCF), shown in Figure 1.1.

According to observation and literature, several mechanisms are involved depending of the number of cycles to failure[47].
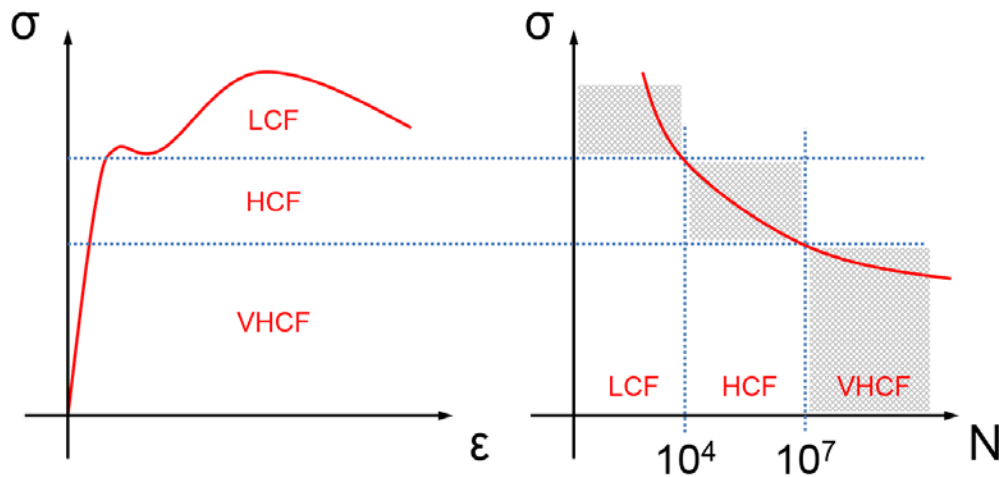
Figure 1.1 Comparison of Stress and Total Cycle between LCF, HCF and VHCF

1.1.1 VHCF (Ultrasonic)

In the past, the "fatigue limit" is defined as the stress value which it does not exist risk that a failure occurs at some number of cycles. In the ASTM standard is defined at 10^6 cycles for structural steels. On the contrary, the "fatigue life" is a term that indicates the time or number of cycles that a material will resist at certain stress level and the "fatigue strength" is the stress level at which a material fails at a given number of cycles.

Conventional design standard bases their recommendations still on the common prejudice that an "endurance limit" exists. However, several investigations prove clearly that in the high-cycle regime a decrease of fatigue strength with increased number of cycles still occurs, even if corrosion or temperature effects are excluded[48]. In 1984 Japanese researchers found that metallic materials as low alloy steels can fail in fatigue after 10^7 cycles[49].

Nowadays, in several industries, such as aeronautics, high speed train, marine or ground transportation, there are several structural elements that are subjected to recurrent loads of high frequency and low amplitude, many times more than 10^9 cycles during their work duration. An example can be the life of the motor of an automobile whose components operate in the range of 10^8 cycles. For the big motors of ships or high-speed trains the life can reach 10^9 cycles, while in the turbines of airplanes, the fatigue life is around 10^{10} cycles[50].

Gigacycle or Very High Cycle Fatigue (VHCF) is one of the fatigue range corresponding to very long fatigue life[50]. Typical loading amplitudes of VHCF range is well below yield stress of material and lying near to the classical "fatigue limit" (with a tendency to be slightly below).

Most of traditional fatigue test machine works limited by several hundred Hz, not suitable for experimental investigation of VHCF range. High time consuming and cost of such test up to 10^9 cycles made conventional testing machine unacceptable for gigacycle testing. The possible solution to make fatigue tests reasonable is increasing a loading frequency.

In 1950, Mason[51] introduced ultrasonic resonance fatigue testing at Bell Telephone Laboratories by using Titanium driver attached to an exponential Brass horn. This high amplitude device was applied to measured wear in relays and in studying internal friction and fatigue in metals, the frequency was 20 kHz. As a result, ultrasonic methodology has found increasing applications in exploring fatigue lives at very high cycle domain[52, 53] and in investigating threshold crack propagation behavior[54-57], where experiments by conventional machines are difficult, time-consuming and expensive to conduct.

The main idea of this concept is cyclic loading of specimen at one of its own natural frequency. In this case the geometry of all loading elements of testing system including specimen should be designed at the same frequency. The analytical solution for this problem is built based on the theory of isotropic elastic waves propagation in elastic body. The differential equation in a Cartesian coordinate system are following Equation (1.1):

$$
\begin{cases}
\rho \dfrac{\partial^2 u}{\partial t^2} = \dfrac{E}{1+v}\left(\dfrac{1}{1-2v}\cdot\dfrac{\partial e}{\partial x} + \nabla^2 u\right) \\[3mm]
\rho \dfrac{\partial^2 v}{\partial t^2} = \dfrac{E}{1+v}\left(\dfrac{1}{1-2v}\cdot\dfrac{\partial e}{\partial y} + \nabla^2 v\right) \\[3mm]
\rho \dfrac{\partial^2 w}{\partial t^2} = \dfrac{E}{1+v}\left(\dfrac{1}{1-2v}\cdot\dfrac{\partial e}{\partial z} + \nabla^2 w\right)
\end{cases}
\tag{1.1}
$$

where (u,v,w) are the displacement change along (x,y,z) respectively, (E,ρ,v) are the Young's modulus, density and Poisson's ratio. e is volume dilatation which can be expressed in the next form (1.2):

$$
e = \frac{\partial u}{\partial x} + \frac{\partial v}{\partial y} + \frac{\partial w}{\partial z} = \varepsilon_{xx} + \varepsilon_{yy} + \varepsilon_{zz}
\tag{1.2}
$$

According to the elastic wave theory the following two types of wave may exist in an infinite isotropic elastic body: longitudinal and transverse waves. The velocities of these waves are not the same and can be expressed in terms of material constants, shown in Figure 1.2.
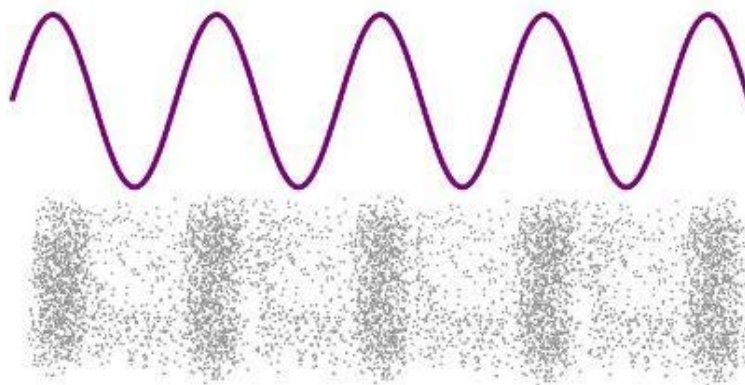
Figure 1.2 Transverse and Longitudinal Wave

For the transverse wave (for example light wave), the velocity of wave propagation shown as Equation (1.3):

$$c_{tran} = \sqrt{\frac{E}{\rho(1+\nu)}} \tag{1.3}$$

A longitudinal wave has a curl of displacement field zero (for example sound wave) and the velocity of wave propagation is (1.4):

$$c_{long} = \sqrt{\frac{E(1-\nu)}{\rho(1+\nu)(1-2\nu)}} \tag{1.4}$$

The major advantage of using ultrasonic fatigue testing method is its ability to provide fatigue limit and near threshold crack propagation data within a reasonable length of time. The development of ultrasonic fatigue testing method brought advantage such as not only rapidly and effectiveness in fatigue testing but also clarification of fatigue behavior in very high cycle regime. Several laboratories have made their own machine and design practical test procedures. Laboratories of Willertz in the US[58], Stanzl in Austria[59], Bathias in France[60] are leading laboratories in this field.

Furthermore, it is known that the fatigue crack initiation process becomes increasingly important with the extension of fatigue life. The fraction of crack initiation in total fatigue life is increasing with decreasing a loading amplitude[61]. But in case of internal crack initiation and growth it was difficult to experimentally prove this tendency. Just with developing of subsurface crack growth model by Bathias and Paris, it became possible to estimate analytically the fraction of crack growth and initiation in total fatigue life. Bathias and Paris has shown, that crack initiation is VHCF can reach more than 99%[62]. The developing of non-destructive control methods (infrared technique) allowed to experimentally confirm this result. Thus, the crack initiation stage consumes most of the total fatigue life and, therefore, can be assumes as a main subject for investigations in VHCF.

However, current understanding of ultrasonic fatigue has been physically long crack oriented, and the influence of ultrasonic frequency on small crack behavior has not adequately integrated into the prediction of fatigue damage. It is dangerous by considering the facts that initiation and the growth of small cracks dominate fatigue lives in metallic materials, especially at gigacycle fatigue life region[63].

1.1.2 Full S-N Curve

Fatigue was continuous process of material degradation under cyclic loading. The fatigue damage accumulated corresponds to the initiation and propagation of the crack originated by cyclic loading on the material. With the changing of stress level, the number of cycles to failure can passed over several orders of magnitude. The abscissa axis of S-N curve was always plotted by logarithmic for this reason. The ordinate axis was stress amplitude. In case of asymmetric loading, maximum stress was usually used here.

The S-N curve was statistical average and associated with scatter of results. The full S-N curve was commonly used for fundamental investigation on the fatigue behaviour of material, because it allowed general view on material behaviour in all fatigue domains. Several different full S-N curve approaches are existed nowadays, shown in Figure 1.3.
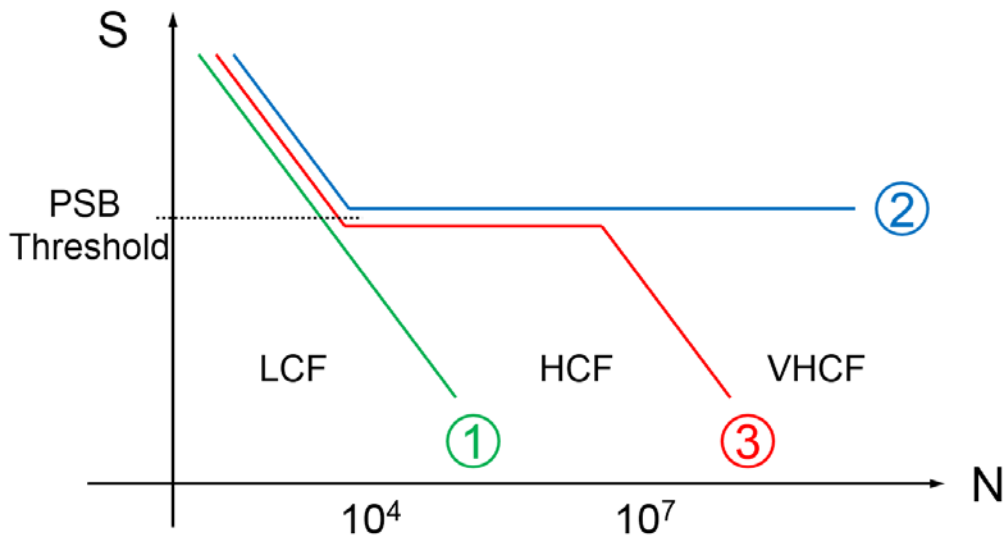
Figure 1.3 Three Different Kinds of S-N Curves

● Continuous Decreased:

The total life of material increased continuously as the loading stress decreasing. There was always fatigue failure after certain number of cycles. no matter the level of loading stress.

● Decreased Straight:

For some kinds of material, like carbon steel or low alloy steel, it seems that fatigue failure did not occur under the distinctive stress level. Corresponding to the S-N curve achieved horizontal asymptote when the stress was enough low, it called as the "Fatigue Endurance / Limit".

● Stepwise Decreased:

The resent investigation in VHCF range has shown that there is no endurance fatigue limit[35]. The material failure occurred after enough high loading cycles. The S-N curve shown distinct knee between two decreasing parts. The mechanism of failure was different associated with the number of cycles.
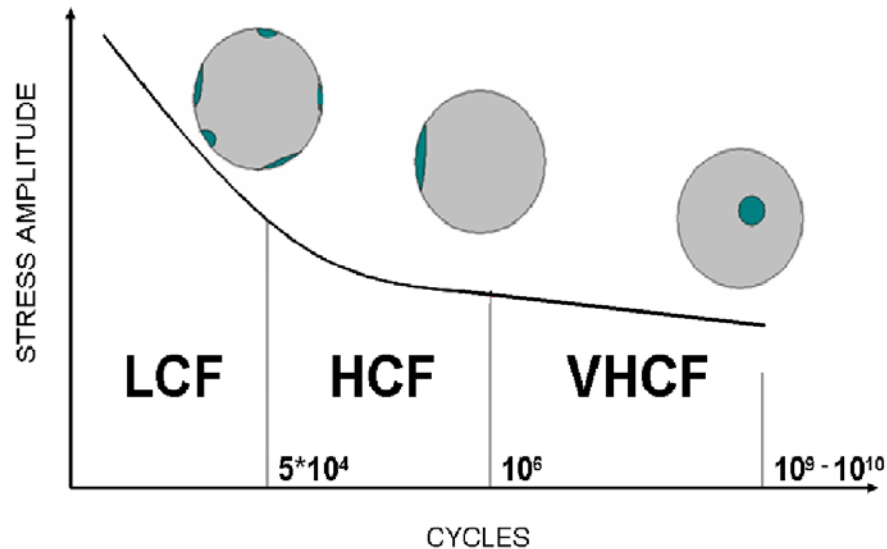
Figure 1.4 Regimes of Fatigue with Crack Initiation Character[36]

Under the high amplitude loading, almost whole test section experienced plastic deformation, the plastic strain is significant. The grains close to the surface were less constrained and plastic deformation was more preferable at the surface. Several points at the surface achieved critical state simultaneously.

With decreasing the loading amplitude, just few grains were involving in plastic deformation process. The plastic deformation localized in PSB or the stress concentration site. Only one initiation occurred on the surface of the specimen.

When the loading amplitude decreased below the conventional "fatigue limit", there was no plastic strain under this kind of loading condition theoretically. However, the fatigue damage still occurred in material leading to the final crack. Micro plastic strain appeared and accumulated around the defect of the material (porosity, cavity, non-metallic inclusion, grain boundary, etc.). The probability of internal defect was higher compared to the surface location, shown in Figure 1.4.

1.2 Mechanism of Fatigue

Generally, the fatigue fracture behavior includes 3 stages: cracks initiation (nucleation and primary growth), cracks propagation and final failure. French proposed the "critical damage curve" in 1933[61], shown in Figure 1.5.
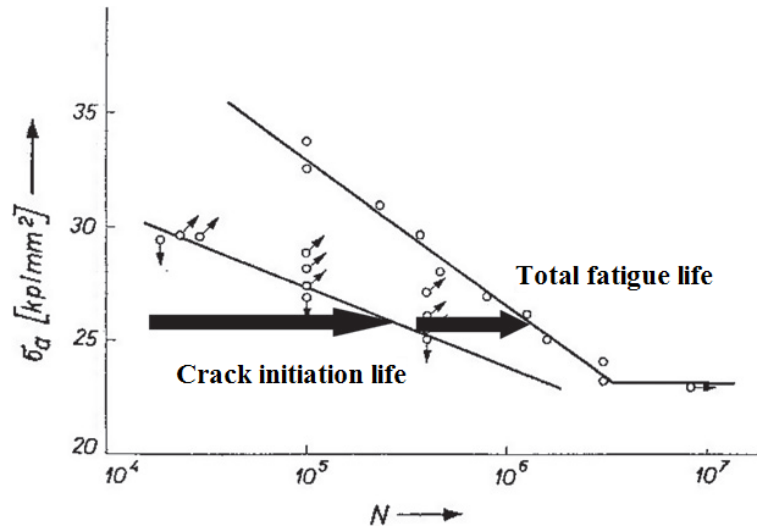
Figure 1.5 Example of French Curve for Carbon Steel[61]

The French curve obtains two stage fatigue experiment: one is aimed to determine a number of cycles which necessary for the initiation of a crack until critical length; the other stage is obtaining S-N curve. The number of cycles which separate the French curve from the S-N curve at a particular stress level is considered to be the period of crack propagation after micro-cracks of critical size have been initiated.

In 1937 B.F. Langer also proposed to separate crack initiation and crack propagation stages Thus, since the, the fatigue in metals became a two stages process, fatigue crack initiation and propagation[22].

The crack initiation stage is associated with forming a critical discontinuity in material structure (crack like defect). The formation of such defect depends of numerous factors, such as loading amplitude, environment, type of material, etc. When a critical size of discontinuity is reached, the crack starts to propagate.

The duration of these stage is not the same and moreover for crack initiation and propagation stages it depends of stress amplitude. The period of crack propagation occupies a large fraction of fatigue life in LCF range. According to Bathias, the fraction of fatigue crack initiation in HCF can be more than 90 % of total fatigue life and reach even 99 % in case of VHCF range[50].

Development of material strength design is divided into different stages:

● Material Mechanics (linear elasticity or elastoplasticity):

The basic hypothesis of material mechanics is that research object treated as ideally homogeneous continuous medium without any defect. The judgment of failure is based on 4 classic theories: maximum normal stress theory, maximum shear stress theory, maximum strain energy theory, and maximum distortion energy theory. Maximum distortion energy theory is also known as von Mises Hencky theory. The total elastic energy due to strain can be divided into two parts: one causes change in volume, and the other part causes change in shape. Failure will occur when the distortion energy per unit volume due to the applied stresses in a part equals the distortion energy per unit volume at the yield point in uniaxial testing.

● Fracture mechanics:

Fracture mechanics has developed by Griffith[64], Irwin[24] from 1920, concerning with the study of the propagation of cracks in materials. The basic hypothesis of fracture mechanics is that macro cracks exist in the material, while the medium around these cracks keep still uniform and continuous. Fracture mechanics consider only the macroscopic defects. The processing of micro damage to macro crack has been neglected.

● Damage Mechanics:

Continuum Damage mechanics (CDM) has provided a method for estimating the damage. It has originally introduced by Kachanov[65], Rabotnov[66] in 1960, and developed by Lemaitre[67, 68] and Chaboche[69-71] after 1980. The aim of damage mechanics is to analyze the evolution of micro cracks, microstructure voids, for making engineering predictions about the initiation, propagation, and fracture of materials without resorting to a microscopic description that would be too complex for practical engineering analysis.

● Failure Mechanics:

The discipline that combines damage mechanics and fracture mechanics becomes the Failure Mechanics.

1.2.1 Crack Initiation

The fatigue crack initiation is continuous physical process of creation a critical discontinuous in metal under cyclic loading. The fatigue in metals was associated with changes in the internal structure of the component or specimen.

Founding of the permanent slip bands (PSB) at the surface of material subjected to the cyclic loading made clear, which such changes in structure are due to plastic deformation. In its turn, the plastic deformation in metals is commonly explains by dislocation motion. Up to nowadays, the fatigue crack initiation process is explaining by accumulation of plastic deformation.

Typically, the process of crack initiation in terms of dislocations is discussed for two types of materials: Type I ductile single phase metal without defect and Type II metallic material containing internal defects (such as non-metallic inclusions or pores) [72, 73].

Fatigue in Type I material is associated with forming PSB. A model of PSB formation has been proposed by Essmann, Gosele and Mughrabi (EGM model), shown in Figure 1.6. According to this model, due to dislocation motion within PSB, an extrusion appears at the material surface. Then with continued cycling, they become roughened by gliding screw dislocations. Extrusions and roughening of the material at the surface within the PSB's are due to slip irreversibility, without which it is difficult to imagine that there could be any kind of fatigue damage.

Under further cyclic loading, intrusions are forming within initial extrusion and by its edges. In fact, extrusions and intrusion at the surface of single crystals are areas of stress concentration at which cracks may nucleate. Thus, in a single crystal of pure FCC material fatigue crack initiate at the surface within at intrusion or permanent surface marks (extrusion / intrusion). In the case of polycrystalline materials, as intergranular, as well transgranular crack initiation can be realized.
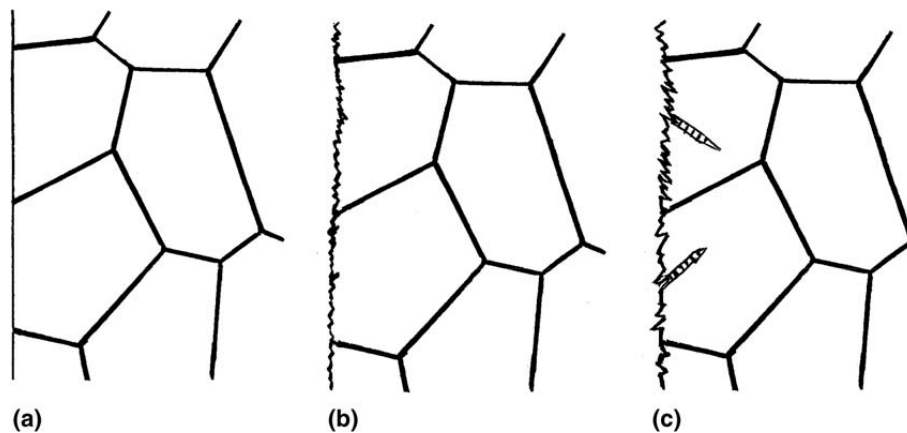
Figure 1.6 Ductile Single Phase PSB from Material Surface[74]
(a) Initial state, (b) Surface roughening (c) PSB formation and micro crack

12

In the case of type II metallic material containing significant internal defects, like BCC material, the sliding process is more difficult compared to FCC material. It is related to the density of atoms in sliding planes of the structure, not a close packed lattice. In materials with very low ability for sliding process, another mechanism of plasticity is activated, twinning.

The crack initiation stage in the type II material is highly dependent on the loading amplitude and life cycles:

At high loading amplitudes (LCF) usually many crack initiation sites can be detected at the surface, originating from PSBs.

At lower loading amplitudes (HCF), similar crack initiation sites can be detected at the surface but they are fewer in number than LCF conditions.

At very low loading amplitudes (VHCF), cyclic slip at the surface is very small and does not give rise to surface roughening thus there is almost no crack growth from the surface and cracks usually form at internal inclusions, which act as stress raisers and promote more slip.

Accumulation of plastic deformation is a reason for fatigue crack nucleation. Under high amplitude, numerous sliding system are simultaneously activated. Almost all material is under plastic deformation. While, under lower loading amplitude, foreign impurity particle, a surface imperfection or a plastically deforming grain surrounded by elastic grains can act to cause local stress concentrations that will lead in a similar way to the creation and growth of small cracks[75]. The nucleation of fatigue cracks at grain boundaries also occurs under the influence of embrittling environments which preferentially attack grain boundaries and the particles, if any, on them[76]. At elevated temperatures where grain boundary cavitation and sliding are promoted, crack nucleation at grain boundaries can also occurs. Intergranular fracture is also commonly observed in brittle solids due to the residual stresses induced by thermal contraction mismatch between adjacent grains or to the presence of brittle phases on grain boundary.

Crack initiation in VHCF

The nucleation mechanism at the microscopic scale is almost the same whatever the fatigue regime, but what changes is the localization of the permanent slip bands. As the likelihood of getting a defect within a volume is higher than the chance of a defect at the surface envelope, internal initiation under gigacycle fatigue can easily be understood.

Type I materials which exhibit surface failure initiation in VHCF regime, typically consist of single phase FCC metals such as copper which do not contain inclusions. Above the PSB threshold, fatigue cracks initiate at the sites of emerging PSBs at the surface, where the rapid formation of extrusions and gradually increasing surface roughness lead to fatigue crack initiation.

At VHCF regime, at stress levels below the conventional fatigue limit, fatigue failure can occur although the stress amplitude is too low for PSBs to develop, the accumulation of slightly irreversible random slip can result in a sufficient surface roughening to initiate surface fatigue cracks. At even lower stress amplitudes irreversibility of slip becomes negligible, leading to a final fatigue limit[74].

In contrast, type II materials, such as high strength steels which contain heterogeneities in the form of inclusions, pores and coarse second phase particles, display internal crack initiation in VHCF regime.

The transition between the different ranges is gradual along with some scatter and overlap. In VHCF regime, fatigue failure can occur at stress amplitudes below the conventional limit, originating mostly from internal defects. The materials can exhibit multi stage life diagrams would be categorized into two classes[77, 78], shown in Figure 1.7.
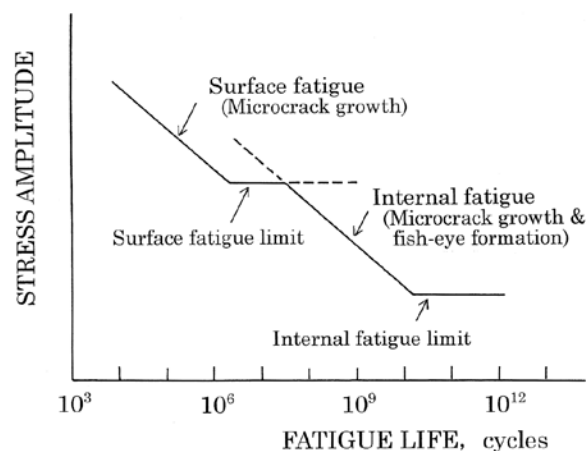
Figure 1.7 Concept of Two Fold S-N Curve[79]

In case of heterogeneous materials, the crack initiation is always associated with imperfections which lead to micro-structural changes by accumulation of repeated cyclic micro-strains. For such crack initiation the direct observation of fatigue damage accumulation process is not possible and the initiation mechanisms are reconstructed based on the observation of fracture surfaces.

The systematic investigations on the fracture surfaces for different materials made possible to distinguish the common for all materials patterns of subsurface crack named the "fish-eye"[50]. It has been found, that depends on the material a different micro-structural formation can be found in the center of the "fish-eye".

Typically, the non-metallic inclusion are surrounded by a characteristic area indicating fine granular morphology, shown in Figure 1.8. Based on the morphology taken by Sakai[80], this area is called FGA (Fine Granular Area). The same area was observed by Shiozawa[81], called it as GBF (Granular Bright Facet).
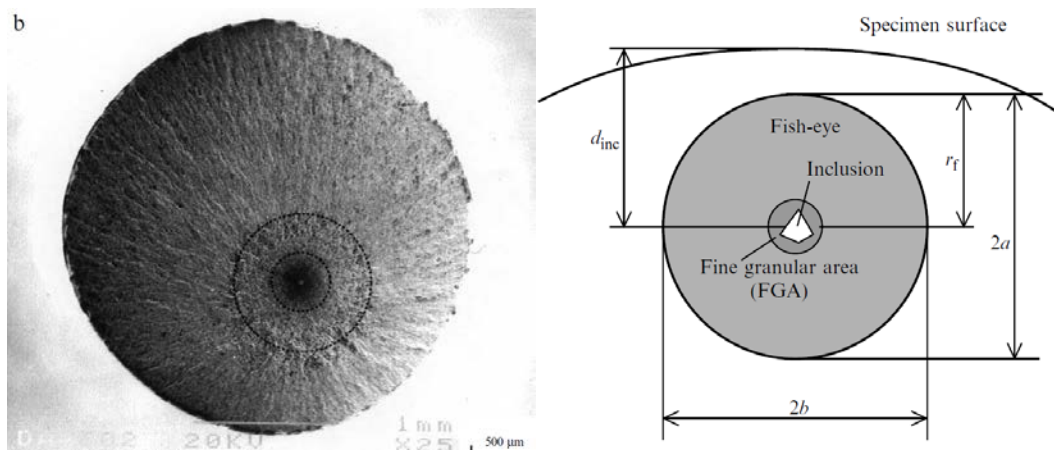
Figure 1.8 Morphology and Model of Fish Eye Crack

Concluding the section about fatigue crack initiation in VHCF, surface failure initiation exhibit in type I materials, and subsurface initiation from inclusions, pores and coarse second phase display in the type II materials.

However there is still exception. Yu investigated the VHCF mechanism of carbide free martensitic steel alloyed with Nb[82-84], finding almost all the initiation sites of the fatigue crack are located at the interior of the specimens. There are no visible inclusions found in the initiation sites in all broken specimens, which means interior non-inclusion-induced fatigue fracture is the main model of fatigue failure, shown in Figure 1.9.
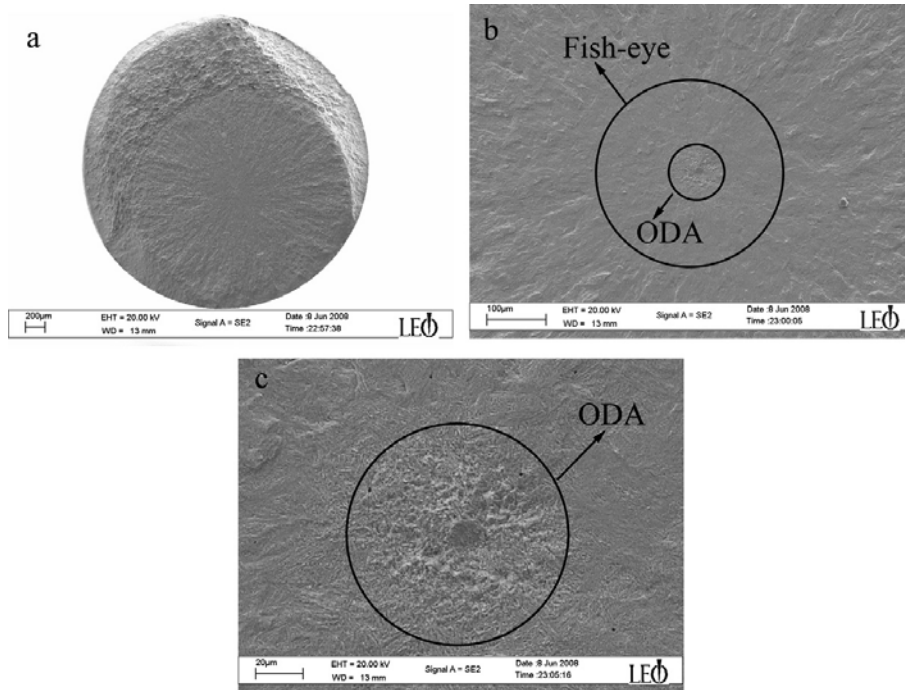
Figure 1.9 Interior non-inclusion induced fracture with Nb[82]

These figures show the typical fracture surface of the steel. The fish-eye and the details of ODA mark can be observed. In the center of ODA, there is no interior inclusion but a piece of flat area, which is evidently different with other steels whose fatigue crack are induced by inclusions. Soft or coarse structure induced fatigue crack should be responsible for the primary VHCF failure mechanism.

1.2.2 Crack Propagation

There are three ways of applying force to enable crack to propagate:

● Mode I: Opening mode, tensile stress normal to the plane of the crack;

● Mode II: Sliding mode, shear stress acting parallel to the plane of the crack and perpendicular to the crack front;

● Mode III: Tearing mode, shear stress acting parallel to the plane of the crack and parallel to the crack front.
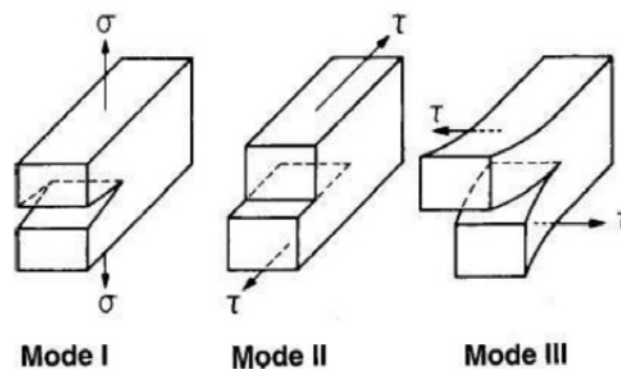
Figure 1.10 Three Mode of Fracture Propagation

Engineers consider the behaviour of two types of crack in metal fatigue in general, Stage I shear crack and Stage II tensile generated crack. Taking axial loading as a simple case, Stage I cracking in a single grain of a polycrystalline assembly eventually leads to Stage II cracking through the bulk of the material if failure is to occur. The push–pull fatigue limit and fatigue resistance of a material is given by the degree of difficulty that a Stage I crack experiences when attempting to propagate in a tortuous three-dimensional manner through several near-surface grains in order to become a Stage II crack.

Microstructural fracture mechanics describes this transition. It follows that the fatigue resistance of a material is enhanced if a large number of barriers is the misorientation of slip systems between grains that is witnessed at a grain boundary. That is the reason why a small grain size material has a greater fatigue resistance than a large grained. Another reason is that a small grain material usually has a higher yield strength, and so the reversed plasticity required to propagate the crack is of a lesser extent.

These two stages are so called stable propagation stage, after that the crack turns into instability growth Stage III, shown in Figure 1.11.
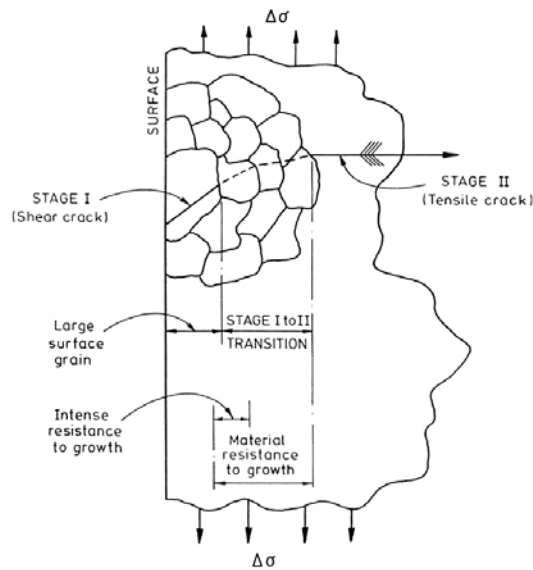
Figure 1.11 Fatigue Crack Growth under Axial Loading [85]

The Stress Intensity Factor (SIF) concept proposed firstly by Irwin in 1957[24]. After the stress intensity factor range for fatigue crack growth rate correlation by Paris[26], and the discovery of the fatigue crack closure phenomenon by Elber[31].
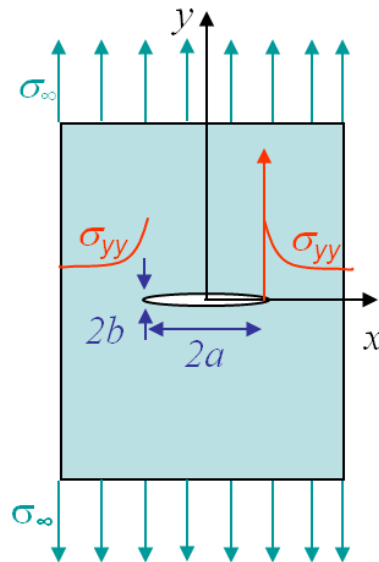
Figure 1.12 Ellipsoidal Mode I fracture in an infinite plate

The SIF for an assumed straight Mode I fracture in the infinite width flat board, shown in Figure 1.12, having a uniform stress field expressed as Equation (1.5):

$$K_I = \sigma\sqrt{\pi a} \tag{1.5}$$

In the actual conditions, for the limited scale component, the SIF should be corrected with the influence by function (1.6):

$$K_I = \sigma\sqrt{\pi a} \cdot f\left(a,b,W...\right) \tag{1.6}$$
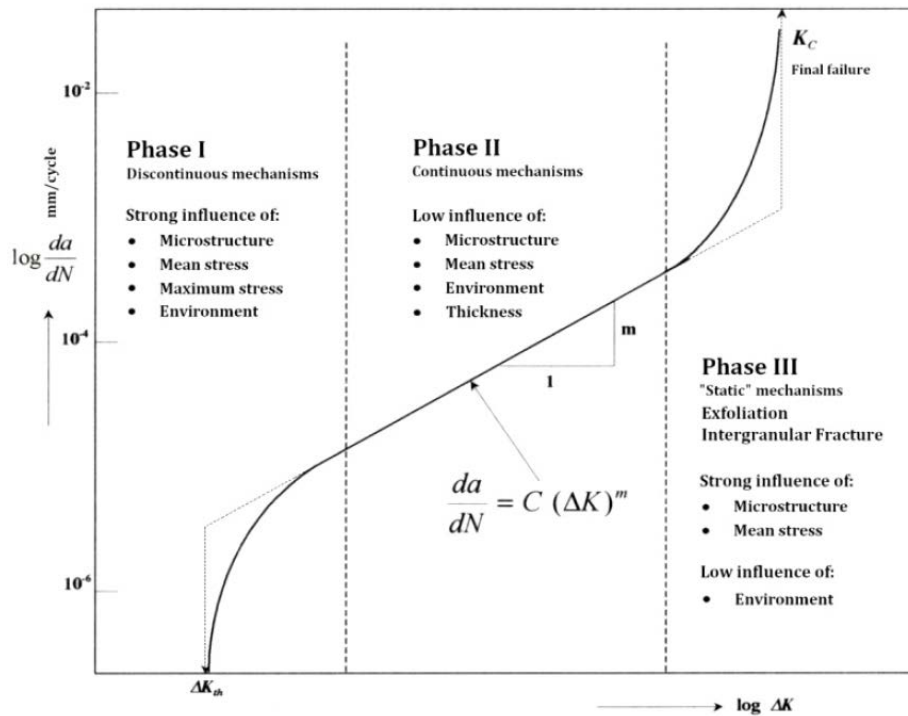
Figure 1.13 Characteristic crack growth curve for a ductile material[76]

Crack growth rate change with SIF in different stages. At the very first stage Phase I, crack growth corresponding to short crack, the propagation speed is high. This topic is not fully understood. Summarizing the experimental facts, it can be outlined that crack growth rate of short crack can exceed those of long cracks at the same applied stress intensity. Moreover, there is threshold for short crack. After the threshold ΔK_{th}, long-crack growth is presumed dormant.

With increasing the crack length, also the value of SIF, the crack growth rate is slightly decreasing in Phase II. Paris proposed double logarithmic law with good agreement with measured crack rate[26]. The period of crack propagation occupies large fraction of fatigue life in LCF and maybe HCF, becoming the most important part in the fatigue propagation research.

The crack growth turns to unstable regime Phase III with further increasing of crack length. The crack growth rate is significantly higher compared with Paris's model prediction, as Equation (1.7):

$$\frac{da}{dN} = C\left(\Delta K\right)^{n}$$

(1.7)

where da is crack increment for dN cycles, C and n are constants depending of the material. For a cyclic stress variation, a variation on the stress intensity factor should be expressed as (1.8):

$$\Delta K = K_{max} - K_{min} \quad \left(K_{min} \geq 0\right)$$

(1.8)

K_{max} and K_{min} are corresponding to the maximum and minimum of stress intensity factors during a cycle of fatigue. If the cyclic loading enters in the compression zone, it is conventionally considered only the positive part, because the crack growth take place in the tension part of the cycle.

The outlined stage of crack propagation can be determined at fracture surface based on its typical fracture morphology. The crack growth during the stage II for most of ductile materials is characterized by so-call micro fatigue striations and macro beach marks. These typical marks on the fracture surface is associated with sequences of loading cycles.

Fatigue striations makes possible to determine the crack propagation direction, duration of growth stage and local crack rate by measurement the crack increment in the loading cycle, shown in Figure 1.14. Some authors assume that forming of such marks on fracture surface is accompanied by environment influence. The gazes presented in the crack are interacts with a new-forming free surface during uploading stage and leaves the clearly seen marks on fracture surface.
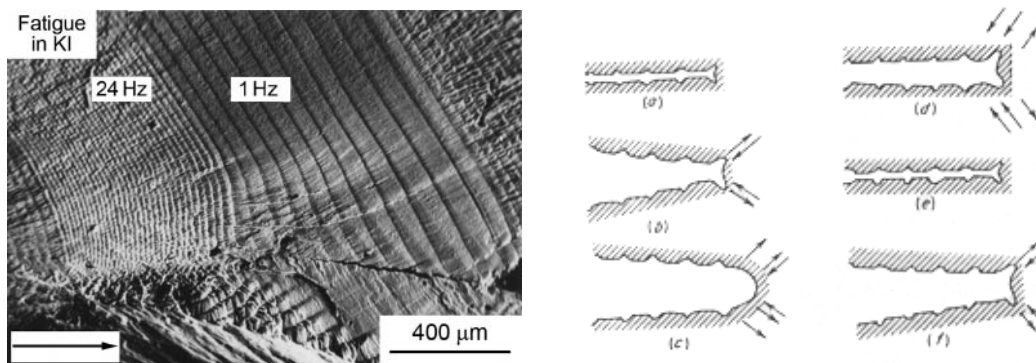
Figure 1.14 Fatigue Striation and Model Approach

Crack propagation in VHCF

As mention before, the crack initiation during the VHCF is highly depending on the type of material. For the Type I ductile single phase metallic materials, it exhibit surface failure initiation from surface PSB in VHCF regime. While for the Type II material containing heterogeneity, inclusion or coarse second phase particle display internal crack initiation in VHCF regime.

For the subsurface crack, crack growth model in VHCF with subsurface initiation is based on Paris Hertzberg McClintock crack growth rate, as (1.9):

$$\frac{da}{dN} = b\left(\frac{\Delta K_{eff}}{E\sqrt{b}}\right)^3 \tag{1.9}$$

where b is the magnitude of Burger's vector, ΔK_{eff} is the effective SIF.

The small crack a_0 starts from defect with size a_{int}, corresponding to the SIF $\Delta K_{eff} = E\sqrt{b}$. And short crack becomes a long crack at a_i, the growth rate is greater for small cracks than for long cracks. The transition point from a short crack to a long crack is located at a point x in terms of the stress intensity factor from the threshold for short cracks, shown in Figure 1.15.
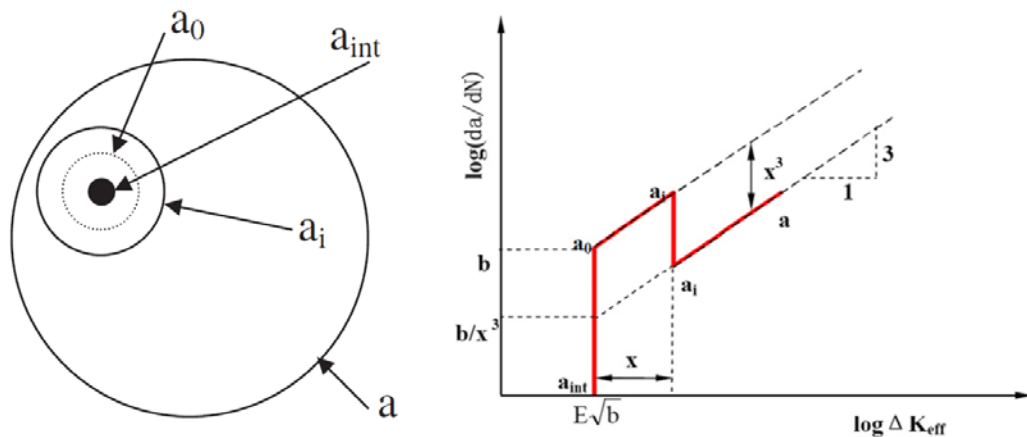
Figure 1.15 Model of Crack Propagation Rate with Subsurface Initiation[86]

And the total fatigue crack growth life can be estimated by addition of the lifetimes as following Equation (1.10):

$$N_{total} = N_{a_{int} \sim a_0} + N_{a_0 \sim a_i} + N_{a_i \sim a} \qquad (1.10)$$

In case of surface initiation, the expression will be more complicated[87-89]. The main difference between subsurface and surface crack initiation is in determination of SIF, shown in Figure 1.16.
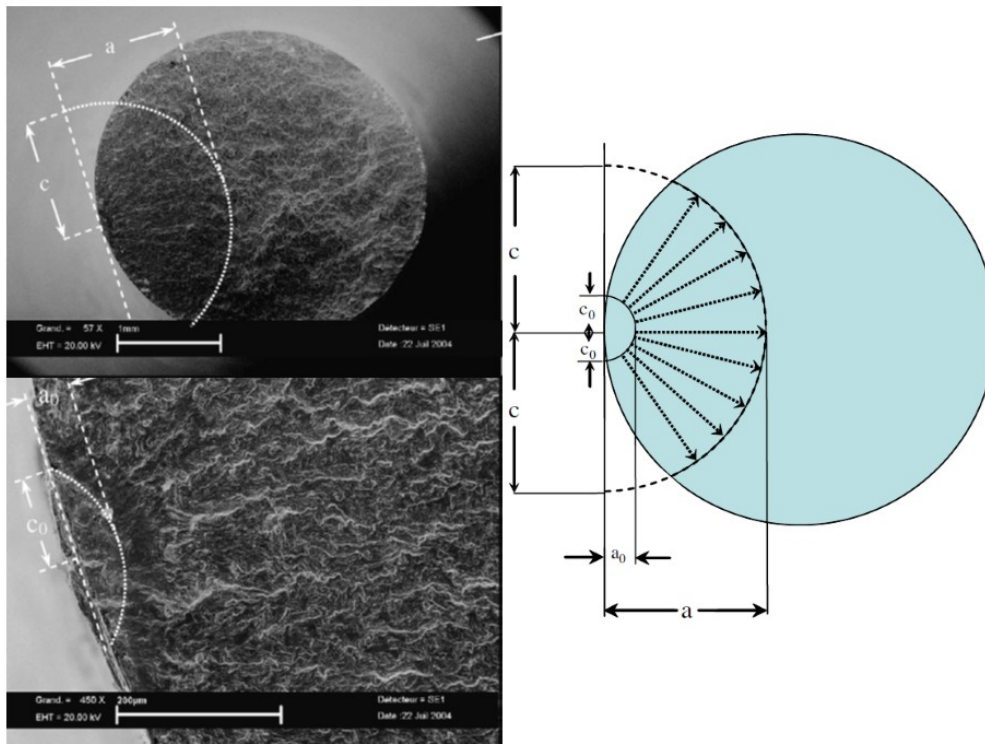
Figure 1.16 Crack Propagation Model with Surface Initiation

It is noticed that the crack propagation life is much smaller than initiation life during VHCF regime, perhaps less than 1% of total life in many cases. So the propagation research in the VHCF always focus on mechanism, the propagation rate is not significant.

1.3 Influence Factor of VHCF

The fatigue resistance of a material is linked to numerous factors, which can be either mechanical or metallurgical. One of the most significant factors deals with the application conditions of the cyclic stresses being applied. For the VHCF test under ultrasonic loading, the most important factor is frequency and temperature due to the material internal friction under high strain ratio.

1.3.1 Frequency and Loading Mode

Many research laboratories around the world have noticed the importance of knowing loading frequency effects on high strength materials' fatigue behaviors. In fact, researchers have investigated these effects on fatigue behavior since 1970s. Bathias and Paris[50] pointed out in their book that during fatigue tests, frequency sensitivity might differ for different materials, and might be affected by crystal types and temperatures. Moreover, Bathias concluded that frequency effects were much more significant between 10 and 0.001 Hz than between 10 Hz and 20 KHz.

Wang compared the gigacycle fatigue test results of ferrous type alloy under several loading frequencies and stress ratios[90]. The insignificant influence of loading frequency on fatigue behavior could also be seen in materials such as carbon steel[91], cast iron and aluminum[92] and so on, which were mostly metals with FCC crystal structures.

On the contrary, some other results draw an opposite conclusion. Yi investigated the gigacycle behavior of single crystal superalloy[93]. High frequency made the S-N curves shift upwards. A similar trend was also found when the work of Korth[94] was compared with Kawagoishi[95] in their research of Inconel 718, no effective models were established to explain this frequency effect.

It must be pointed out that the test result above come not only from the different frequency, but also the different loading mode. For high frequency ultrasonic testing, full reversed tension compression loading is applied, resulting in a uniform distribution of stress on the valid cross section, and thus the whole cross section will have the same largest stress. While in the rotary-bending testing, the specimen will have a linear-distributed stress state on the valid cross section.

Conventionally, the risk volumes, estimated as the region subjected to above 90% of the maximal stress, are used as a qualitative measurement of VHCF lives, specimens with large risk volumes are believed to fracture with short lives[96]. Therefore, risk volumes of the ultrasonic test specimens are much larger than those of the rotary bending tests. As a result, it is widely believed that fatigue life of a tension-compression case is shorter than bending case with same conditions.

For a given material, such as carbon steel, we can find as many endurance limits as types of cycles (alternate, repeated, waved) and stress of different natures (traction, bending, torsion). Comparison of test results usually shows that the endurance limit values decrease when we switch from rotating bending to planar bending, tension compression and finally torsion. Deviations between the different values depend on the adaptation possibilities of the steel considered.

$$\sigma_{f(RB)} > \sigma_{f(PB)} > \sigma_{f(TC)} > \sigma_{f(TT)} > \tau_{f(Torsion)} \qquad (1.11)$$

● Rotary Bending (RB):

In the case of rotating and planar bending, stress is not homogenous within the section of the specimen. It is highest for external and close to zero on the axis. Distribution of stress through a section should lead to a rotary bending endurance higher than a planar bending endurance when specimens of the same circular sections and shapes are used.

● Planar Bending (PB):

In the case of planar bending, stress is highest for external fibers and close to zero on the axis when there are non-uniform stress within the sections considered. Planar bending usually gives some endurance limit values higher than those obtained with tension compression. While, in the case of planar specimens of rectangular section, the edge is not well defined and can lead to some local initiations that can reduce fatigue resistance. This is known as the edge effect.

● Tension-Compression / Tension-Tension (TC / TT):

In the case of tension-compression or tension-tension, stress is homogenous across the whole section. All the section will have the same largest stress.

● Torsion:

According to the elasticity theory, there is a constant ratio equal to $1/\sqrt{3}$ between failure strength in the case of torsion and traction. However, according to numerous results, this ratio varies between 0.45 and 0.75.

1.3.2 Temperature

Temperature can be considered as another influence of ultrasonic testing. Material properties varied obviously as temperature changed, for example yield stress, ultimate stress, especially the elastic modulus. Because of working under resonance condition during the ultrasonic test, fatigue specimen was needed to redesign for keeping close to the excited frequency, according to the different temperature distribution.

There were two type of equipment for impose high temperature on the specimen: induction coil heater and chamber heater. The induction coil heater was simple and fast launch, while the chamber heater provided uniform temperature distribution of all the specimen.
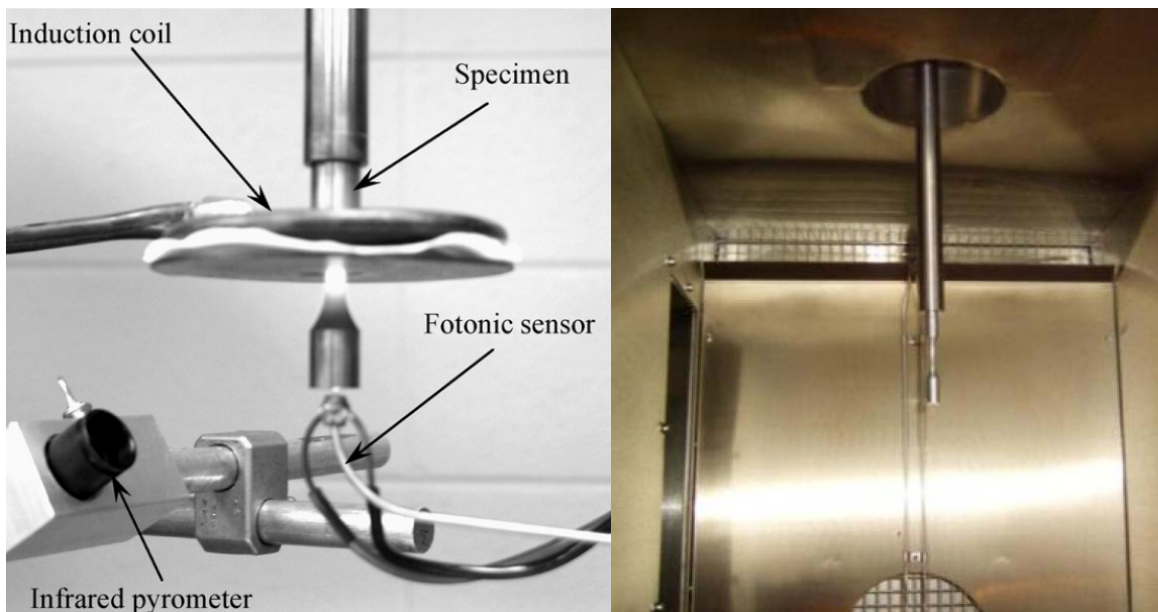
Figure 1.17 Two Different Type Ultrasonic Equipment for Elevated Temperature

No matter which scheme has been chosen for the test, there was must be added cylinder rod between specimen and horn for isolation the high temperature, avoiding damage the piezoelectric ceramic in the transducer. The length of this rod should be equal or times to the wavelength, shown in Figure 1.18.
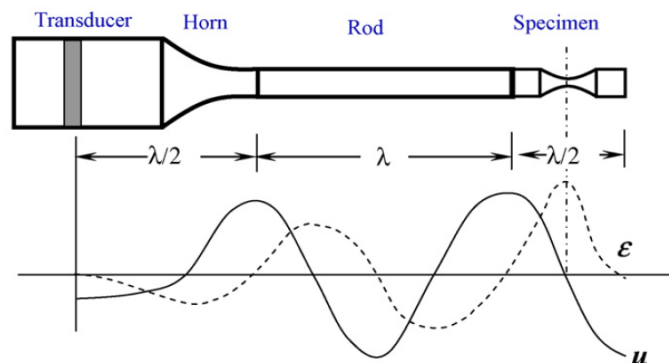
Figure 1.18 Rod Bar for the High Temperature Fatigue Test

Reger and Remy have made investigations on the LCF and HCF properties of nickel based superalloy, such as the effect of temperature on the cyclic stress-strain response and fatigue life associated with the deformation microstructures [97, 98]. This study has shown marked decreasing in total fatigue life for given total strain range when the temperature increasing. It has been related to the marked decrease in yield stress with increasing temperature and to the fact that, in the fatigue life range investigated, the total strain range is dominated by the elastic contribution.

The influence of temperature on fatigue life has corresponding to the change in crack initiation and growth mechanisms; oxidation played the major role in the cracking process at high temperatures. The influence of oxidation may affected both the initiation and the propagation stages.

Yi studied the ultrasonic fatigue phenomenon of single crystal Ni-based superalloy at high temperature[93]. It shown that the material occurred in crystallographic manner on *{111}* octahedral slip plane, in contrast to the normal Mode I growth typically mode observed in single crystal superalloys with conventional servo-hydraulic loading.

Besides the applied temperature field, another important consideration in ultrasonic testing was the self-heating that the material generated internally due to the mechanical energy dissipation under the ultra high strain ratio. For some kinds of material, the mechanical energy dissipation could lead the large temperature increasing over hundred degrees, it should be pay additional attention.

1.3.3 Stress Ratio

The geometry of loading cycle can be different from sinusoidal, triangular, trapezoidal, etc. Typical curve of sinusoidal loading is shown on the Figure below. The loading consists of two parts: static stress or mean stress σ_m and alternating stress with amplitude σ_a. The static stress has a significant influence on the fatigue behaviour of material as was shown for the first time.
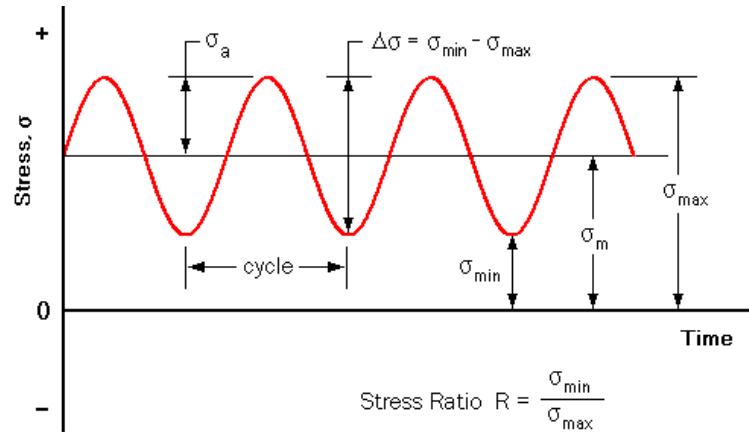
Figure 1.19 The Typical Sinusoidal Loading Parameters

The relation between minimum and maximum stress is called as "stress ratio". In case when the mean stress is equal to zero, the cycle becomes symmetrical and called fully-reversed loading with **R**=-1.

$$\begin{cases} \sigma_m = \dfrac{\sigma_{max} + \sigma_{min}}{2} \\[2mm] \sigma_a = \dfrac{\sigma_{max} - \sigma_{min}}{2} \end{cases} \qquad (1.12)$$

$$R = \frac{\sigma_{min}}{\sigma_{max}} = \frac{\sigma_m - \sigma_a}{\sigma_m + \sigma_a} \qquad (1.13)$$

An increase in the mean stress statistical stress leads to a reduction in the dynamic stress resistance of a material. When focus on fatigue calculation of structures, it is important to know the evolution of σ_a as a function of σ_m

Several models explaining the effect of mean stress were developed. The outstanding equations are following: Gerber model at 1874, Goodman model at 1899, Soderberg model at 1930 and Morrow model at 1960.

Gerber:
$$\frac{\sigma_a}{\sigma_f} + \left(\frac{\sigma_m}{\sigma_b}\right)^2 = 1 \tag{1.14}$$

Goodman:
$$\frac{\sigma_a}{\sigma_f} + \frac{\sigma_m}{\sigma_b} = 1 \tag{1.15}$$

Soderberg:
$$\frac{\sigma_a}{\sigma_f} + \frac{\sigma_m}{\sigma_y} = 1 \tag{1.16}$$

Morrow:
$$\frac{\sigma_a}{\sigma_f} + \frac{\sigma_m}{\sigma_k} = 1 \tag{1.17}$$

where σ_y, σ_b, σ_k is yield / ultimate / true fracture stress, σ_f is fatigue endurance at a given number of cycles (Ferrous metals 10^7; Non-ferrous 10^8).

The Haigh diagram is another way of presenting the fatigue data with regard to mean stress effect. On this diagram, stress amplitude is plotted as function of mean stress. Each line is for constant number of cycles[99], shown in Figure 1.20.
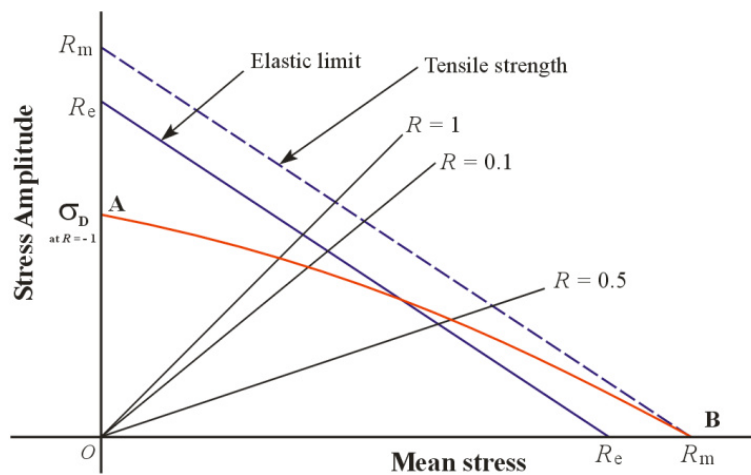
Figure 1.20 Theoretical Haigh Diagram

1.4 Inconel 718 / GH4169 / NC19FeNb

High temperature superalloy is a series of materials who provide high resistance to corrosion, oxidation, thermal creep deformation, as well as mechanical strength at elevated temperatures. The crystal structure is typically face centered cubic FCC austenitic. According to the fundamental chemical component in the alloy, it can be divided into Ni, Co, Fe-based superalloy and so on. Nickel based superalloys have emerged as the material of choice for these applications.

Nickel based superalloy was invented in the 1940s for gas turbine applications because of its long time strength and toughness at high temperature. Nickel has a high activation energy for self-diffusion which resistant to creep deformation. Early nickel based superalloy typically contained nearly 80% Ni and 20% Cr, another elements such as Ti, Al, Mo, W, etc, have been added to enhance its mechanical properties[100]. Modern nickel base superalloy have not only complex composition, but also an intricate phase by adding special elements, particularly with Nb, Re, Ta, Y. Lots of different phases and precipitates can be found[101]:

- γ   Gamma phase compose the matrix phase of nickel based superalloy. It has solid solution FCC austenitic crystal structure of the alloying elements with solute elements such as Cr, Co, Fe and Mo.

- γ'   Gamma prime is an intermetallic phase which constitute the precipitate used to strengthen the alloy. It has an FCC structure with a composition of Ni, Al and Ti.

- γ"   Gamma double prime is a strong coherent precipitate with a Body Centered Tetragonal (BCT) structure rich in Nb. It is used to strengthen Ni based superalloys at lower temperatures relative to γ'. It's metastable and can transform into delta phase under some circumstances.

- δ   Delta phase is a non hardening precipitate usually found at grain boundaries, where it improves the creep rupture and grain boundary sliding resistance. It is orthorhombic and composed mainly of Ni and Nb.

- TCP Topologically close packed phases include σ, μ, Laves and so on. They are characterized by their tendency to be highly brittle and deplete the γ matrix of strengthening, solid solution refractory elements.

Inconel is a family of austenitic nickel chromium based superalloys produced by Special Metal Corporation (developed from International Nickel Corporation). It has better temperature resistance due to higher proportion of Nickel over 50%, relative to another nickel iron chromium alloy Incoloy, and better corrosion resistance due to the higher proportion of Niobium, relative to Nimonic family.

Inconel, when heated, forms a thick stable passivity oxide layer that protects its outer surface from further attack. It retains strength over a wide temperature range, attractive for high temperature applications, where steel, aluminum or titanium would succumb to thermal creep. Inconel high temperature strength is developed by solid solution strengthening or precipitation hardening, well suited for service in extreme environments subjected to high pressure and kinetic energy.

Inconel is difficult shape and machine metal using traditional techniques due to rapid work hardening. For this reason, age-hardened Inconel such as 718 are machined using an aggressive but slow cut with a hard tool, minimizing the number of passes required. Alternatively, the majority of the machining can be performed in a solution form, only the final step being performed after age hardening.

Inconel 718 alloy (GH4169 in China, NC19FeNb in France) is a high strength, corrosion resistant nickel chromium material used at -250 ~ +700°C. It can be fabricated even complex parts, combining with good tensile, fatigue, creep, and rupture strength, have resulted in use in wide range of applications, for example the components of aircraft and gas turbine engines, liquid fueled rocket and cryogenic tankage.

Table 1.1 Limiting Chemical Composition[102, 103]

Element	Ni	Cr	Fe	Nb+Ta	Mo	Ti	Al
Weight %	50~55	17~21	Balance	4.75~5.5	2.8~3.3	0.65~1.2	0.2~0.8

Element	Co	Mg	Si	Cu	C	S	B
Weight %	<1.0	<0.35	<0.35	<0.3	<0.08	<0.015	<0.006

Airline Engine (Inconel 718) Bearing Support (Inconel 718) Outlet Manifold (Inconel 718) Casingcomb (Inconel 718)

Jet Engine Airfoils (Ni Superalloy: CMSX) Seal / Flaps (Ni Superalloy: Rene 41) Bearing Support (Ni Superalloy: C263) Nozzle Guide Vanes (Ni Superalloy: C1023)

Figure 1.21 Typical Component by Inconel 718

For most applications, heat treatment of Inconel 718 is specified as solution annealed and precipitation age hardened. 718 is strengthen by the precipitation of secondary phases, such as gamma prime and double prime, into matrix. For this metallurgical reaction to properly take place, the aging constituents (Al, Ti, Nb) must be dissolved in the matrix; if they are precipitated as some other phase or are combined in some other form, they will not precipitate correctly and the full strength of the alloy with not be realized.
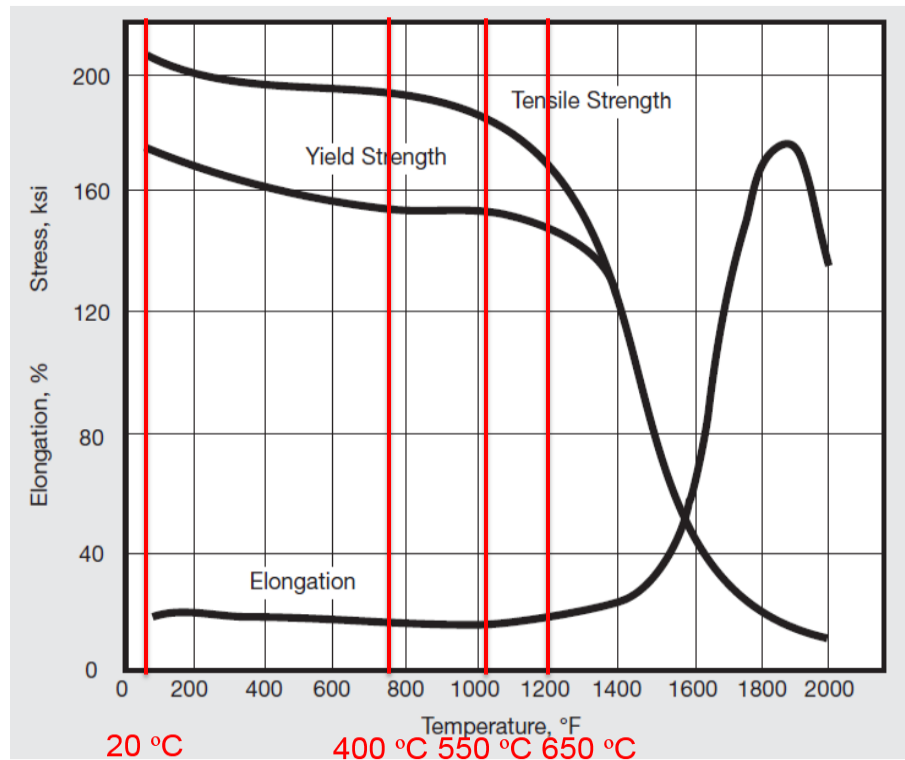
Figure 1.22 High Temperature Properties of Inconel 718

$$^{*}5 \times T\left(^{\circ}F\right) = 9 \times T\left(^{\circ}C\right) + 160$$

Obviously, the yield strength of Inconel 718 is not always gradual as the temperature changed. It decreased not so much before design temperature 550°C, ensuring the good strength under high temperature. While it decreases seriously after design temperature. This phenomenon will lead a qualitative change when temperature rising appeared inside of the specimen during the test.

Most nickel based superalloy cyclically harden, but in contrast to Inconel 718 cyclically soften[2]. Inconel 718 is known to exhibit the phenomena of ratchetting and mean stress relaxation, and since the mean stress of the material has an influence on the fatigue crack initiation life of the material[104].

1.5 Fatigue of Inconel 718

Inconel 718 was mainly used in the components of aircraft engine, gas turbine, liquid fueled rocket and so on, combining with good tensile, fatigue, creep, and rupture strength. There are mainly three kinds of test for this material:

● LCF test with compact tension specimen was applied for simulation the fatigue crack propagation (FCP) caused by high-amplitude low-frequency centrifugal force and high temperature gradient thermal stress.

● LCF / HCF test with hourglass specimen predicted the fatigue life for ensuring the reliability and safety of the engine.

● VHCF test with hourglass specimen focused on the fatigue crack initiation duo to low-amplitude high-frequency vibration tensile force transferred from rotary blade or turbine shaft.

Schematic illustration of compact tension specimen for fatigue crack propagation test (FCP) and hourglass specimen for VHCF test shown their location in the Figure 1.23 [105].
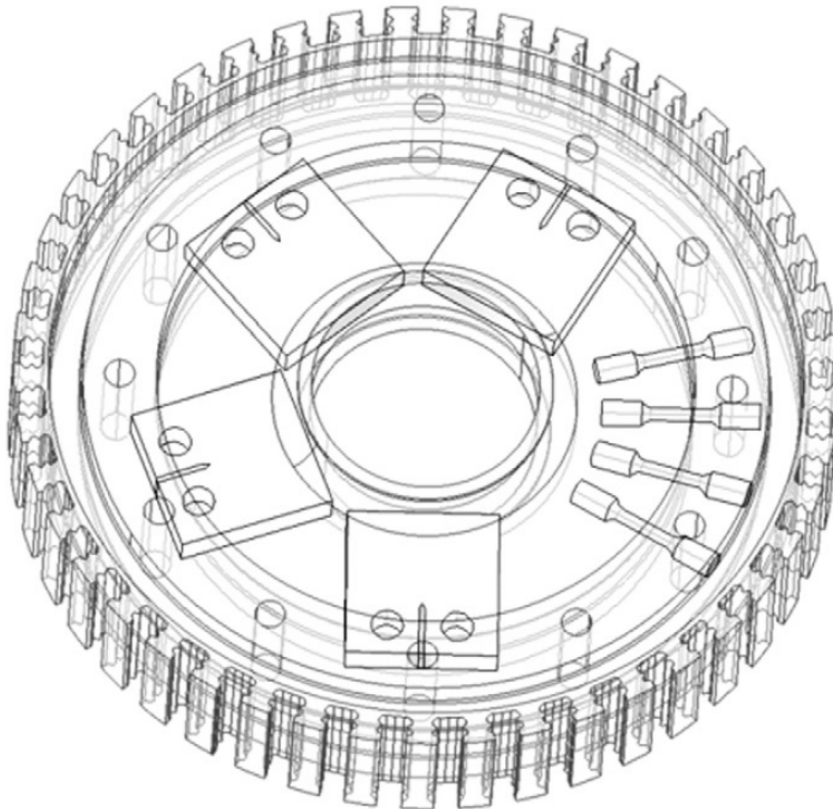
Figure 1.23 Schema of Specimen Location

1.5.1 LCF / HCF of Inconel 718

During the past few decades, extensive investigations have been made on the LCF and HCF properties of Inconel 718, such as the effect of temperature on the cyclic stress-strain response[106], fatigue life associated with the deformation microstructures, the influencing of temperature, environment, loading parameters on the fatigue crack growth[107, 108], the creep fatigue oxidation interaction[107, 109], the mechanism based modeling of fatigue life prediction and so on[110].

The most fundamental data came from the official manual by Special Metal Corporation who developed Inconel series. Rotary bending was applied in the test. It was clearly that the fatigue life increased obviously as loading stress increased, shown in Figure 1.24. It was also said that material can be used in the annealed rather than the annealed and aged condition after forging when fatigue strength was of prime importance, aging treatment only raised fatigue strength slightly.
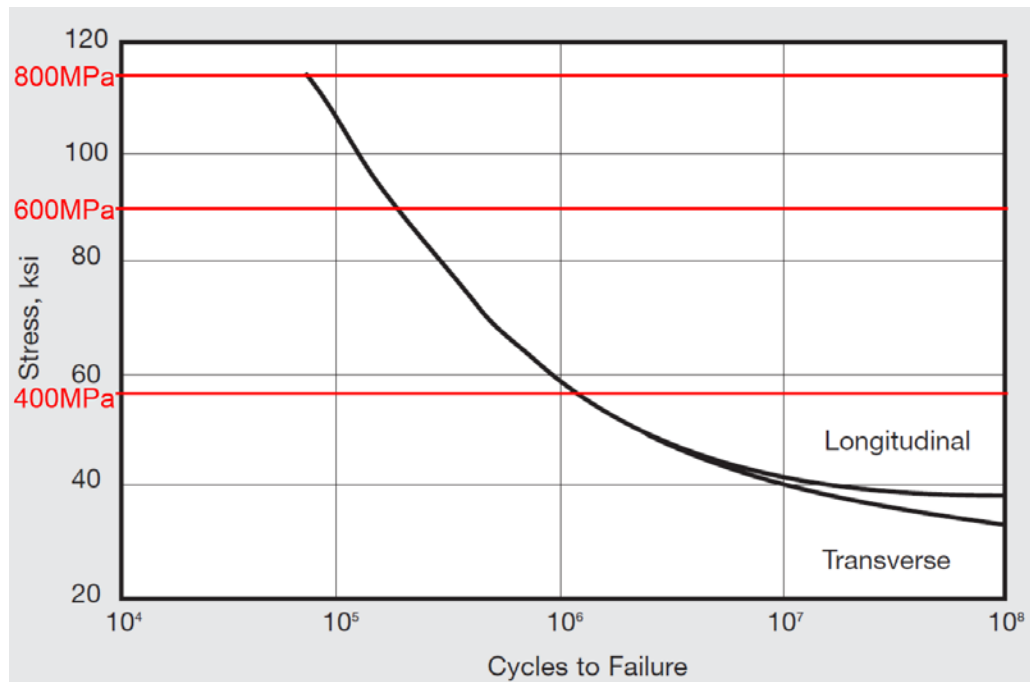
Figure 1.24 Room Temperature Fatigue Strength of Cold Rolled Sheet Annealed and Aged with Average Grain Size 50μm[102]

$$^*1ksi = \frac{kbf}{in^2} = \frac{1000 \times 0.454 \times 9.8N}{25.4^2 \, mm^2} = 6.895MPa$$

Grain size was also major factor in achievement of high fatigue strength. Fatigue endurance limit at 10^8 cycles decreased obviously as average grain size increased, shown in Figure 1.25. It could be promoted by requisite fine grain at the not very high temperature working condition. For the high temperature fatigue strength, creep property became another important consideration.
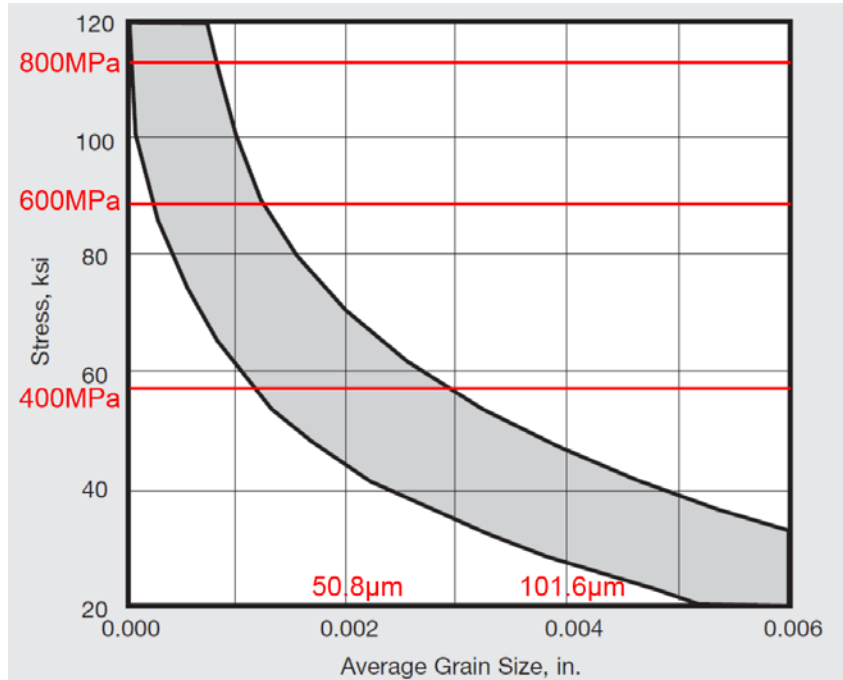
Figure 1.25 Effect of Grain Size on Fatigue Endurance Limit at 10^8 cycles of Plate Annealed and Aged[102]

Yan performed also rotary bending fatigue test on Inconel 718, found there was no failure in gigacycle range at room temperature, but was at 500 ℃[111]. However, Chen studied the fatigue behaviour under ultrasonic frequency firstly, revealed that fracture still occurred between 10^7 and 10^8 cycles[112, 113]. After that, some other team continued to investigate the ultra high fatigue phenomenon of Inconel 718 under ultrasonic loading.

1.5.2 VHCF of Inconel 718

Compared to the LCF and FCP research, only few teams investigated the VHCF behaviour of Inconel 718 using ultrasonic system over 10^9 cycles, less than 20 articles have published about the relation between fatigue life and stress or focused on the crack initiation mechanism under low-amplitude high-frequency loading. Especially, the heat treatment processing and test condition were not same, that has led more difficulties.

Team Kawagoishi from Japan in 2005, 2008 and 2010

In 2005, Chen, Kawagoishi, et al[112] investigated fracture and small crack behavior of nickel based superalloy Inconel 718 in very high cycle of 10^9 cycles under ultrasonic fatigue in ambient air at room temperature. To minimize internal friction induced temperature rise, ultrasonic fatigue tests were performed in pulse-pause manner with pulse length varied in a range of 25~50 ms and pause between 1000~2000 ms. The maximum temperature rise at the most stressed node section surface was controlled below 5~8°C during the testing. The influence of ultrasonic frequency was examined by comparing the results with those in conventional low frequency fatigue, shown in Figure 1.26.
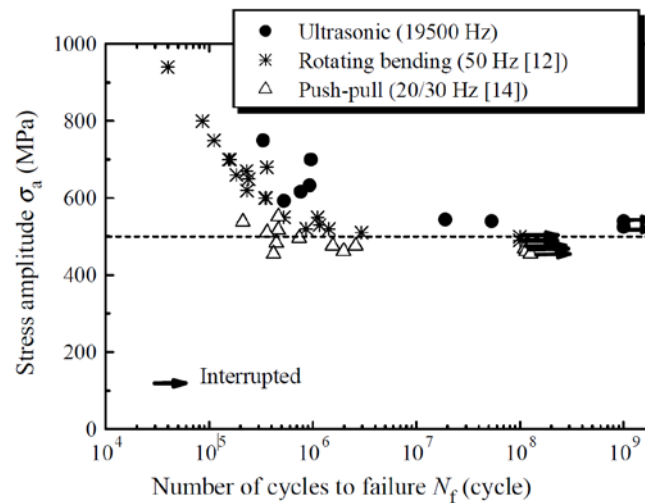
Figure 1.26 S-N Curve of Inconel 718 under Ultrasonic and Rotary Bending

In 2008, Kawagoishi, Maemura, et al[114] studied the effect of grain size on ultrasonic fatigue properties of Inconel 718 with different grain sizes in ambient air (in Japanese).

(a) S (18 μm)   (b) M (88 μm)   (c) L (276 μm)

(a) S   (b) M   (c) L
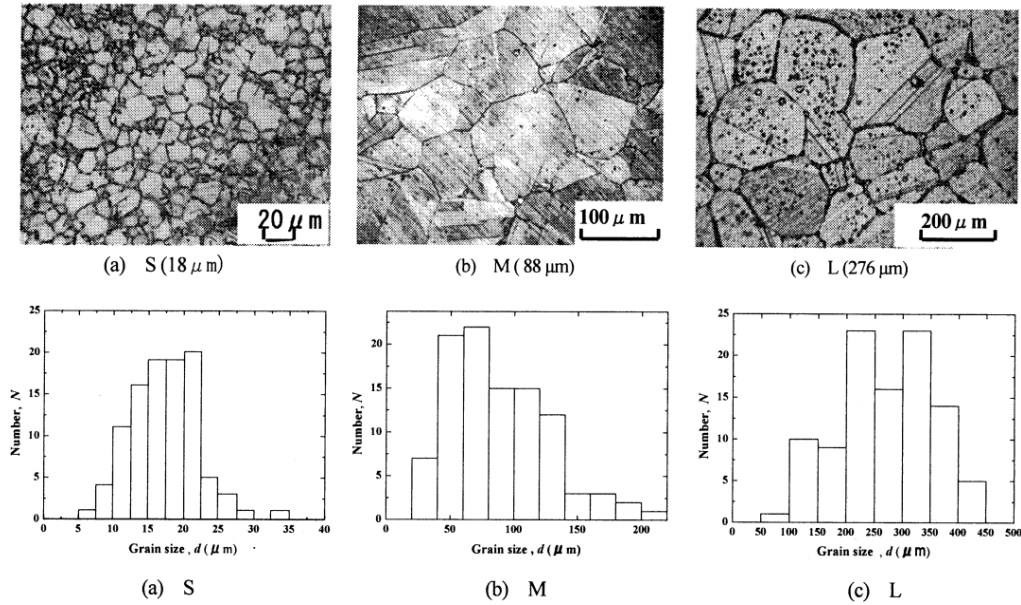
Figure 1.27 Microstructure and Grain Size Distribution under 3 Heat Treatment

　　Mechanical strength and fatigue strength were increased at the same time with decreasing in grain size, shown in Table 1.2. The increasing of yield strength could be explained by flow stress. The relation between yield strength and reciprocal of root of grain size was approximated by a straight line, followed as Hall-Petch equation. The increasing in fatigue strength by refining grain size was mainly caused by the suppression of crack initiation. Flow stress increased and Hall-Petch relation hold even under high strain rate.

Table 1.2 Mechanical properties of Inconel 718 with 3 Grain Size

Grain size	$\sigma_{0.2}$(MPa)	σ_B(MPa)	σ_T(MPa)	Ψ(%)
18 μm (S)	1147	1372	2073	38.1
88 μm (M)	1074	1298	2340	55.8
276 μm (L)	988	1175	2143	49.1

$\sigma_{0.2}$: 0.2% proof stress (MPa)　　σ_T: True breaking stress (MPa)

σ_B: Tensile strength (MPa)　　Ψ : Reduction of area (%)
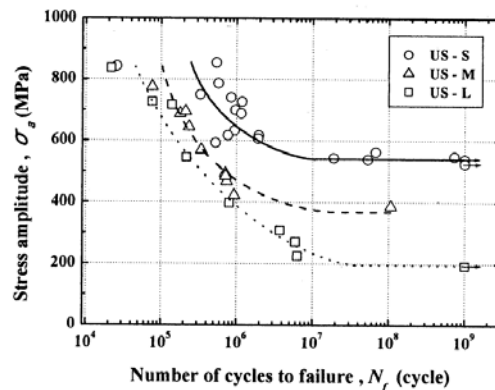
Figúre 1.28 S-N Curve of Inconel 718 with 3 Grain Size

In 2010, Yan, Kawagoishi, et al.[115] investigated the effect of loading frequency on fatigue property of Nickel based superalloy Inconel 718. In order to change the grain size, the alloy was solution treated for 1 h at three different temperatures of 982, 1050 and 1100ºC and then water quenched. Precipitated particles of Ni_3Nb were observed at grain boundary by EDX. Fatigue strength was increased with decreasing in grain size. Moreover, fatigue strength under ultrasonic loading was higher than that under rotating bending, shown in Figure 1.29.
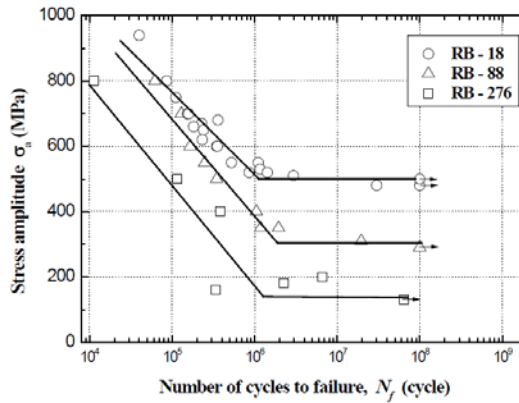
(a) Rotating bending
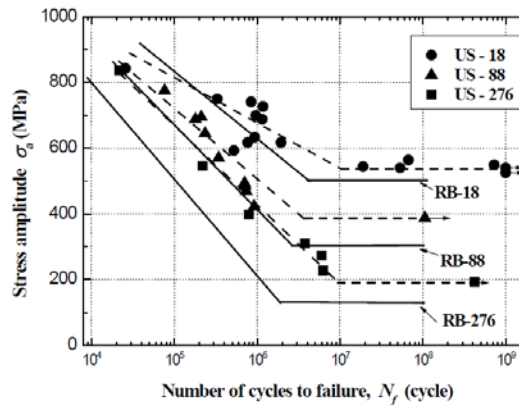
(b) Ultrasonic

Figure 1.29 S-N Curve of Inconel 718 under Ultrasonic and Rotary Bending

Team Duan and Shi from China in 2010 and 2013

In 2010, Ma, Duan, et al.[116] investigated fatigue and fracture behavior of Inconel 718 under rotary bending of 52.5Hz (3150r/min) until 10^9 cycles at room temperature. The microstructure consisted of grey blocks of carbides and fine lenticular particles δ phases (Ni$_3$Nb) distributed in the matrix. Nearly equiaxed grains of Ni-rich FCC solid solution (γ phase) can be seen, exhibiting average grain size of around 10 μm. Fractographic analysis revealed that there was transition from fatigue crack initiation at multi sites to single with decreasing stress levels, shown in Figure 1.31.
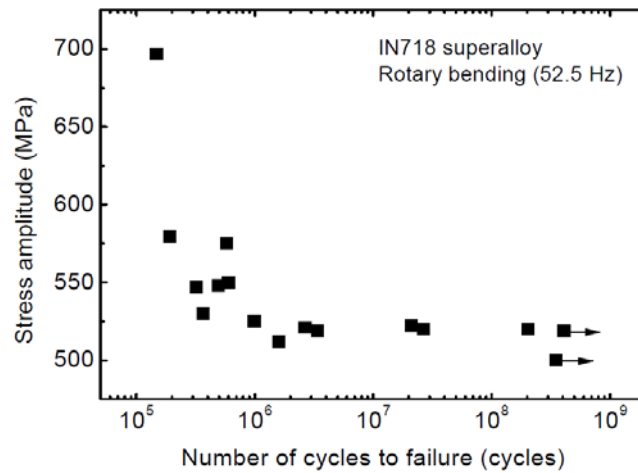
Figure 1.30 S-N Curve of Inconel 718 under Rotary Bending
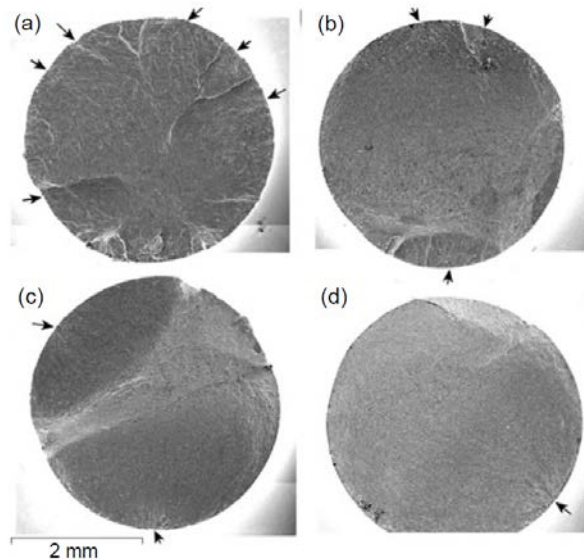
Figure 1.31 Transition of Initiation Site with Fatigue Life
(a) 697 MPa, $1.48*10^5$;   (b) 548 MPa, $4.91*10^5$;
(c) 625 MPa, $9.91*10^5$;   (d) 519 MPa, $33.9*10^5$.

In 2013, Zhang, Duan, et al.[96] compared the very high cycle fatigue behaviors of Inconel 718 with different loading frequency by ultrasonic method (20 kHz) and rotary bending method (52.5 Hz) both at room temperatures. It was continuously air-cooled to suppress any temperature increase during all tests, making sure that approximate room temperature was supplied in the whole process. Results disclosed that cycles to failure at given stress level increased with an increasing of the applied frequency, shown in Figure 1.32.
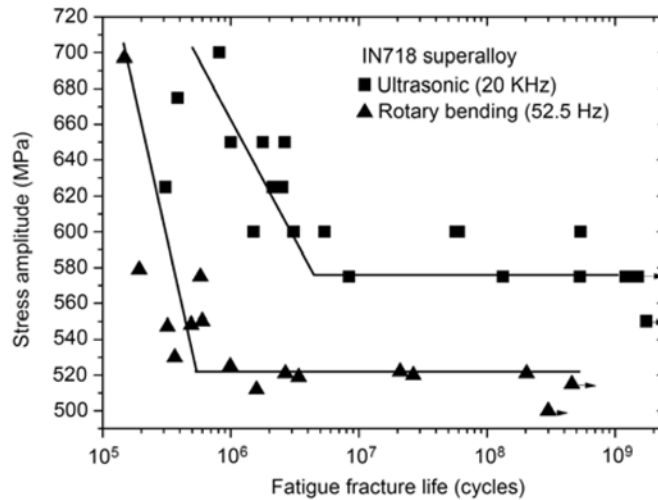
Figure 1.32 S-N Curves at Room Temperature

Fractography revealed that the main fracture surfaces (predominate cracks) for both type of testing are about 45º inclined to specimen axis, indicating that fatigue crack grow along the planar slip on {111} plane, which is favorable in FCC superalloys, shown in Figure 1.33. This was in accordance with the in-situ SEM examination, which proved dominance of transgranular crack growth mechanism at room temperature under various SIF ranges and maximum stress values.
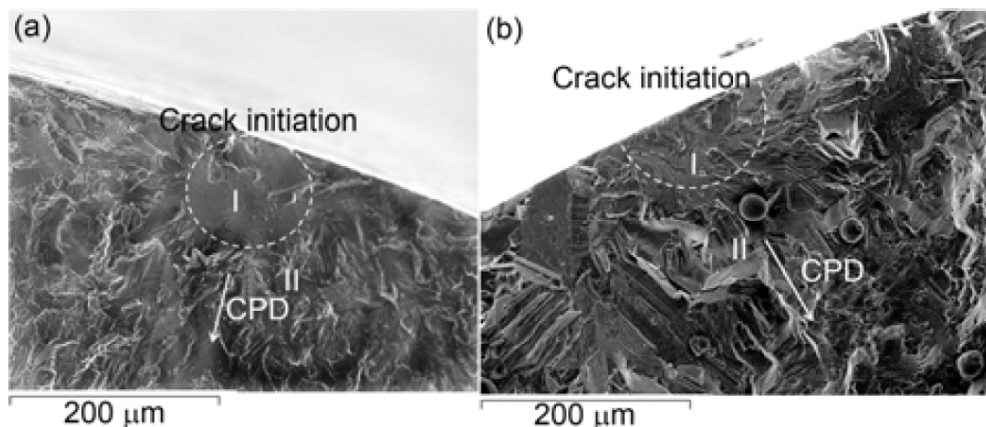
Figure 1.33 Typical Fracture Surfaces of Fatigue Specimen
(a) Ultrasonic, 625MPa, $3.09*10^5$;   (b) Bending, 547MPa, $3.21*10^5$;
(CPD: Crack Propagation Direction)

Team Bruchhausen in 2013 and 2015

In 2013, Bruchhausen, Hahner, et al.[117] described the device with ultrasonic excitation in asymmetric push pull mode demonstrating the deterioration of the lifetime of Inconel 718 in the high pressure gaseous hydrogen compared to argon. E_{dyn} has been determined experimentally by means of dedicated cylinder. The calibration between calculation and strain gauge shown non-linearity for low amplitude below 4 μm. This was governed by unreliability of power generator for very low control voltage. Besides, the discrepancy between the measured and calculated axial stress was less than 3%, shown in Figure 1.34.
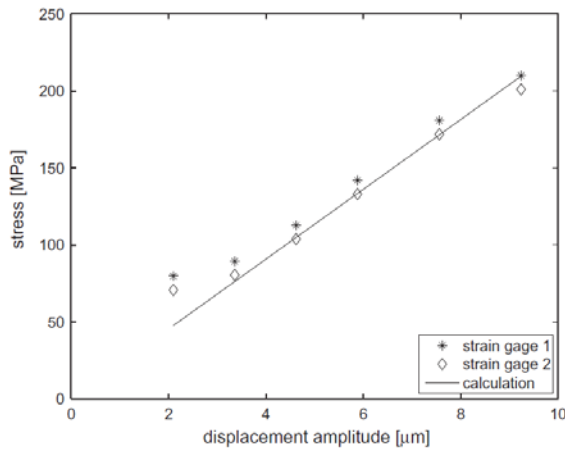
Figure 1.34 Comparison of Stress Amplitude by Strain Gauge and Calculation

Fatigue life in H_2 was shorter than in Ar, although the stress amplitude was slightly lower, shown in Figure 1.35. It seems obvious that the environmental effect outweighs the scatter of the data, proving deleterious effect of hydrogen under those conditions.
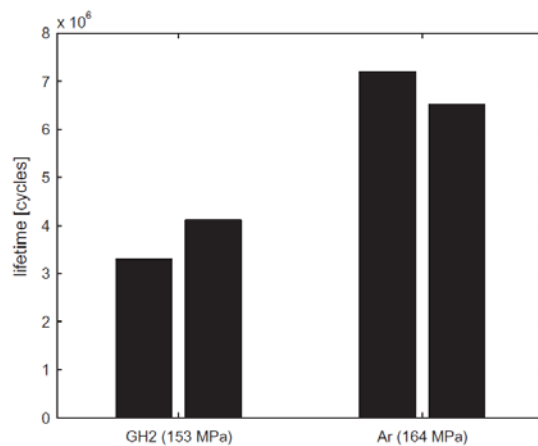
Figure 1.35 Lifetime of Inconel 718 in H_2 and Ar with mean stress 600 MPa

In 2015, Bruchhausen, Fischer, et al.[118] studied the impact of environment on the high cycle fatigue behaviour of Inconel 718 in asymmetric push pull mode at room temperature. It has been shown experimentally that the specimen remains at room temperature without additional cooling. Monitoring the resonance frequency during the test is sufficient to verify constant temperature during the test. Obvious environmental effect shows that fatigue strength in H_2 was always lower than which in Ar, shown in Figure 1.36 and Figure 1.37.
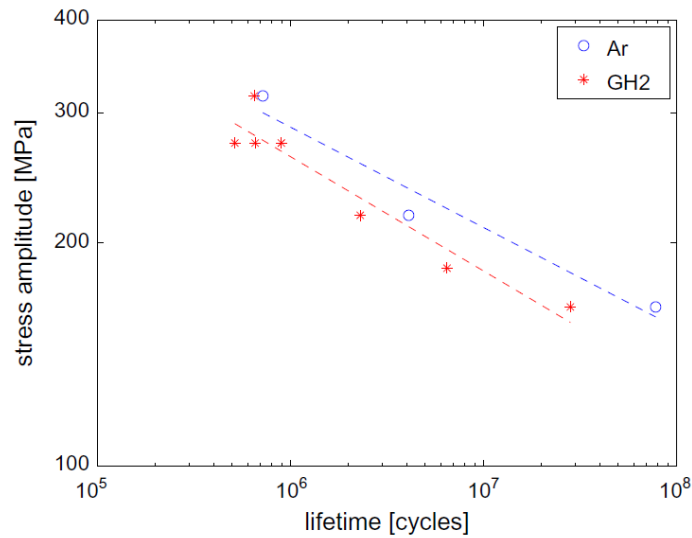
Figure 1.36 Stress Amplitude versus Fatigue Life with Mean Stress 500 MPa
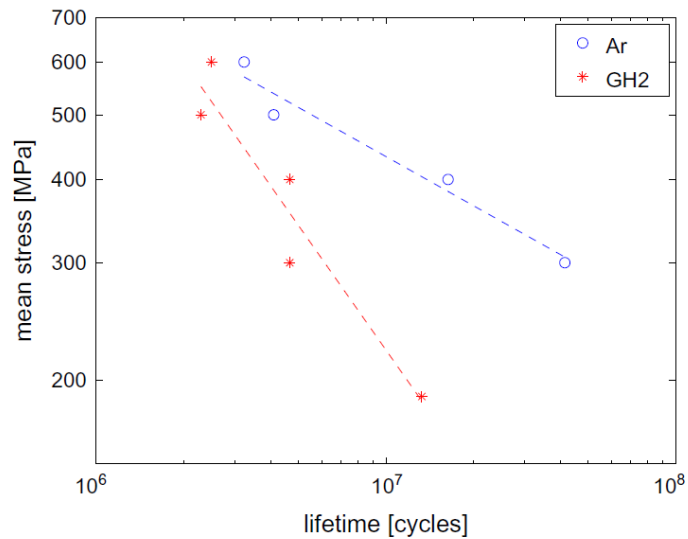
Figure 1.37 Mean Stress versus Fatigue Life with Stress Amplitude 218 MPa

41

Team Belan in 2014 and 2015

In 2014, Belan[119] investigated the fractography analysis of Inconel 718 after fatigue test under high frequency push pull mode at room temperature. The microstructure of wrought 718 was consisted of light gray blocks of primary carbides and fine lenticular and lamellar particles of δ orthorhombic phase Ni_3Nb distributed in the FCC matrix, which grain size approximately 10 μm and few deformation twins. Major strengthening phases small part of γ' $Ni_3(Ti/Al)$ but mostly γ" Ni_3Nb coherent solid state precipitate was hard to observe, due to insufficient SEM magnification, better to use TEM, shown in Figure 1.38.
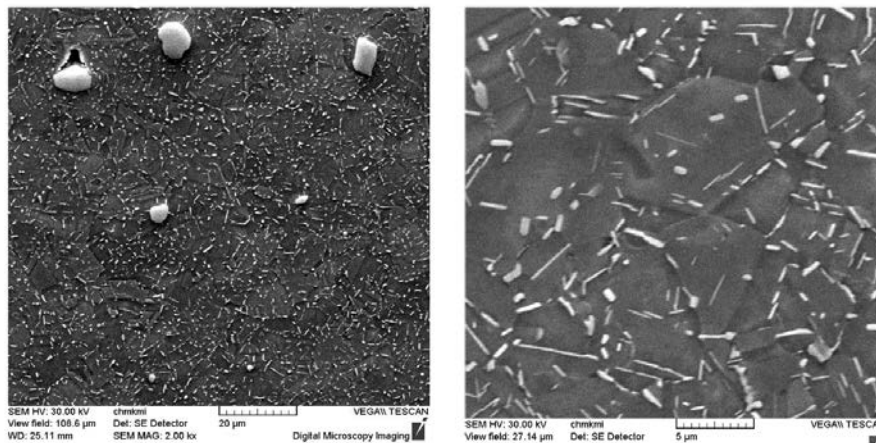
Figure 1.38 Typical Microstructure of Wrought Inconel 718, Etched by Kallings

The high frequency fatigue test was performed by ultrasonic push pull method and appropriate cooling was used to avoid temperature rise. Fatigue life increases with decreasing stress amplitude and the S-N curve appears to continuously decline as the life extends, shown in Figure 1.39. Fractography analysis shown that crack initiation site was controlled by crystallographic slip at surface grains or massively oxidized areas, and after propagated by typical transcrystalline mechanism.
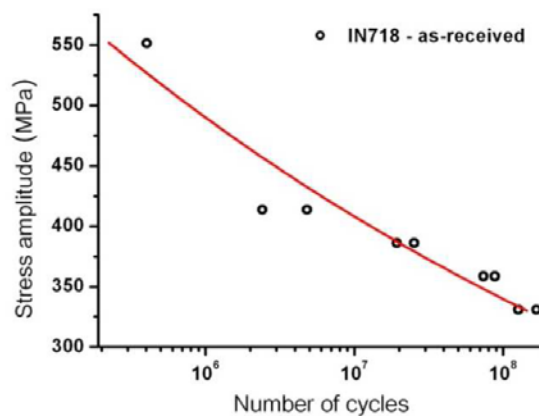
Figure 1.39 S-N curve of Inconel 718 at 20 kHz, R=-1, RT

In 2015, Belan[120] carried out microstructure and fractography evaluation for high frequency fatigue of Inconel 718. Superalloy was consisted of the austenitic FCC matrix phase γ, that solid solution of such elements as Cr, Fe, Co in Ni. Secondary phases in controlling property were γ' phase FCC ordered $Ni_3(Ti/Al)$ and γ'' BCT ordered Ni_3Nb intermetallic compounds in nickel based superalloys. The γ'' and γ'' also are known as geometrically close-packed GCP phases.

Important carbide forming elements are titanium, tantalum, niobium (MC); molybdenum, tungsten (M_6C); chromium (M_7C_3, $M_{23}C_6$,), where M stands for the type of metal atom. Average size of these carbides varied from 4.01~11.79 μm. According to carbide size evaluation, there was no reason to be afraid of affecting fatigue life at any, low or high cycle fatigue cracking, shown in Figure 1.40.
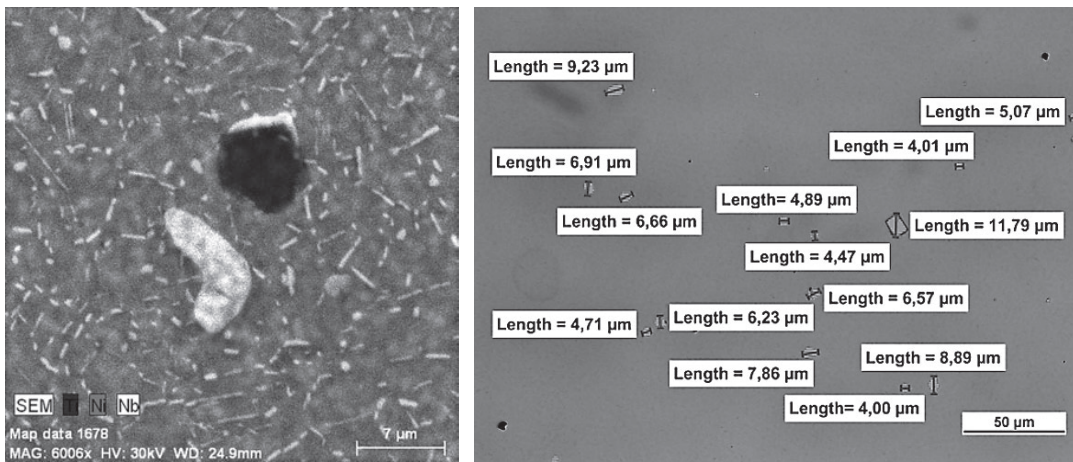
Figure 1.40 Carbide Evaluation in Etched and Non-etched Specimen

Amanov in 2015

In 2015, Amanov, Pyun, et al.[121] investigated ultrasonic fatigue performance of Inconel 718 at elevated temperature. It can be seen from EBSD that the average grain size of the specimen was about 16 μm with few deformation twins, shown in Figure 1.41.
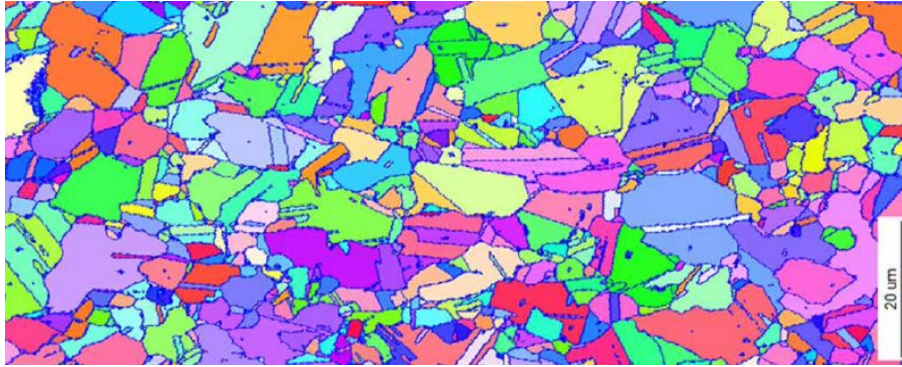
Figure 1.41 EBSD of Cross Section of Aged Inconel 718

Two different group annealed and aged Inconel 718 specimen with diameter 3mm were employed. The specimen was cooled down by air during testing. Annealed specimen exhibited lower fatigue strength compared with the aged group at room and high temperatures. The fatigue strength at high temperature was found to be lower than that of room temperature. However, no significant difference in fatigue strength was found between different high temperatures 300, 500, 700°C.
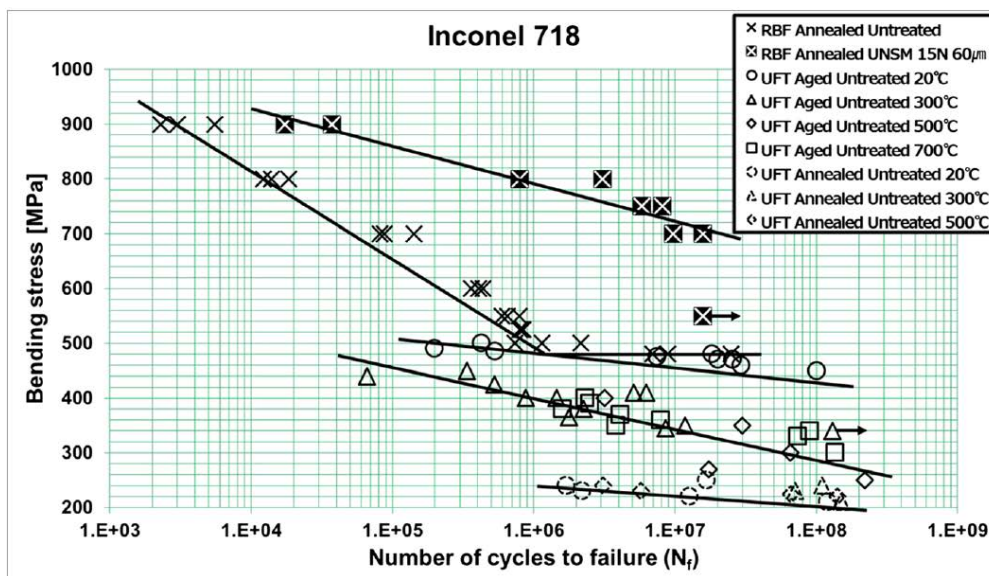
Figure 1.42 Comparison of S–N curve for Annealed and Aged Inconel 718
(RBF: Rotary Bending Fatigue; UFT: Ultrasonic Fatigue Test)

Compressive residual stress was considered to be the most critical factor affecting the improvement of fatigue. The improvement in fatigue life was mainly attributed to the induced compressive residual stress in the subsurface.

It was confirmed that there was inclusion with the size of about 27.5*25 μm that caused the fatigue crack initiation. High concentration of Nb was formed in the inclusion including the other elements such as C, Ni, Ti, Cr and Fe, while the concentration of Ni was the highest in the inclusion near the surface area, shown in Figure 1.43.

Element	Weight%	Atomic%
C K	10.05	43.48
Ti K	5.54	6.01
Cr K	1.84	1.84
Fe K	2.26	2.10
Ni K	5.12	4.53
Nb L	75.18	42.04
Total	100.00	100.00

Element	Weight%	Atomic%
C K	5.60	22.27
Al K	0.84	1.48
Ti K	0.90	0.90
Cr K	18.39	16.90
Fe K	16.46	14.08
Ni K	49.06	39.93
Nb L	5.23	2.69
Mo L	3.53	1.76
Total	100.00	100.00

Element	Weight%	Atomic%
C K	14.37	53.61
Ti K	7.91	7.39
Cr K	1.33	1.15
Fe K	0.89	0.71
Ni K	2.60	1.99
Nb L	72.90	35.15
Total	100.00	100.00

Element	Weight%	Atomic%
C K	18.60	50.47
O K	2.66	5.41
Al K	0.46	0.55
Ti K	0.69	0.47
Cr K	15.60	9.77
Fe K	13.80	8.05
Ni K	41.09	22.80
Nb L	4.37	1.53
Mo L	2.73	0.93
Total	100.00	100.00

Figure 1.43 Fracture Surface of Fish-eye Crack Initiation Point
① ②: 475MPa, $7.5*10^6$, RT; ③ ④: 350MPa, $3*10^7$, 500° C

Texier in 2016

In 2016, Texier, Cormier, et al.[122] investigated the effect of particle NMI (non-metallic inclusion) on crack initiation sensitivity of wrought direct aged Inconel 718 at room temperature. Three different microstructures have been examined at the same strain amplitude in order to understand the influence of NMI, carbide, carbonitride and nitride, and Σ3 twin boundary density on lifetime and failure mode, shown in Figure 1.44. It demonstrated that surrounding grain structure (grain orientation, local plasticity and roughness in the vicinity of crack tip due to pre-straining) played key role in the fatigue life in the nominal elastic regime. The effect of the prior damage on VHCF lifetime was examined by means of introducing "natural cracks" within NMIs prior to VHCF testing.
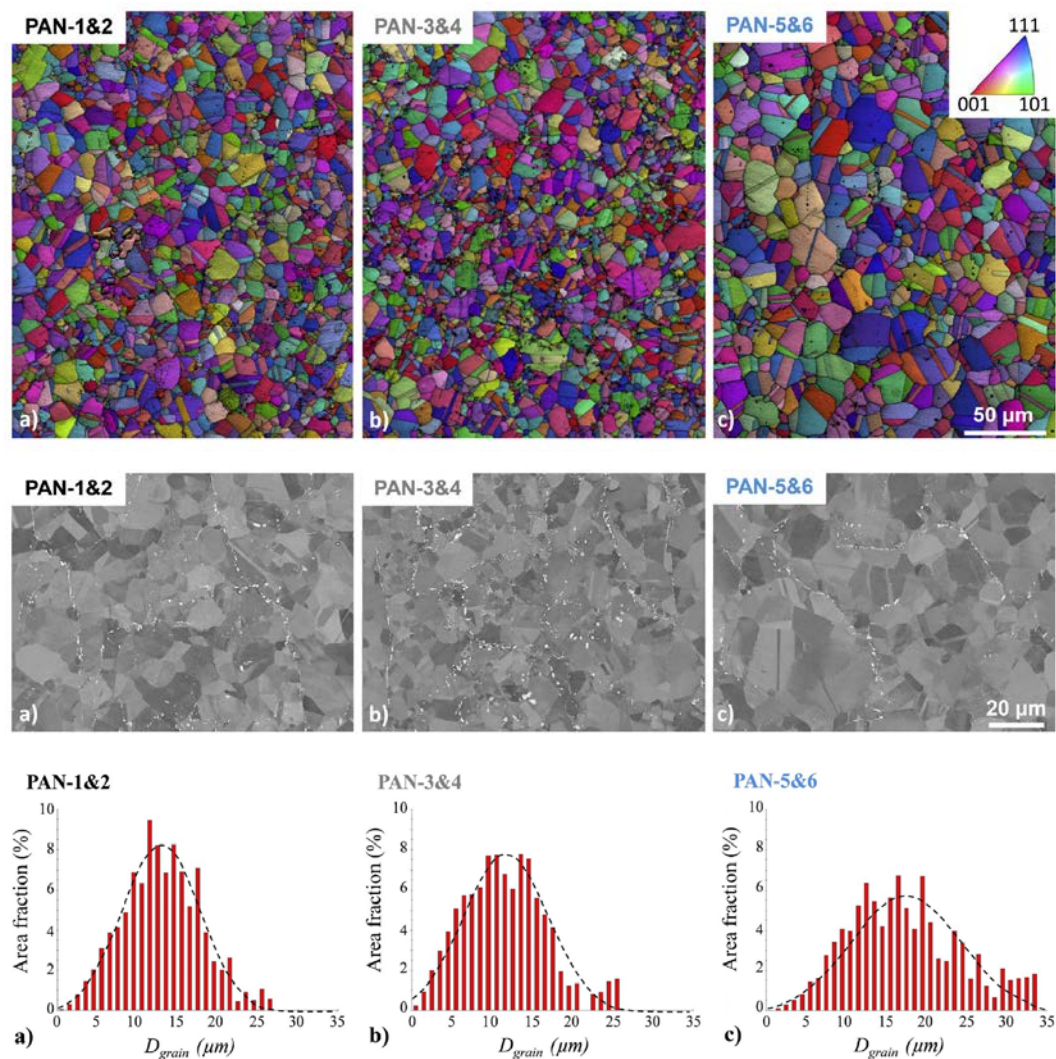
Figure 1.44 Inverse Pole Figure, δ phase and Grain size distribution of 3 microstructures

Tofique in 2016

In 2016, Tofique, Bergstrom, et al.[123] compared very high cycle fatigue crack initiation mechanism in different materials using ultrasonic equipment at 20 kHz. Superalloy Inconel 718 was tested in the forged and heat treated condition, solution treated followed by precipitation hardening. Thus, it typically consists of austenitic grain with Ni_3Al precipitate. The specimen was tested under the load ratio R=0.8.

The study of the fatigue fracture surface displayed an initiation CGR (Crystallographic Growth Region) characterized by growth along favorable oriented slip planes. Initiation point was typically grain boundary triple point. At first appearance the crystallographic faceted surface looked quite smooth but closer study showed stepwise growth of the fatigue crack along the plane. Further away from the initiation point one could more easily distinguish striations but not continuous and still following the crystal plane. Out of the CGR, transgranular fatigue crack growth perpendicular to the applied load took place until the final failure region, shown in Figure 1.45.
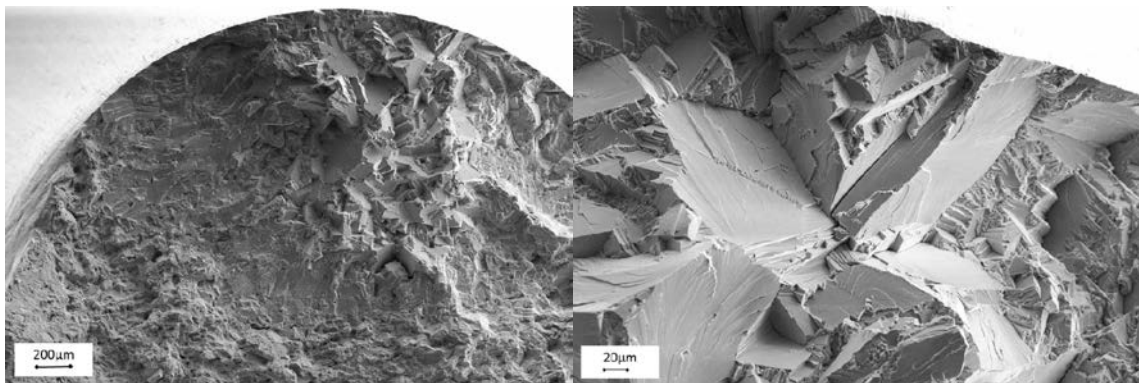
Figure 1.45 Fracture Crystallographic Growth Region of Inconel 718, $3.2*10^9$ cycles

Pineau and Antolovich in 2016

In 2016, Pineau and Antolovich[124] investigated probabilistic approach to fatigue with emphasis on initiation from inclusion. It concentrated on the two problems of microstructural variance and on the effect of component or specimen size in introducing uncertainty. The first part, an attempt was made to summarize the micro-mechanism of crack initiation by the formation of intrusion/extrusion along the slip bands in pure metal. The second part, an attempt was made to account for the dispersion associated with specimen or component size in terms of the interaction between the defect distribution and size when fatigue cracks were initiated from inclusion, shown in Figure 1.46.

The case of Inconel 718, which inclusions were mainly formed by niobium carbide (NbC), was examined in more detail. Fatigue resistance of this material can be simply modelled, knowing the size and the distribution of NbC particles which act as fatigue initiation sites. It was also found that δ phase, grain size, etc. could influence local plastic strains. And non-metallic inclusion at the high end of the size distribution was the most important feature controlling variability.
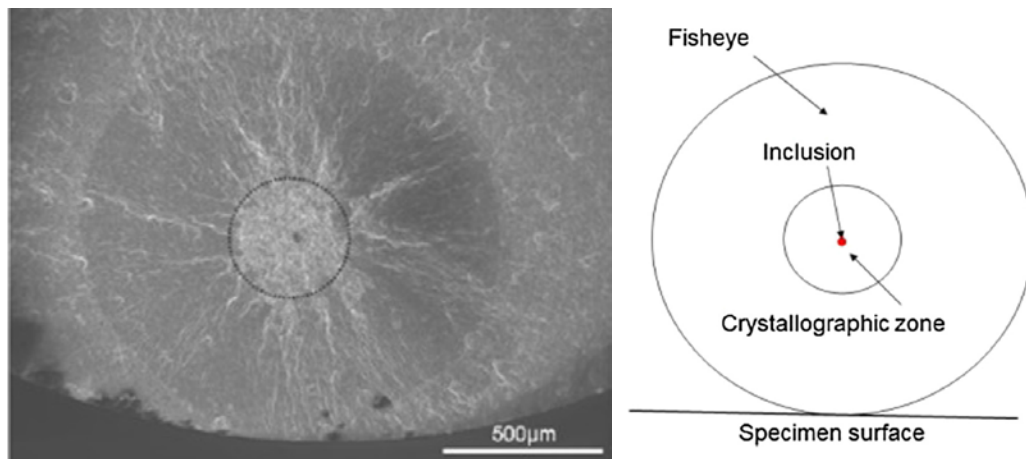
Figure 1.46 Fish-eye Crack Associated FGA Initiated from Internal Inclusion Particle

Chapter II Experimental Devices

The usual experimental procedure for determining fatigue strength is by testing a group of similar specimens, subjecting each one to a particular alternating load until it fails.

Fatigue testing machines can be classified by the type of loading mode that is applied to the specimen. It is direct or axial stress, rotary bending, bending, torsion, and combined multi-axial stress.

It is also divided by the type of loading frequency that conventional mechanic loading with low frequency 0.1~50 Hz, hydraulic or pneumatic machine working up to 200 Hz, and ultrasonic electromagnetic loading at 20 or 30 kHz.

The conventional fatigue tests usually work at the frequency of load system of testing machine. This is always performed under the force vibration condition. In ultrasonic fatigue testing machine, the excited frequency supplied by the testing machine must be one of the natural frequencies of the specimen, deals with free vibration. Only one of the ends of the specimen needs to clump to the test machine, the other is assumed as free. The tests stress or strain distribution is absolutely symmetric R=-1. It is assumed that the materials are isotropic and homogeneous, and it has an elastic behavior during all the cyclic loading.

Moreover, ultrasonic testing machine was capable to carry out just longitudinal tension compression before. With the development of fatigue test equipment, the ultrasonic unit can also combine into the tensile machine for preset static mean stress, achieving the asymmetric test loading R>-1, including tension-tension test.

2.1 Piezoceramic Tension Compression Test Group

As is mentioned before, fully reversed tension compression loading situation is studied in this research, supplied by ultrasonic test system.
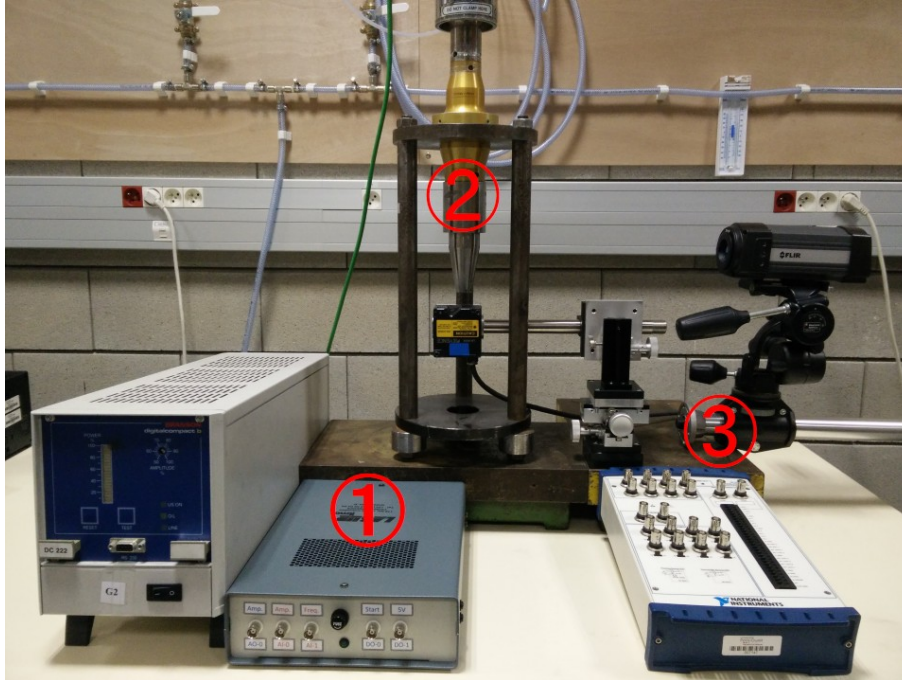
Figure 2.1 VHCF Tension Compression Test Group

The schematic diagram of VHCF test equipment is shown in Figure 2.1. Major components of this system group can be summarized into 3 parts[50, 60]:

1. Control System:

    Computer with National Instrument® PCI internal card and self-programming software that feedback regulation to keep the initial parameters as required.

2. Actuation System:

    Power generator, piezoelectric converter and booster/horn apply the available displacement at one side of specimen as its nature frequency, for obtaining the required strain amplitude, corresponding to the stress, in the middle section of specimen.

3. Acquisition System:

    NI external card driven by LabView™ combines the signals from Branson®, Keyence® laser sensor, and Flir® infrared camera, monitoring the frequency, temperature, displacement and so on for the whole test.

2.1.1 Control System and Calibration

VHCF ultrasonic fatigue test are displacement controlled. In order to control the machine, personal computer with National Instrument® internal PCIe card and self-programming software working on Windows are used. The software allows to impose the electrical signal to command the amplitude, further compare and adjust it with feedback of mechanically vibrated system and change the value if necessary.
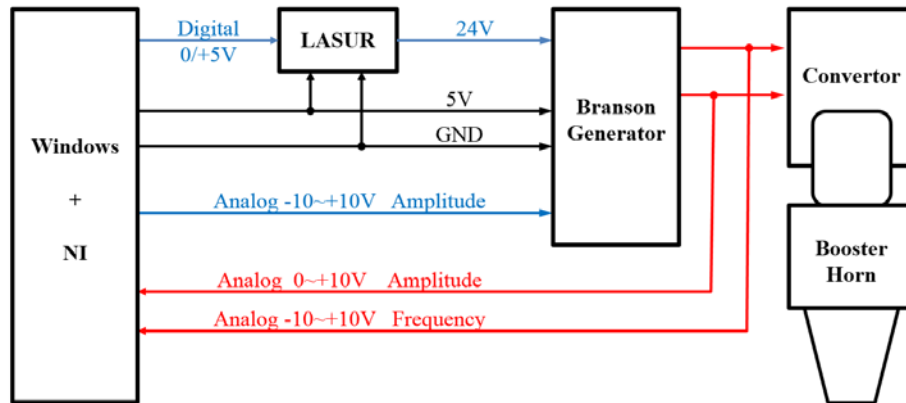
Figure 2.2 Schema of Control System

There are two signals should be decided for input into the actuation system: one digital on the relay to start or stop the test and the other analog for determining displacement amplitude, shown in Figure 2.2. The electric current of this analog signal is nearly 100~150 mA, that means the portable USB NI card cannot provide enough power, it's better to use the PCI edition.

The purpose of calibration is to obtain the relationship between the input voltage and output displacement. After only one calibration, a certain range of loading obtained through only regulating the voltage in the software. According to the previous experience, the input control voltage, output feedback voltage and displacement amplitude always exist linear relation, shown in Figure 2.3.
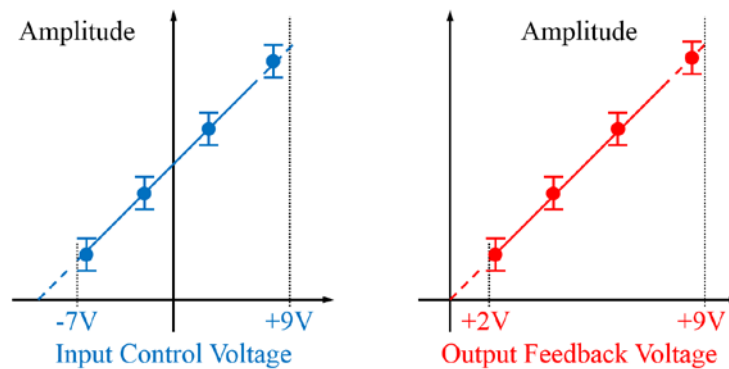
Figure 2.3 Calibration between Electronic Voltage and Mechanic Amplitude

Theoretically, the power generator should work at the range of the control voltage -10~+10V, and corresponding feedback voltage 0~+10V. While, during the practical application, for the steady vibration from the piezoelectric ceramic, it appears preferable to stay the control signal into -7~+9V, and feedback voltage nearly +2~10V. For the special high or low amplitude demand, it should be arranged through changing the suitable horn, instead of setting the voltage.

Frequency is not controlled by setting, but chosen automatically by the Branson® UPS™ software, according to the minimum total energy consuming, as well as minimum current (red). Displacement amplitude keeps maximum (green) and the phase changes also at this point (black). No matter scan from forward or backward, this frequency shows the same value, shown in Figure 2.4.
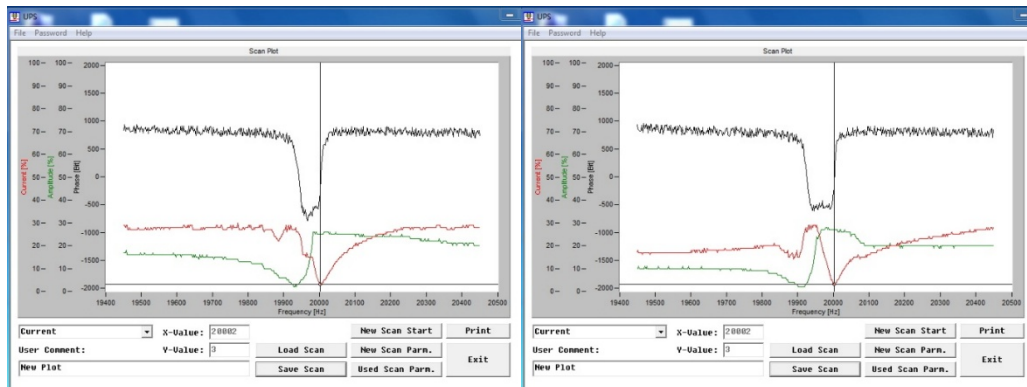
Figure 2.4 Forward and Backward Frequency Scan by Branson UPS

This frequency adjusted itself automatic during the test keeping the power frequency always at the nature frequency of the whole system. As well known, specimen temperature will rise more or less, due to internal frictional of material under high strain rate. Dynamic modulus of material deceased as temperature increased, as well as the resonance frequency. The nominal resonance frequency of system must be in the 20000±500 Hz, (In fact, the DC 222 edition in LEME is 19450~20450 Hz).

The criterion for judgment of the crack is that the frequency of whole system went out of this range due to crack initiation and propagation (-500 Hz), so that the power will be cut. It is necessary to point out that the specimen maybe still linked when group stopped, the fracture don't propagate to all the section yet. In contrast, for the smaller or lighter specimen, the frequency maybe still keeps in this range, even if the half of the specimen dropped down.

2.1.2 Actuation System

The schematic diagram of actuation system shows in Figure 2.5. Two curves are drawn to display the stress and displacement amplitude at different parts.
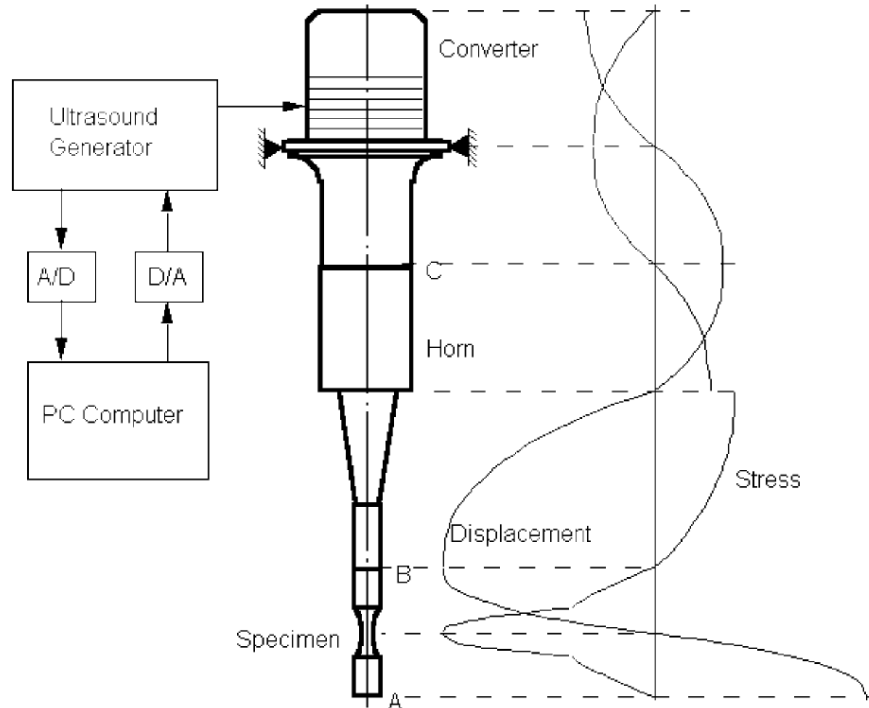
Figure 2.5 Schema of Actuation System with Stress and Displacement Field[50]

The schematic diagram of actuation system can be summarized into:

● Power Generator:

Power generator receives the control signal (≈100mA) from the NI card, and generates sinusoidal electrical signal from 50~60Hz civil electricity at the nature frequency of the system nearly 20 kHz. The maximum power of Branson generator is 2kW.

● Piezoelectric Converter:

Piezoelectric Converter is excited by the power generator, and transforms the electrical energy into mechanical ultrasonic longitudinal mechanical vibration wave at the same frequency. The wave amplitude directly from piezoceramic is small (several micron). There are two signal feedback from the convertor, one for amplitude and the other for frequency.

- Booster & Horn (Sonotrode):

The role of the booster is to provide a plane for arrange the whole group, and at the same time, increase a little bit the wave amplitude ($\approx$1.2). Due to the vibration amplitude directly from piezoelectric ceramic is so small, the horn (also called as sonotrode) is needed to amplify this value from several micron to tenths of micron, available for the required strain and stress amplitude in the test section of specimen.
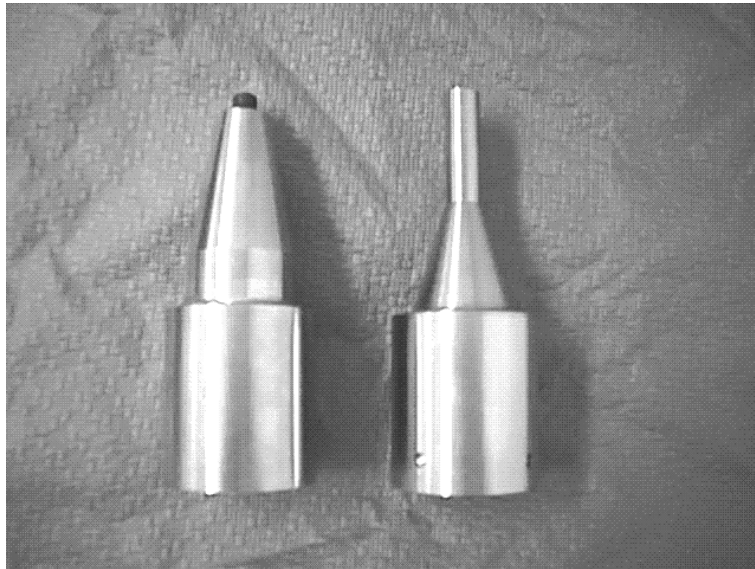
Figure 2.6 SC and TGD Sonotrode

SC sonotrode is standard device with an amplification factor of nearly 2.4, TGD sonotrode is high amplification sonotrode with the factor from 8 to 10, shown in Figure 2.6. Specimen is connected at the end of the horn by M5 screw.

Indeed, ultrasonic testing machine is also capable for asymmetric test, including tension-tension test R>0, through assembling into the tensile machine for preset static mean stress. For this situation, two same booster and horn should be ranged as mirror to the specimen, while only one piezoelectric converter at the top supplies the longitudinal vibration stress.

2.2 Acquisition System

Laser sensor and infrared camera are applied to measure and analyze the vibration mode, deformation, prolongation, temperature due to self-heating phenomenon and so on during the fatigue testing, shown in Figure 2.7.

Two probes of laser sensor are used at same time for revealing the vibration mode of the specimen. One is set at the bottom of the specimen; the other is set at the bottom of the horn. The bottom surface of horn and the top surface of specimen have been considered with same vibrating situation. The upper probe is rotated nearly 30º, due to the geometry obstacle. After experimental converted calibration, it can be used as normal.
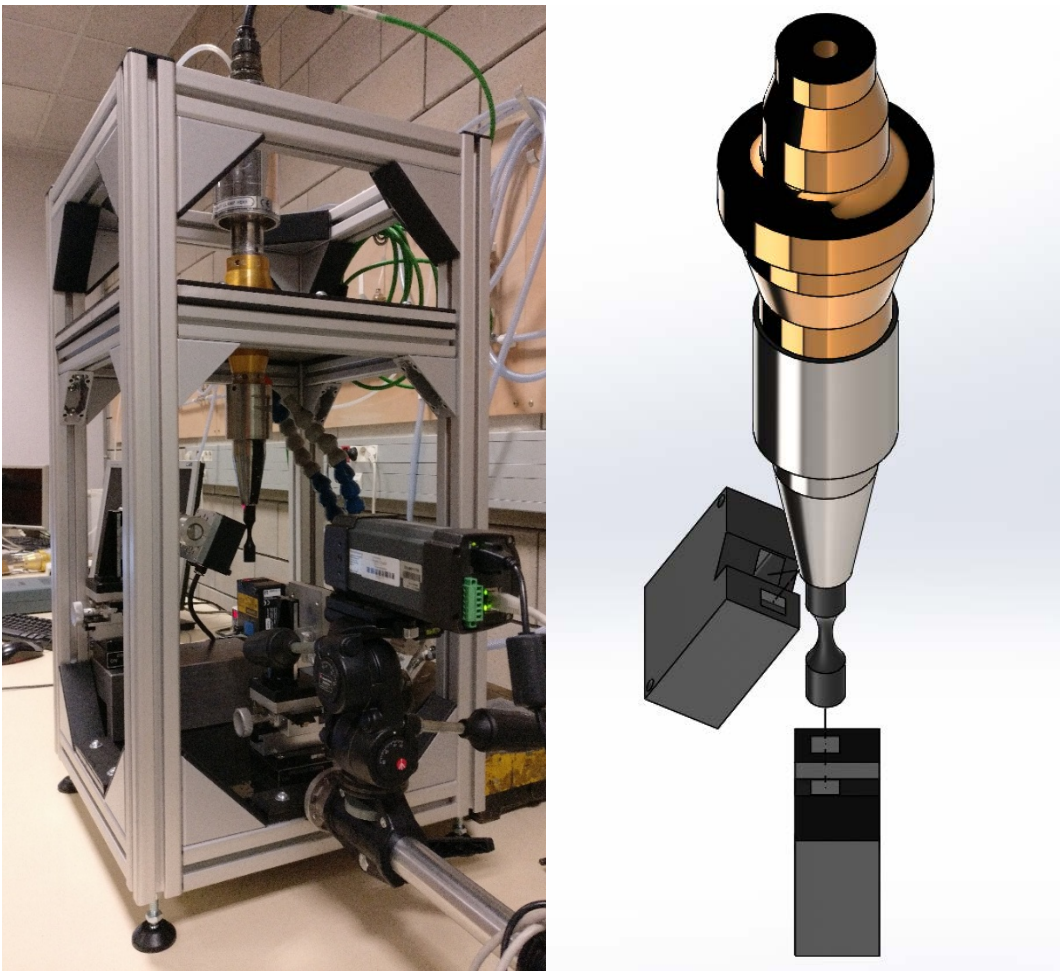
Figure 2.7 Schema of Acquisition System
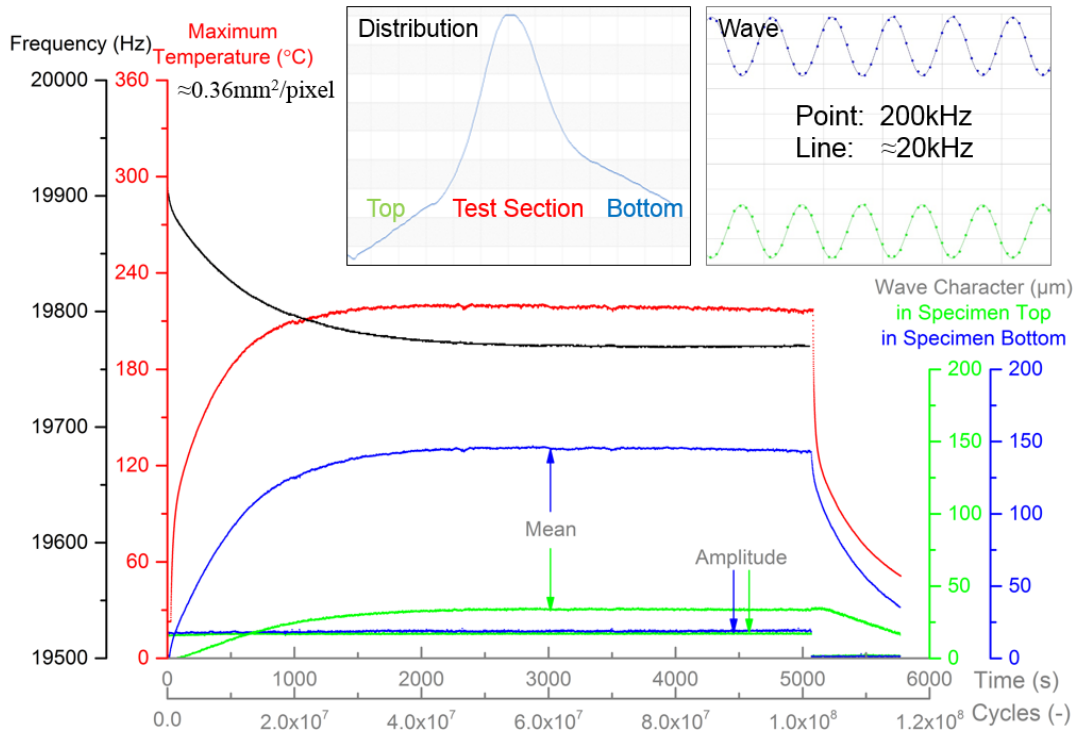
Figure 2.8 Summary of Data Acquisition

There are 4 main parameters are monitored during the test, shown in Figure 2.8:

● Resonance Frequency (Black):

Calculated from the feedback voltage;

● Maximum Temperature (Red):

Chosen from the all the pixel on infrared image;

● Amplitude of vibration wave (Two probes):

The wave amplitude on the top and bottom of the specimen were nearly same. Value obtained from the top probe is in green, which from bottom is in blue;

● Mean value of the vibration wave (Two probes):

The position of the top of specimen goes down slightly, because the horn and booster become a little longer due to be heated, corresponding to the mean value in green increased slightly;

At the same time, the position of the bottom of specimen goes down obviously, because the specimen became longer due to its self-heating, corresponding to the mean value in blue increases obviously.

The difference of these two values is the elongation of the specimen, its tendency shows also in the Section 2.2.1.

2.2.1 Laser Sensor

Inconel 718 dissipates numerous energy under high strain rate during the test. The conventional optic displacement sensor which calculates the displacement by reflected light intensity at different position, is not suitable for this kind of test. Because the emissivity changes also as the specimen surface temperature changes. The temperature is sometimes higher than 100ºC during the test. Contact strain gauges is not easy to calibration owing to the same reason. The non-contact laser sensor is chosen for the experimental research.

Keyence® LK-G5001P series sensor with two LK-H022 probes is employed for the test. The maximum detected frequency is up to 392 kHz. While during the practical application, 200 kHz is used generally taking accuracy and memory consumption into account at the same time. For measured vibration nearly 20 kHz, there are 10 points to description one sinusoidal wave in average. The working range of this probe is 20±3 mm, with repeatability of 0.02 μm.

The correctness (not accuracy) of this new laser sensor is verified by another believable mechanical micrometer. The micrometer is fixed on a frame and the laser point is focused on the spindle surface. Two groups of data from the sensor software and micrometer screen can be obtained when turning the ratchet continuously. Good agreement means that the laser sensor probe with present fixture is suitable for the fatigue test.
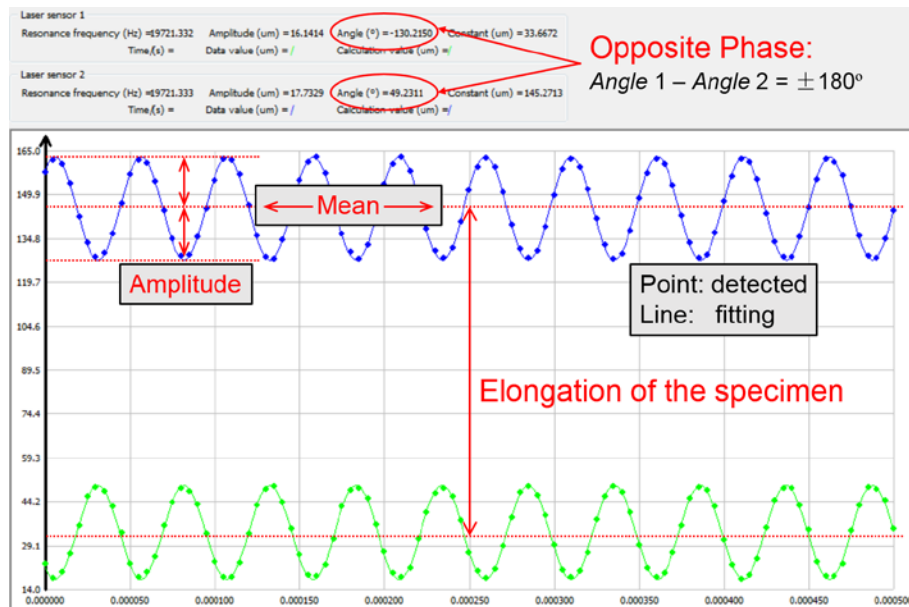
Figure 2.9 Original Wave Obtained from Laser Sensor

Besides amplitude and mean value of vibration shows in the summary, all the real wave during the test is also recorded, shown in Figure 2.9. The points are detected directly from the sensor probe, and the line is fitting. Perfect agreement shows the steady vibration during all the test, and the opposite phase proved the fully reversed tension-compression mode (R=-1) of the specimen.

The difference of mean values between the top and bottom probes allows to assess the elongation of the specimen caused by self-heating phenomenon, shown in Figure 2.10 (violet). It can be compared with another value by integration the thermal expansion, in the next Section 2.2.2.
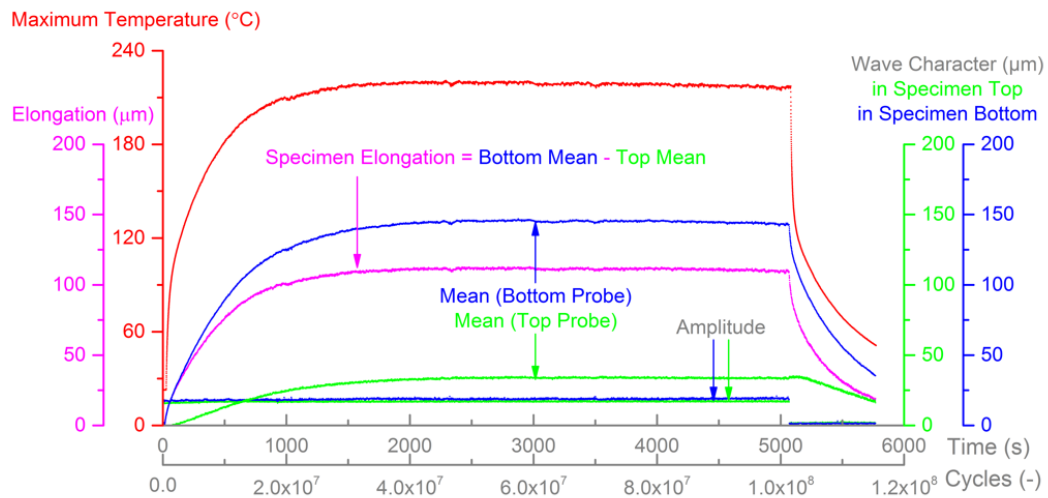
Figure 2.10 Elongation of Specimen during the Test

The wave frequency is obtained from the FFT calculation of the fitting line. The Fourier transform decomposes the signal as the function of time into the frequencies that make it up, shown in Figure 2.11.

$$\begin{cases} y(t) = \int_{-\infty}^{+\infty} \hat{y}(f) \cdot e^{2\pi i f \cdot t} df \\ \hat{y}(f) = \int_{-\infty}^{+\infty} y(t) \cdot e^{-2\pi i t \cdot f} dt \end{cases} \tag{2.1}$$
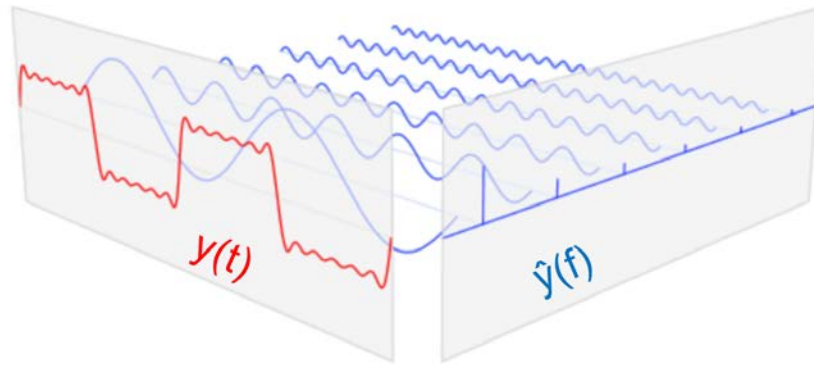
Figure 2.11 Schema of FFT

For sinusoidal vibration during the ultrasonic fatigue test, it can be simplified as Equation (2.2):

$$y(t) = \sum_{n=1}^{\infty} A_n \sin(2\pi f_n t) = \cdots + A_{max} \sin(2\pi f_{res} t) + \cdots \tag{2.2}$$

Resonance frequency of the detected wave is treated as the frequency of the component with maximum amplitude, shown in Figure 2.12. It can be compared with another frequency from feedback voltage on the ceramic. According to the previous research, the maximum difference between these two values don't exceed 50 Hz, less than 1%.
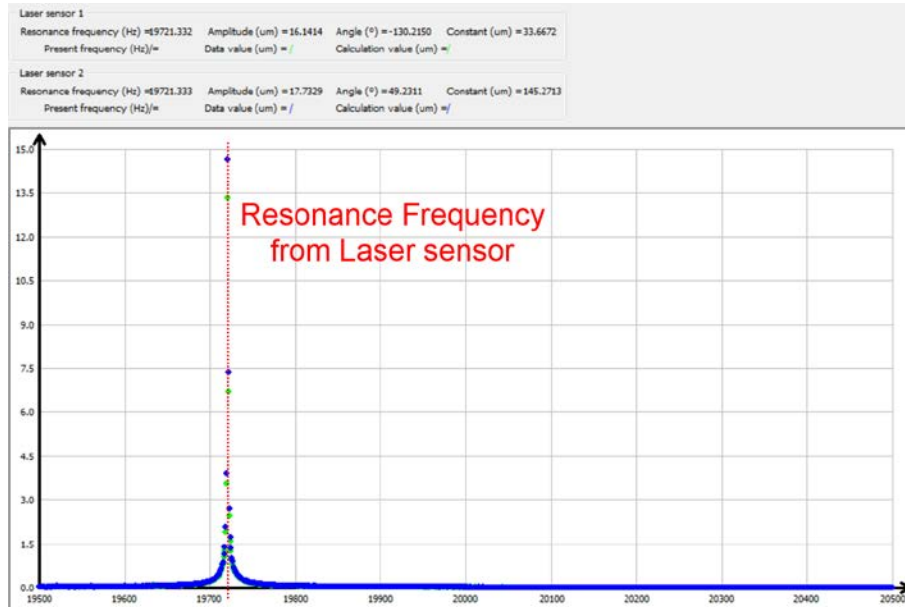
Figure 2.12 Frequency Calculated from Laser Sensor by FFT

2.2.2 Infrared Camera

Flir[®] A325sc infrared camera is chosen for the test. The working range of spectral band is 7.5~13 μm, and the resolution of this camera is 320*240 pixels. There are two default test temperature range can be chosen, -20~+120 or 0~360ºC. The precision of this camera is less than ±2ºC or 2% of the detected value, which is enough for the fatigue research considering the price.

The camera is also verified by our own laboratory. Test material bulk black painted has been put into the large heater with high precision. The detected value from infrared camera is really close to the demand heating temperature. It means that Inconel 718 with present black painting is suitable for the non-contact measurement by infrared camera.

In the practical application, when observed the higher temperature, the horn should be monitoring with the specimen together (lower zoom), making sure the heat didn't transfer so much to the ceramic. When observed the moderate temperature, the camera is set close enough as possible to the specimen for the finest resolution (higher zoom), shown in Figure 2.13. At that time, the total width of the image is nearly 90mm into 360 pixels, it means the value reading from the software is averaged in one pixel with 0.06 mm^2.
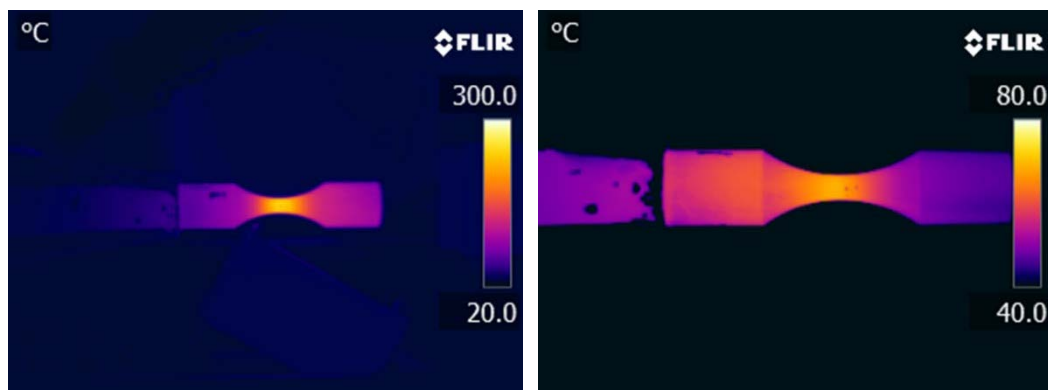
Figure 2.13 Lower and Higher Zoom Image by Infrared Camera

Maximum temperature of all the specimen is chosen as characterization of the self-heating phenomenon at ultrasonic loading at 20 kHz, because the black painting maybe chip after enough long time vibration at high frequency, even if "700 ℃" is written on the bottle of black painting. Specimen is well polished before the test for avoid stress concentration, but it is adverse for painting attachment. Mean value and the minimum of temperature will be unstable if the painting drops down, shown in Figure 2.14.
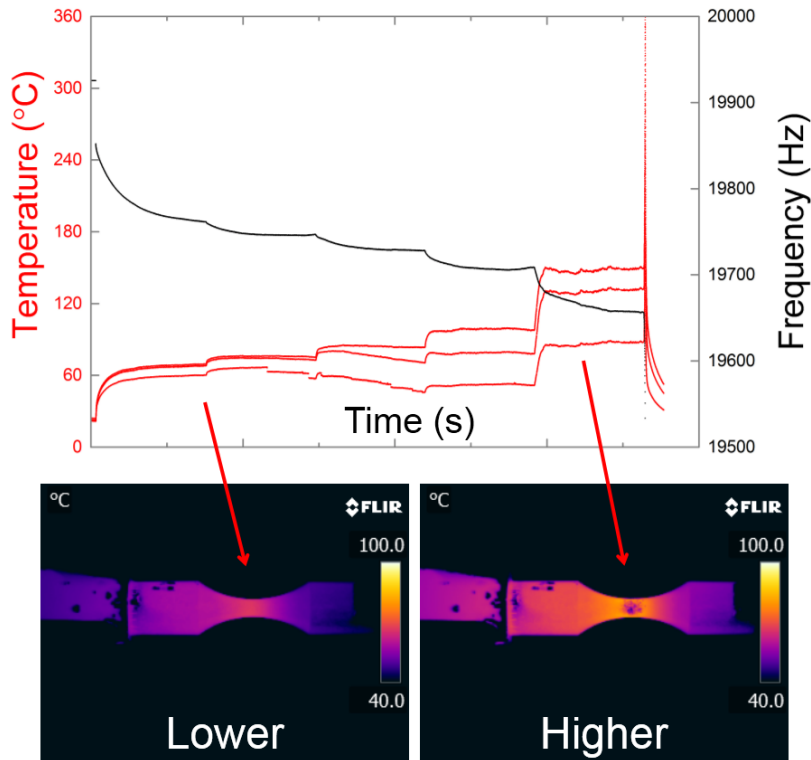
Figure 2.14 Painting Crack at High Frequency Loading

Besides the maximum temperature of all the image has shown in the summary, all the points which face to camera has been also recorded, shown in Figure 2.15. Heat generates mainly in test section at the beginning of the test, then conducts gradually through the specimen until steady distribution with the balance between heat generation and dissipation of all the specimen. Enormous heat exhausts in the fracture point (not shown in the figure, the detection limit is 360℃) and temperature decreases to RT after machine stop caused by specimen break.

For the safety of the piezoelectric ceramic, two cooling air gun are ranged between the horn and booster generally. Even if they are far from the specimen, there is still some influence on the specimen temperature, not fully symmetrical, marked in Figure 2.15.
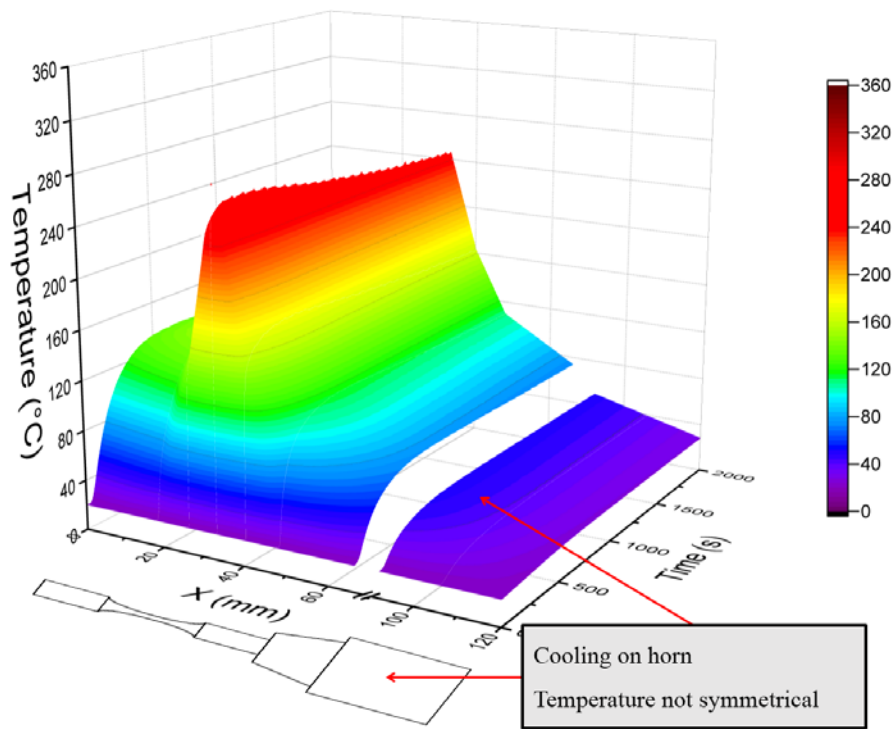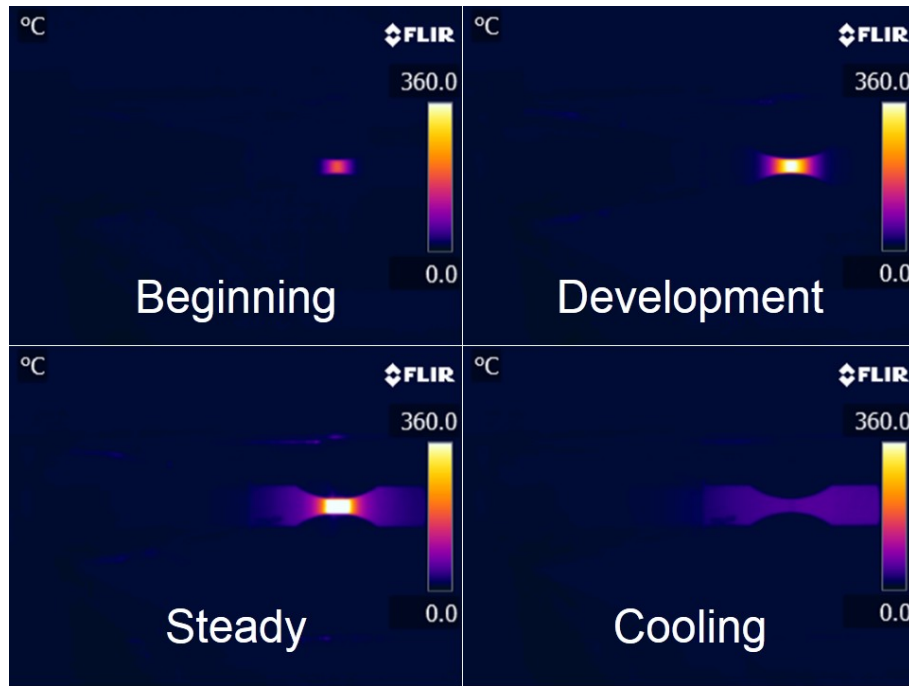
Figure 2.15 Temperature Distribution depending of Cycling

Elongation of specimen can also calculate by integration the thermal expansion along the specimen. It can be validated with the other one come from the laser sensor. Verification between these two values shows in Figure 2.16.
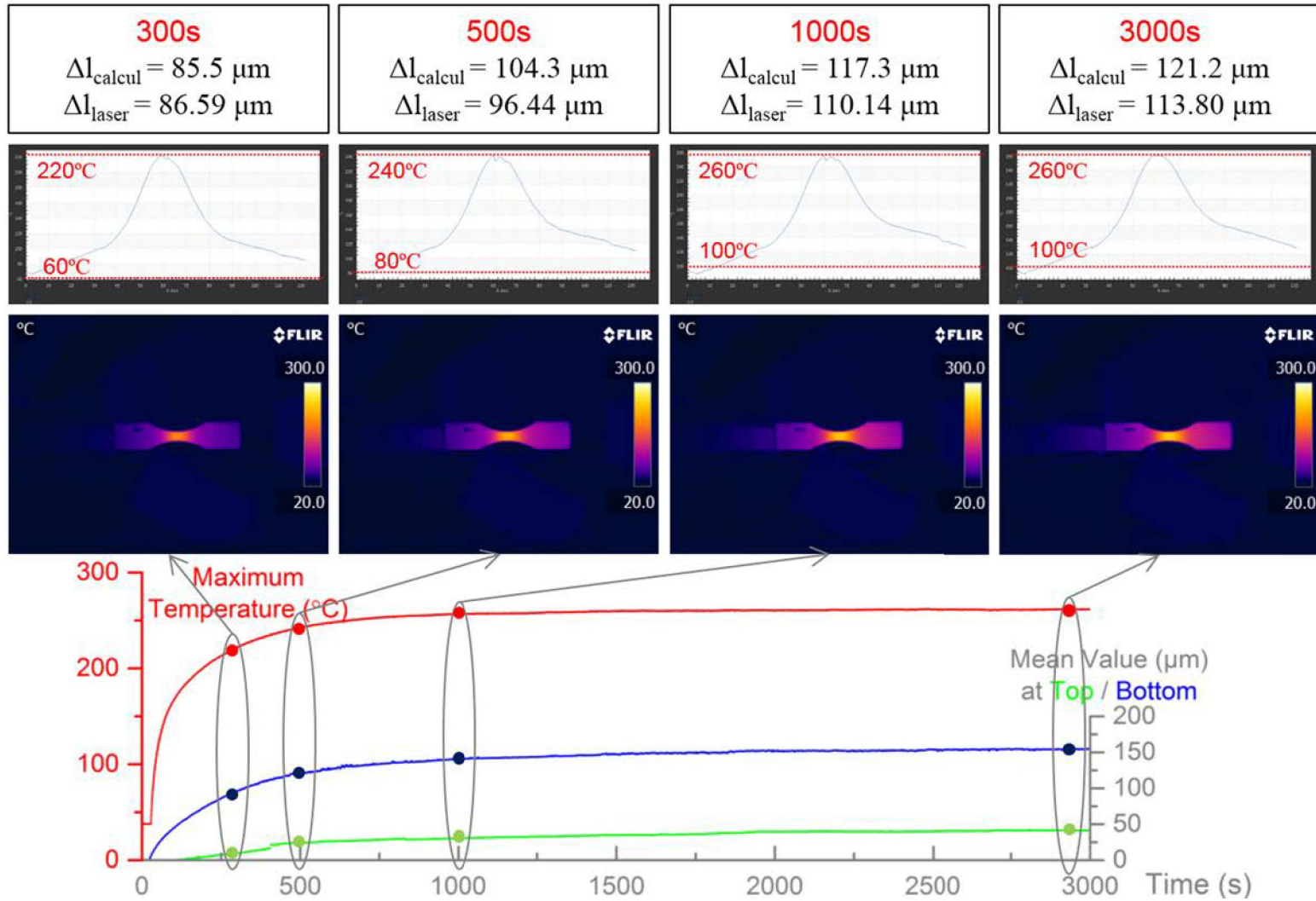
Figure 2.16 Elongation Verification of Inconel 718 with Self-heating Phenomenon at 20 kHz

2.3 Cooling & Pulse-Pause Mode

Air and water cooling are also tested in the project, for some potential test excluding the effect of self-heating in the future.

CompAir® Delcos Pro™ air compressor is used in this test. Air is inhaled from surrounding and compressed up to 8 bar, then imported into Beko® Drypoint™ and Clearpoint™ filter for dry clean cooling air. Temperature of cooling air at the exit of the filter is 3.5ºC, but it will change slightly after long tube and tap. Cooling air is imported into the convertor for cooling the piezoceramic, and also on test section of specimen surface. The maximum massflow is 200 L/min. It is still not enough to offset the temperature increase due to self-heating of Inconel 718 at 20 kHz.

Distilled water with anti-corrosion additive is pumped and spouted on the test section of specimen. (Massflow is not detected). Due to the ultra high convective heat transfer coefficient of water than air, the specimen keeps nearly RT during all the test. (At this time, the real temperature of specimen cannot be obtained. Constant resonance frequency of all the group during the test inclines the fixed temperature of specimen at nearly RT.)

Disadvantage of water cooling is that the infrared camera and laser sensor cannot work anymore because the existence of water layer. So it is better to find way to suppress the temperature increase without additional cooling.
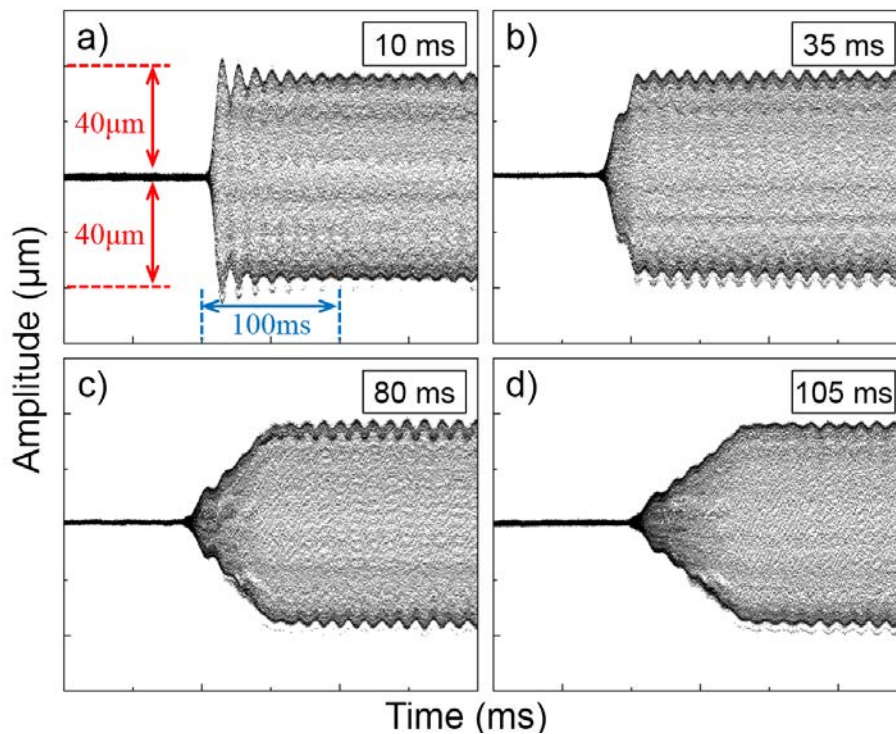
Figure 2.17 Original Wave with 4 Different Startup Ramp

Pulse-pause mode is also applied in this project for solving the disadvantage of air and water cooling. The main thinking of pulse-pause mode is to prolong the heat transfer duration (convention and radiation), but shorten heat generation time. There are 4 options of startup ramp in the Branson® power generator: fast 10ms; middle 35 ms; standard 80 ms and slow 105 ms. Tested wave amplitude is 40 μm. Original wave of 4 different startup ramp time are shown in Figure 2.17. Obvious overload (nearly 10%) appears at the beginning of fast ramp case (a). That is absolutely prohibited in VHCF fatigue test. So the middle startup ramp duration of 35 ms is chosen for the next pulse-pause mode test.
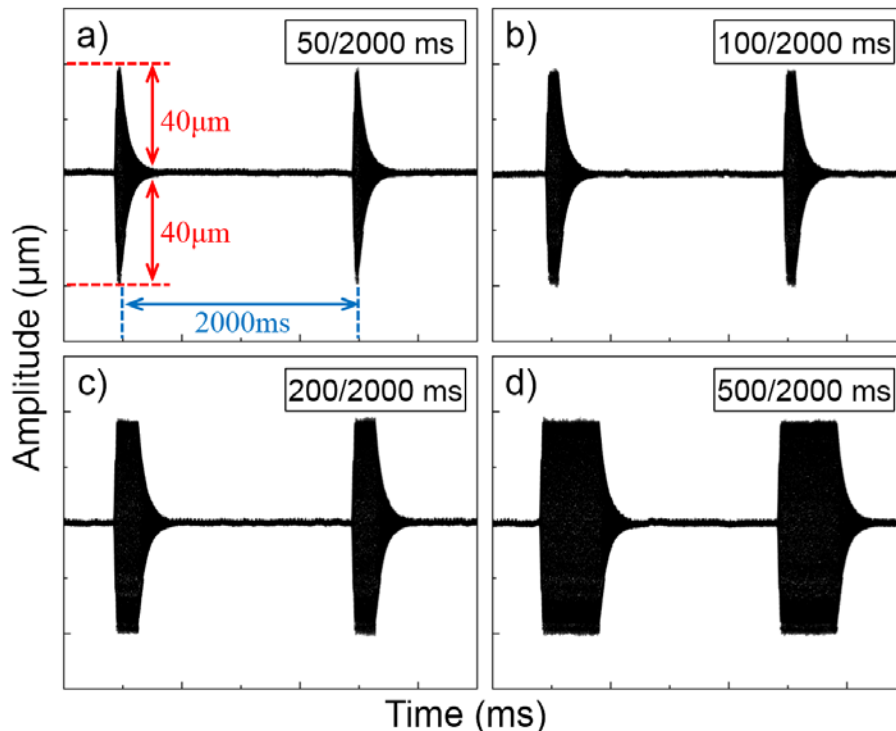
Figure 2.18 Original Wave with 4 Different Pulse Duration

The proportion of pulse time in the total cycle is another important parameter. Original wave of different pulse duration 50, 100, 200 and 500ms in total cycle time of 2000 ms are shown in Figure 2.18. For the short pulse time (a) and (b), the wave shape is not enough steady. While, for the long pulse time (c) and (d), majority of wave is at the required amplitude.

On certain conditions, for the same material with same loading stress, stationary temperature increase under continuous loading mode is 100 ℃. While, temperature of specimen surface keeps nearly room temperature during the test under 200/2000 ms and increases less than 5℃ under 500/2000 ms mode.

2.4 Specimen Design

For resonance with the test device, specimen is designed in analytical and validated in numerical way.

2.4.1 Theoretical Calculation

The analytic method used to design the specimen under following hypothesis:

● Test material being studied is homogeneous and isotropic;

● Pure elastic without plastic deformation is considered during all the test (Test stress was much smaller than yield stress at VHCF long life regime);

● Vibration wave is longitudinal, the theoretical analysis can be simplified to one dimension;

● Gravity is neglected.

Uniform Section Cylinder (1D)

Without loss of generality, the one dimension case of straight cylinder with longitudinal elastic axial wave vibration can be discussed to simplify calculations. The elastic wave comes from one end of the bar and travels through the length than it reflected from one the other end and returns to the initial place of entrance.
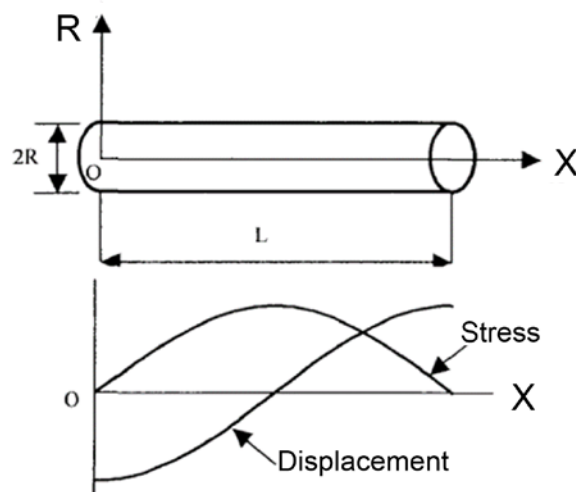
Figure 2.19 Displacement and Stress Distribution in Cylinder Bar

The differential equations are reduced to single equation only for X axis, as (2.3):

$$\rho S \frac{\partial^2 u(x,t)}{\partial t^2} = \frac{\partial F}{\partial x} = E_d S \frac{\partial^2 u(x,t)}{\partial x^2} \tag{2.3}$$

$$\frac{\partial^2 u(x,t)}{\partial t^2} = \frac{E_d}{\rho} \frac{\partial^2 u(x,t)}{\partial x^2} \tag{2.4}$$

The general solution for this equation is given by (2.5):

$$u = \sum_{n=1}^{\infty} u_n(x,t)$$

$$= \sum_{n=1}^{\infty} \left(A_{n-1} \cos \frac{n\pi c}{l} t + B_{n-1} \sin \frac{n\pi c}{l} t \right) \cos \left(\frac{n\pi}{l} x \right) \tag{2.5}$$

The longitudinal wave velocity could be determined directly with $v=0$ for consideration of 1D example as (2.6) and (2.7):

$$c_{long} = \sqrt{\frac{E(1-v)}{\rho(1+v)(1-2v)}} \tag{2.6}$$

$$c_{1D} = \sqrt{E_d / \rho} \tag{2.7}$$

The boundary conditions of ultrasonic fatigue testing requires the displacement to be maximum at both ends whereas the strain disappeared at the same place, shown as Equation (2.8):

$$u\big|_{x=0,l} = \pm A_0, \quad \frac{\partial u}{\partial x}\bigg|_{x=0,l} = 0 \tag{2.8}$$

The special solution for first mode of vibration (**n**=1) could be determined, the displacement **u**, strain **ε**, strain rate **ε̇** and stress **σ** shown as:

$$u(x,t) = A_0 \sin(\omega t)\cos(\kappa x) \tag{2.9}$$

$$\varepsilon(x,t) = \frac{\partial u}{\partial x} = -\kappa A_0 \sin(\omega t)\sin(\kappa x) \tag{2.10}$$

$$\dot{\varepsilon}(x,t) = \frac{\partial \varepsilon}{\partial t} = -\kappa \omega A_0 \cos(\omega t)\sin(\kappa x) \tag{2.11}$$

$$\sigma(x,t) = E_d \cdot \varepsilon = -\kappa A_0 E_d \sin(\omega t)\sin(\kappa x) \tag{2.12}$$

where

$$\omega = \frac{\pi c}{l}; \quad \kappa = \frac{\omega}{c} = \frac{\pi}{l} \tag{2.13}$$

and A_0 is displacement amplitude at the ends of the bar, E_d is dynamic modulus for consideration of dynamic effect. As the boundary condition requires, displacement vanishes, strain and stress are maximum in the middle of cylindrical bar of length **x**=l/2, shown as Equation (2.14):

$$u = 0; \quad \sigma_{max} = -\frac{\pi}{l}A_0 E_d \tag{2.14}$$

At the both ends of the cylinder, the displacement is maximum, strain and stress are vanished when **x**=0,l, shown as Equation (2.15):

$$u_{max} = A_0; \quad \sigma = 0 \tag{2.15}$$

Stress-Amplitude Coefficient can be defined as (2.16):

$$C_s = \left|\frac{\sigma_{max}}{u_{max}}\right| = \frac{\pi E_d}{l} \tag{2.16}$$

The analytical solution for straight cylindrical bar is finished. During the experimental test under resonance, the excite frequency should be same with the nature frequency of the specimen, as (2.17):

$$f_{excite} = f_{nature} = \frac{\omega}{2\pi} = \frac{1}{2l}\sqrt{\frac{E_d}{\rho}} \qquad (2.17)$$

While in the practical application, the frequency of excitation signal coming from generator and convertor is already fixed when fabricated in factory. Resonance condition could be achieved through adjust the length of specimen. Resonance length has been defined as (2.18):

$$l = \frac{1}{2f_{excite}}\sqrt{\frac{E_d}{\rho}} \qquad (2.18)$$

This equation reveals an important fact: the resonance length is inversely proportional to the excite frequency, which explained why some very high frequencies are not practicable, because the size of specimen should be too small. One simple calculation for cylindrical steel bar shown that, the specimen length is around 12.8 mm when working at resonance 200 kHz.

At the same time, taking the human auditory perception into account, the excite frequency should be keep away from 20~18000 Hz, for avoiding the noise. The most common ultrasonic test machine operates at 20k or 30 kHz.

Variable Section Hourglass Specimen (2D)
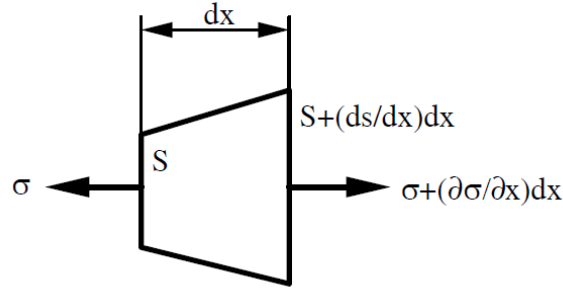
Figure 2.20 Differential Vibration Element

For fatigue specimen with variable section, section area is not constant, but varies along the axial direction $S=S(x)$. The differential vibration equation is more complex than 1D uniform situation, as (2.19) and (2.20):

$$\rho S(x)\frac{\partial^2 u(x,t)}{\partial t^2} = \frac{\partial F(x,t)}{\partial x} = \frac{\partial}{\partial x}\left[E_d S(x)\frac{\partial u(x,t)}{\partial x}\right] \qquad (2.19)$$

$$\frac{\partial^2 u(x,t)}{\partial t^2} = \frac{E_d}{\rho}\left[\frac{\partial^2 u(x,t)}{\partial x^2} + \frac{S'(x)}{S(x)}\frac{\partial u(x,t)}{\partial x}\right] \qquad (2.20)$$

For the harmonic stationary wave during the fatigue test, the displacement of the specimen can be written as (2.21):

$$u(x,t) = u(x)e^{i\omega t} \qquad (2.21)$$

Then differential equation (2.20) could be simplified as (2.22):

$$\frac{\partial^2 u(x)}{\partial x^2} + \frac{S'(x)}{S(x)}\frac{\partial u(x)}{\partial x} - \frac{\omega^2}{E_d/\rho}u(x) = 0 \qquad (2.22)$$

assume that

$$\kappa = \frac{\omega}{c} = \frac{2\pi f}{\sqrt{E_d/\rho}} \qquad (2.23)$$

so that
$$\frac{\partial^2 u(x)}{\partial x^2} + \frac{S'(x)}{S(x)} \frac{\partial u(x)}{\partial x} - \kappa^2 u(x) = 0 \tag{2.24}$$

That is the simplified differential equation (2.24) of the mechanical longitudinal and planar wave for the variable section specimen.

The geometry of the specimens under VHCF vibrating fatigue is usually designed with an hour glass axisymmetric profile, due to the larger stress amplification coefficient generated by hourglass shape, and the maximum stress stabilized in the middle section, shown as Figure 2.21.
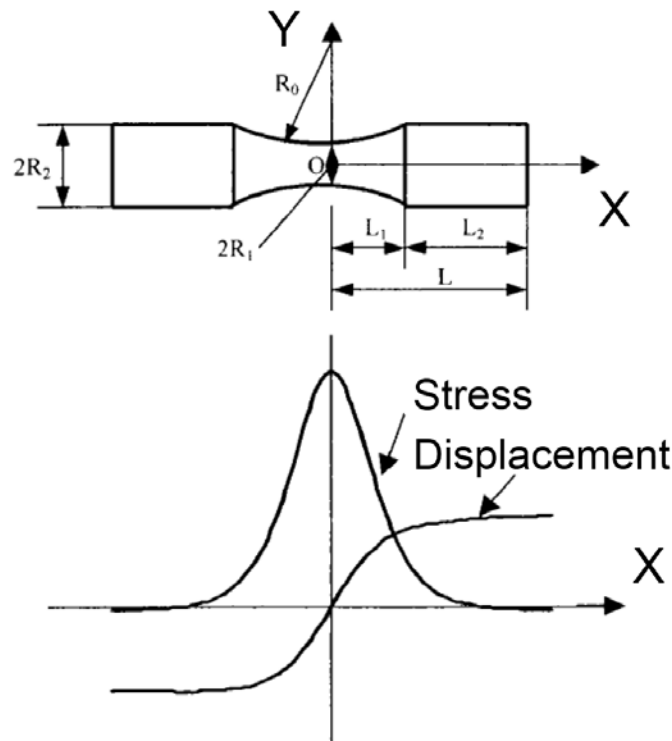
Figure 2.21 Displacement and Stress Distribution in Hourglass Specimen

For facilitating the manufacture processing, the reduced section in the middle of specimen is treated as circular arc, the diameter could be written as (2.25):

$$R_0^2 = \left(R_0 + R_1 - R_2 \right)^2 + L_1^2 \tag{2.25}$$

$$R_0 = \frac{\left(R_2 - R_1 \right)^2 + L_1^2}{2 \left(R_2 - R_1 \right)} \tag{2.26}$$

While for the numerical solution with integration, the reduced section is approximated to hyperbolic cosine, as (2.27):

$$y(x) = \begin{cases} R_1 \cdot \cosh(\alpha x) & 0 < |l| < L_1 \\ R_2 & L_1 < |l| < L_1 + L_2 \end{cases} \tag{2.27}$$

then

$$\frac{S'(x)}{S(x)} = \frac{(\pi y^2)'}{(\pi y^2)} = \begin{cases} 2\alpha \tanh(\alpha x) & 0 < |l| < L_1 \\ 0 & L_1 < |l| < L_1 + L_2 \end{cases} \tag{2.28}$$

where

$$\alpha = \frac{1}{L_1} \cosh^{-1} \frac{R_2}{R_1} \qquad \beta = \sqrt{\alpha^2 - \kappa^2} \tag{2.29}$$

The solution for the equation is given by (2.30):

$$u(x) = \begin{cases} A_0 \cdot \dfrac{\cos(\kappa L_2) \cosh(\alpha L_1)}{\sinh(\beta L_1)} \cdot \dfrac{\sinh(\beta x)}{\cosh(\alpha x)} \\ A_0 \cos[\kappa(L_1 + L_2 - x)] \end{cases} \tag{2.30}$$

The boundary conditions show as (2.31):

$$u\big|_{x=0} = 0, \ u\big|_{x=L} = A_0, \ \frac{\partial u}{\partial x}\Big|_{x=L} = \sigma_{max}, \ \frac{\partial u}{\partial x}\Big|_{x=L} = 0 \tag{2.31}$$

The continuous condition is (2.32):

$$u\big|_{x \to L_1^+} = u\big|_{x \to L_1^-} \tag{2.32}$$

The resonance length of the specimen is defined as (2.33):

$$L_2 = \frac{1}{\kappa} \tan^{-1}\left[\frac{\beta \coth(\beta L_1) - \alpha \tanh(\alpha L_1)}{\kappa} \right] \tag{2.33}$$

Similar to the last cylinder bar, at the both ends of the hourglass shape specimen, the displacement is maximum, stress is vanished at $x=L_1+L_2$, as (2.34):

$$u_{max} = A_0; \quad \sigma = 0 \tag{2.34}$$

The displacement vanishes and stress obtains maximum in the middle of the specimen when $x=0$:

$$u = 0 \quad \sigma_{max} = -\beta A_0 E_d \frac{\cos(\kappa L_2) \times \cosh(\alpha L_1)}{\sinh(\beta L_1)} \tag{2.35}$$

Stress-Amplitude Coefficient can be defined as Equation (2.36):

$$C_s = \left| \frac{\sigma_{max}}{u_{max}} \right| = \beta E_d \frac{\cos(\kappa L_2) \times \cosh(\alpha L_1)}{\sinh(\beta L_1)} \tag{2.36}$$

The stress concentration factor of hourglass specimen is calculated by FEM software ABAQUS to be 1.024.
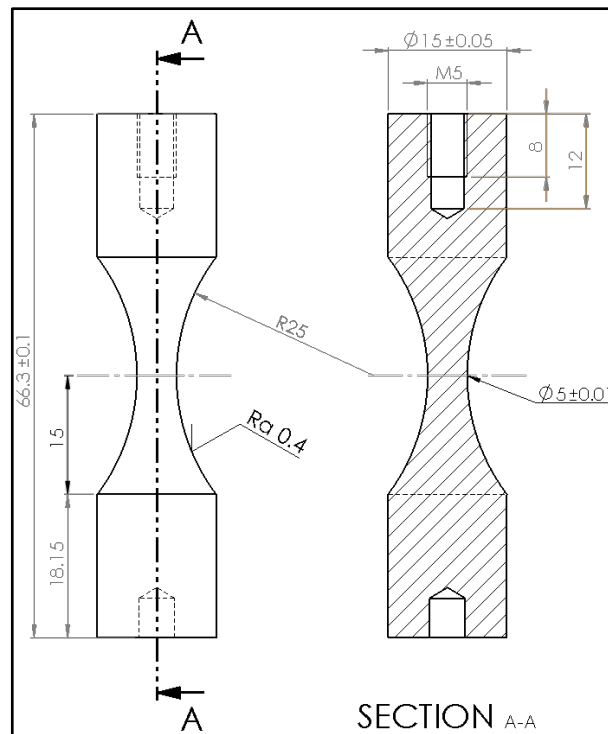
Figure 2.22 Specific Geometry of Specimen in the Test

Variable Section Booster & Sonotrode (3D)

The geometry of sonotrode is rod with constant section connected to variable cross section whose dimension can dramatically affect the amplification coefficient. In the case of continuous cone shaped sonotrode, it is impossible to determine the resonance length through calculation. This problem had been resolved using the finite element method (FEM).

The finite element equation shows as following (2.37):

$$[M]\{\ddot{u}\} + [C]\{\dot{u}\} + [K]\{u\} = \{F\} \tag{2.37}$$
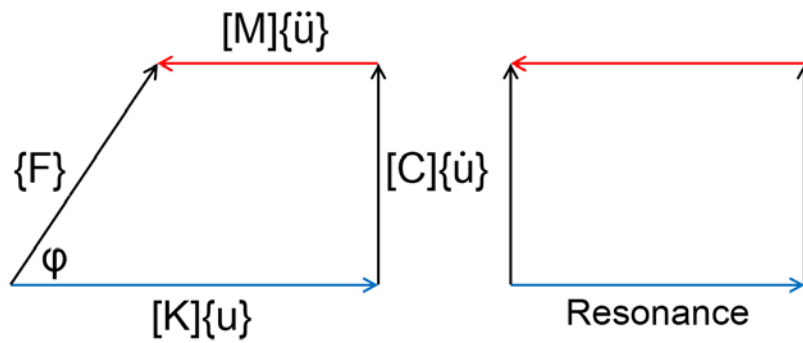
Figure 2.23 Force Polygon of vibration

Under the resonance condition shows in Figure 2.23 and Equation (2.38):

$$[M]\{\ddot{u}\} + [K]\{u\} = \{0\} \tag{2.38}$$

For the harmonic stationary wave during the fatigue test, it can be written as:

$$u(x,t) = u(x)e^{i\omega t} \tag{2.39}$$

Then (2.38) can be simplified as (2.40):

$$\omega^2 [M]\{u\} = [K]\{u\} \tag{2.40}$$

where [*M*] is mass matrix and [*K*] is rigidity matrix.
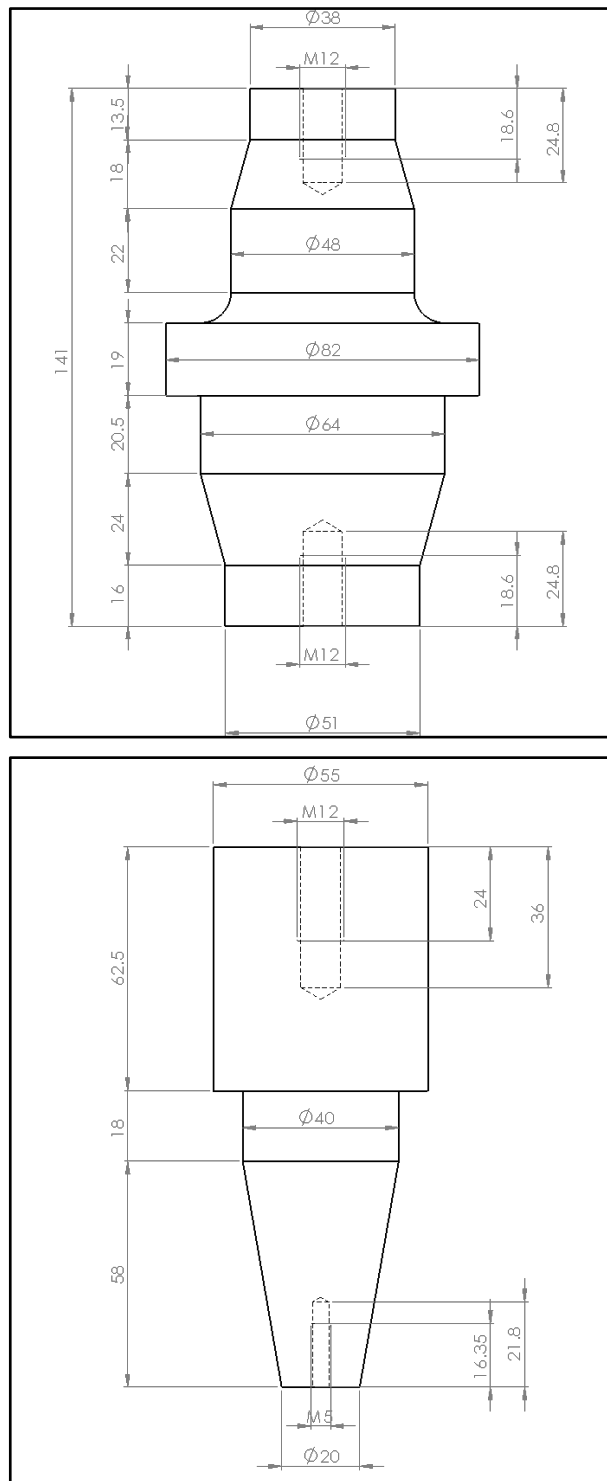
Figure 2.24 Specific Geometry of Booster and Horn (Sonotrode)

2.4.2 Numerical Simulation

Numerical simulation using the finite element method FEM software ANSYS is also employed for validation the resonance frequency of all the group and stress amplitude coefficient of the specimen. The model could be simplified into two dimension because the geometry of all the parts is axisymmetric. At the same time, this result is compared with that obtained from three dimension.

2D simulation is carried by classical APDL with Quad 8 Plane 183 element. Y axis of the global Cartesian must be chosen as the symmetry axis, and the radial line is only draw in the positive +X quadrant.

3D simulation is created by Workbench with Brick 20 Solid 186 element. The three dimension result is closer to the practice situation, avoiding to set additional constraint, shown in Figure 2.25.
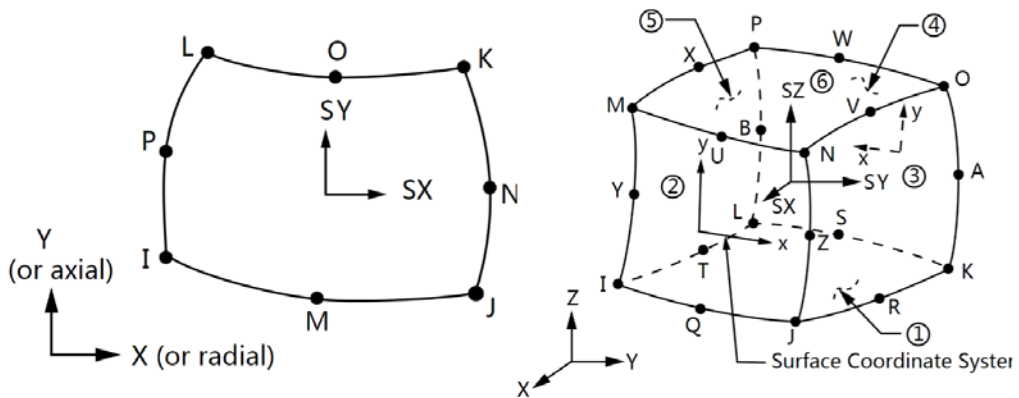
Figure 2.25 Plane 183 and Solid 186 Element
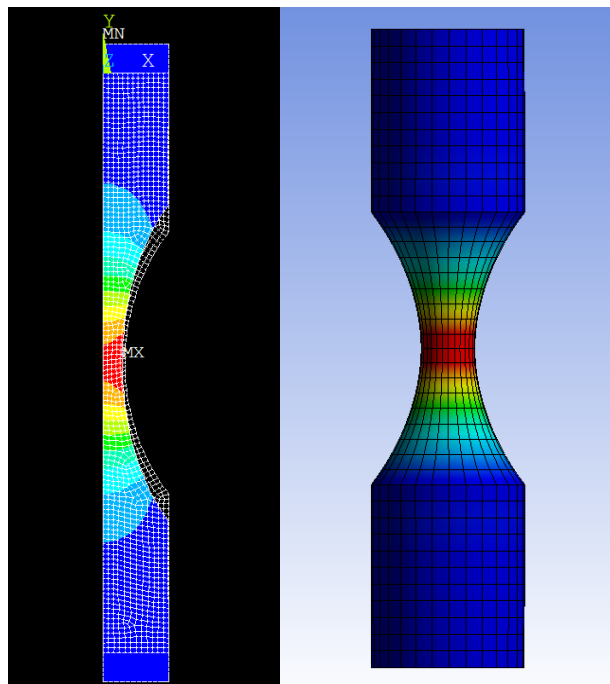
Figure 2.26 2D APDL Model and 3D Workbench Model of Specimen

77

Modal and Harmonic analysis are carried out for all the separated part (Booster / Sonotrode / Cylinder / Specimen) and two kind of assembly (without / with specimen), shown in Figure 2.27. Excited frequency is not been set by user, but chosen automatically by the Branson UPS software, according to the minimum total energy consuming, as well as minimum current. It means that specimen is not always vibrating naturally, but under forced vibration at the frequency suitable for all the groups.
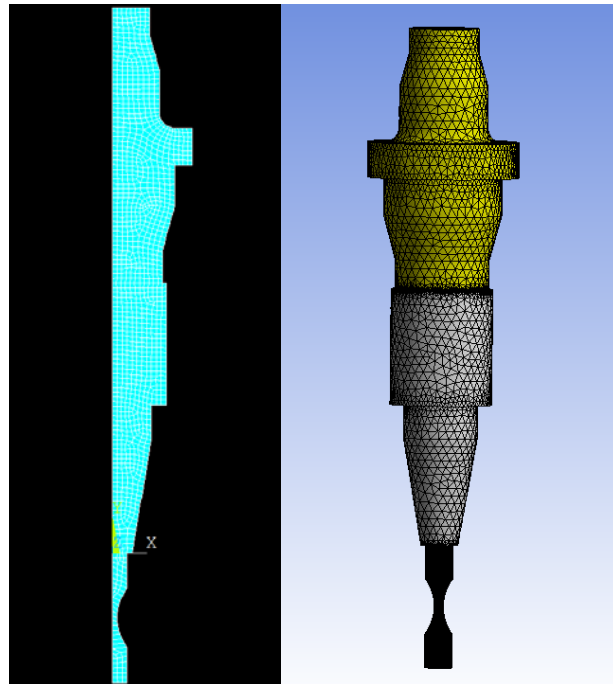
Figure 2.27 Assembly 3 Model with Specimen

The simulation result for separated part is shown in Table 2.1. There is no experimental data in this table, because it is difficult to measure the nature frequency of each part separately. All the frequency and coefficient in this table is under first tension compression mode. The difference between APDL 2D and Workbench 3D is in 20 Hz.

The assembly simulation result shows in Table 2.2, and compared with experimental data from software Branson UPS. It is clear that the frequency obtained from Assembly 3 (with specimen) and Assembly 2 (without specimen) shows obvious difference (≈100 Hz). The influence of hourglass specimen on the system cannot been ignored, even if the mass of specimen only occupies nearly 2% of all the system.

Table 2.1 Separated Part Simulation

	Material	m (g)	V (cm³)	ρ (kg/m³)	E (GPa)	ν (-)	Cs (MPa/μm)		f (Hz)	
							2D	3D	2D	3D
Booster	Aluminum	981.9	355.4	2762.6	70	0.32	/	/	19937	19938
Sonotrode	Ti6V	939.8	210.3	4469.1	111	0.30	/	/	19955	19976
Cylinder	Inconel 718	329.5	40.21	8194.5	206.9	0.294	5.080	5.078	19619	19612
Specimen	Inconel 718	64.32	7.852	8191.6	206.9	0.294	24.50	24.34	19461	19456

Table 2.2 Assembly Simulation

	Simulation Cs (MPa/μm)		Simulation f (Hz)		Experiment f (Hz)
	2D	3D	2D	3D	
Assembly 2 (without Specimen)	/	/	19957	19956	19942
Assembly 3 (with specimen)	23.735	23.415	19859	19860	19812

Self-heating

The self-heating of specimen is significant during the test, caused by the internal fiction under high strain rate. Temperature in the test section of specimen is higher than 100ºC, while lower relatively at two ends. Nature frequency decreased even several hundred Hz, due to the decreasing of modulus. Numerical simulation is carried for validation the resonance frequency and stress-amplitude coefficient of the specimen.

For simplify the calculation processing, specimen is treated as 7 slice in which with homogenous temperature distribution. The length of these slice is asymmetry to the test section, shown in Figure 2.28. Because the existing of cooling air between the booster and sonotrode, temperature at the top and bottom of the specimen is not totally asymmetry.
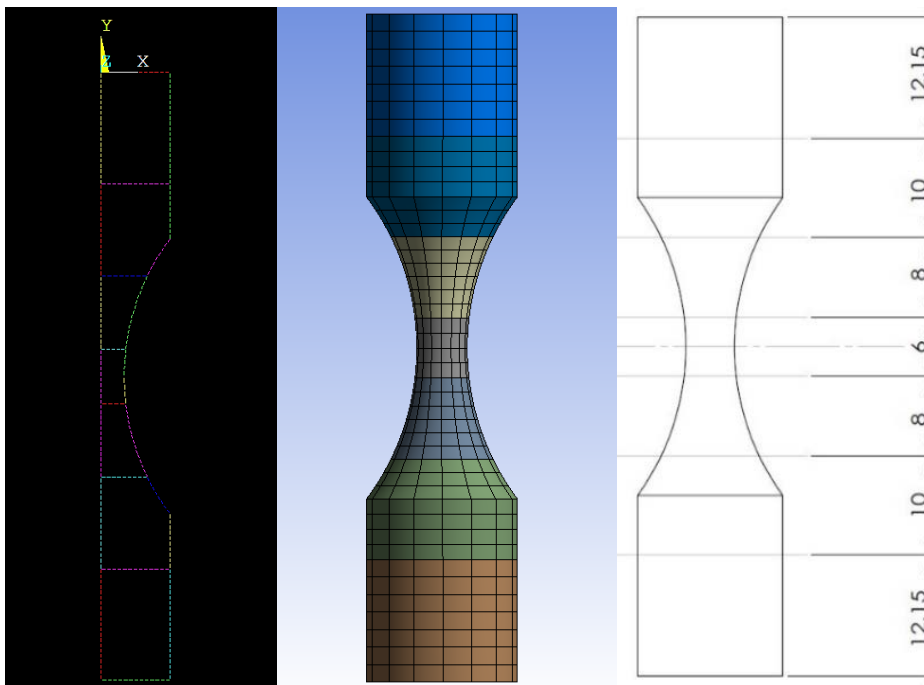
Figure 2.28 Sliced Model of Specimen with Self-heating

The simulation result for specimen with self-heating shown in Table 2.3. Temperature data comes from one of the experiment tests. It is clear that 115 ºC shows at the specimen bottom and only 67 ºC at specimen top which connected with sonotrode. 400 Hz decreasing appears after steady, while the applied stress in the test section changes not so much (<5%).

Table 2.3 Specimen Simulation with Self-heating

	T (ºC)	E (MPa)	ν (-)	Temperature Distribution		Cs (MPa/µm)	f (Hz)
RT	20	206892	0.294			24.34	19456
Beginning	21.4	206811.9	0.2939			23.76	19151
	21.8	206789.0	0.2939				
	81.1	203394.0	0.2892				
	251.7	193627.2	0.2772				
	80.0	203457.0	0.2893				
	22.5	206748.9	0.2938				
	20.2	206880.6	0.2940				
Development	41.8	205644.0	0.2923			23.11	18989
	84.9	203176.5	0.2890				
	163.3	198688.0	0.2828				
	271.6	192487.9	0.2762				
	165.1	198585.0	0.2827				
	92.4	202747.1	0.2884				
	57.7	204733.7	0.2911				
Steady	67.0	204201.3	0.2903			23.25	19029
	99.7	202329.2	0.2878				
	148.8	199518.2	0.2840				
	226.7	195058.4	0.2786				
	168.4	198396.1	0.2824				
	132.9	200428.5	0.2852				
	114.8	201464.7	0.2866				
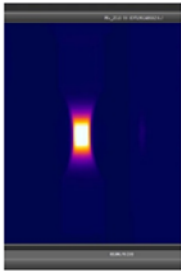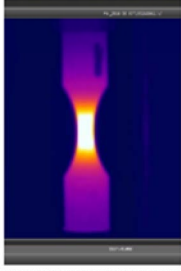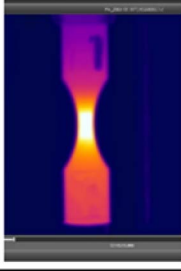
The assembly simulation result with self-heating shown in Table 2.4, compared with experimental data from VC++ control program (not Branson UPS).

It is necessary to point out that the minimum frequency of heated specimen happens during the beginning of the test, not until steady situation. Heat generates mainly from the middle of test section due to the high stress amplitude, and then transfers to the ends of the specimen. The processing of heat generation is faster than conduction, energy accumulates at this time. Maximum temperature of "Development" is 272° C, while after "Steady" is only 226° C. Therefore, the minimum of simulation frequency occurs also before steady.

However, the experiment frequency decreases continuously before steady. That is because that sonotrode is heated also during the experiment. This influence doesn't take into consideration when simulation.

Table 2.4 Assembly Simulation with Self-heating

	Simulation Specimen f (Hz)	Simulation Assembly f (Hz)	Experiment Assembly f (Hz)
RT	19456	19860	19812
Beginning	19151	19801	19754
Development	*18989	19771	19725
Steady	19029	19779	**19712

*   Minimum simulation frequency of only specimen

**   Minimum experiment frequency of assembly

Chapter III Material Properties

Before the ultrasonic fatigue test, physical properties, monotonic and cyclic behaviors of Inconel 718 are validated in this chapter. Micrograph of metallographic sample are taken using OM and SEM, for investigating the difference of grain size, phase, precipitate particle, etc. in detail.

3.1 Furnished Raw Material

Chemical Composition

Chemical composition of one specific material cannot be influenced by any heat treatment process. It should be point out before the section of heat treatment. However, there is slightly difference between different batches of this material. Therefore, the detail chemical composition is tested separately for the specific sample after treatment, listed in the Section 3.3.2.

Density

According to theoretical calculation and numerical simulation in last chapter, the most important material properties for resonance are density, Young's modulus and Poisson ratio. Mass and volume of the specimen keep constant after treatment, so that density is not influenced by heat treatment. Density of all the specimen is in this range:

$$\rho_{spe} = \frac{m}{V} = \frac{64.14 \sim 64.32 \times 10^{-3}}{7.852 \times 10^{-6}} = 8168.6 \sim 8191.5 \, kg \big/ m^3 \quad (3.1)$$

where m is the range of specimen mass which weighed from all the real specimens, and V is the theoretical volume which calculated by software.

Young's modulus, dynamic modulus and Poisson ratio under different frequency and temperature has shown in Section 3.4.

3.2 Heat Treatment

Density, Young's modulus and Poisson ratio changed slightly after heat treatment, while other parameters are influenced obviously, for example grain size, precipitate particle, yield strength, ultimate stress, etc.

Inconel 718 is typically purchased as annealed forging, billet, rod bar, plate and stress relieved condition. Then this material is fabricated in its most malleable condition. After fabrication, it could be heat treated as required per applicable specification.

Typical heat treatment of Inconel 718 from the handbook by Special Metal Corporation re given in Table 3.1 [102, 103]. All the data in bracket are original value directly from the manual (US System), and It is transformed into ISO standard for comparison, for example ºF to ºC, or ksi to MPa.

For most applications, Inconel alloy 718 is used under this form: solution annealed and precipitation hardened (aged). This alloy is hardened by the precipitation of secondary phases (e.g. γ' and γ'') into the metal matrix. The precipitation of these nickel- (aluminum/titanium, niobium) phases is induced by heat treating in the temperature range of 593 to 816ºC. For obtain this metallurgical reaction to properly take place, aging constituents must be in solution (dissolved in the matrix).

Anneal with its corresponding aging treatment is the optimum heat treatment where combining the rupture life, rupture ductility, impact strength, etc. because it produces the best transverse ductility in heavy sections, and the lowest temperature notch tensile strength. However, this treatment has tendency to produce notch brittleness in stress rupture.

It is said in the official handbook that "If fatigue strength is of prime importance, Inconel alloy 718 forgings can be used in the annealed rather than the annealed and aged condition; aging raises fatigue strength only slightly"[102, 103]. While, it is contrary with our VHCF result shown in the Section 4.3.

84

Table 3.1 Typical Heat Treatment of Inconel 718 by Special Metal Corporation

	Solution (Annealed)	Rapid Cooling	Precipitation Hardening (Aged)	Furnace Cooling	Slow Cooling	Hardness (HRC)	$\sigma_{y/0.2}$ (MPa)	σ_s (MPa)	δ/A (%)	ψ/Z (%)
Typically	927~1010ºC (1700~1850ºF)	Water	718ºC 8h (1325ºF)	621ºC 18h Total (1150ºF)	Air	36	1034 (150 ksi)	1241 (180 ksi)	10~12	12~15
	1038~1066ºC (1900~1950ºF)	Water	760ºC 10h (1400ºF)	649ºC 20h Total (1200ºF)	Air	38	1034 (150 ksi)	1241 (180 ksi)	10~12	12~15
Hot-Finished	954ºC 1h (1750ºF)	/	/	/	Air	8~19 (B 90~97)	379~496 (55~72)	814~869 (118~126)	45~53	47~52
	1066ºC 1h (1950ºF)	/	/	/	Air	4~6 (B 85~87)	324~365 (47~53)	758~793 (110~115)	58~62	61~65
Hot-Finished +Aged	954ºC 1h (1750ºF)	/	718ºC 8h (1325ºF)	621ºC 18h Total (1150ºF)	Air	45~46	1138~1241 (165~180)	1324~1434 (192~208)	17~21	24~39
	1066ºC 1h (1950ºF)	/	760ºC 10h (1400ºF)	649ºC 20h Total (1200ºF)	Air	43~45	1048~1138 (152~165)	1296~1351 (188~196)	20~24	26~36
Directly Aged	/	/	718ºC 8h (1325ºF)	621ºC 18h Total (1150ºF)	Air	41~44	1186~1310 (172~190)	1420~1489 (206~216)	19~24	35~45

Directly Aged treatment is chosen for the VHCF fatigue test, due to its highest yield and ultimate strength. Treatment step shown are in Table 3.2.

Table 3.2 Directly Aged Process by LEME

Temperature (°C)	Time (hour)
720	8
-50 ºC/h	2
620	8
	Total: 18

DAHQ (Directly Aged High Quality) is special edition used for turbine disc. It is directly aged, but difficult to ensure the heat treatment history precisely, because of the high confidentiality of this treat process. Finally, 3 sets of specimens (As-received, Directly Aged, DAHQ) are used in the study of VHCF test.

Macro-hardness test determined its value by measuring the penetration depth under larger load compared to the penetration by smaller preload. Hardness Brinell (HB), Rockwell (HR), and Vickers (HV) are widely used. Rockwell C standard (HRC) is tested by 120º diamond sphero-conical indenter with 150 kgf loading.

Micro-hardness has obtained by applied force less than 1000 gf with indentation smaller than 50 μm in general, using for specific phase or precipitation. Hardness Knoop micro (HK_m) and Vickers micro (HV_m) are most widely used. Micro Vickers is tested by 136º pyramidal diamond indenter.

For our study, macro and micro hardness of these 3 materials are determined, shown in Table 3.3.

Table 3.3 Hardness of Inconel 718 after Different Heat Treatments

	Tested (HRC)	Converted (HV)	Micro Hardness ($HV_m0.5/10$)
As-Received	19~24	234~260	257.2~313.0
Directly Aged	42~44	412~434	377.4~441.8
DAHQ	45~46	446~458	440.0~444.7

3.3 Microstructure after Aged Heat Treatment

Metallographic analysis of Inconel 718 is investigated before and after heat treatment. However, it should be noted that more than 90% of fatigue life in the very high cycle range is initiation life, which highly influenced by microstructure.

Through comparing the micrograph obtained from our samples with those from some fundamental literature which widely recognized and cited, the influence of microstructure after different heat treatment on the engineering properties and phenomenon can be investigated simply.

3.3.1 Phases of Inconel 718

TTT (Time Temperature Transformation) diagram of Inconel 718 is shown in the Figure 3.1. The DRX (Dynamic Recrystallization) temperature is about 950ºC, and grains begin to grow up over 1035ºC.

From the point of view of crystal phase, aged heat treatment at 720ºC until 8h could only influence the γ'' phase which cannot be observed by SEM. Analysis of micrograph can only focus on the structure, instead of focus on alloy phase.
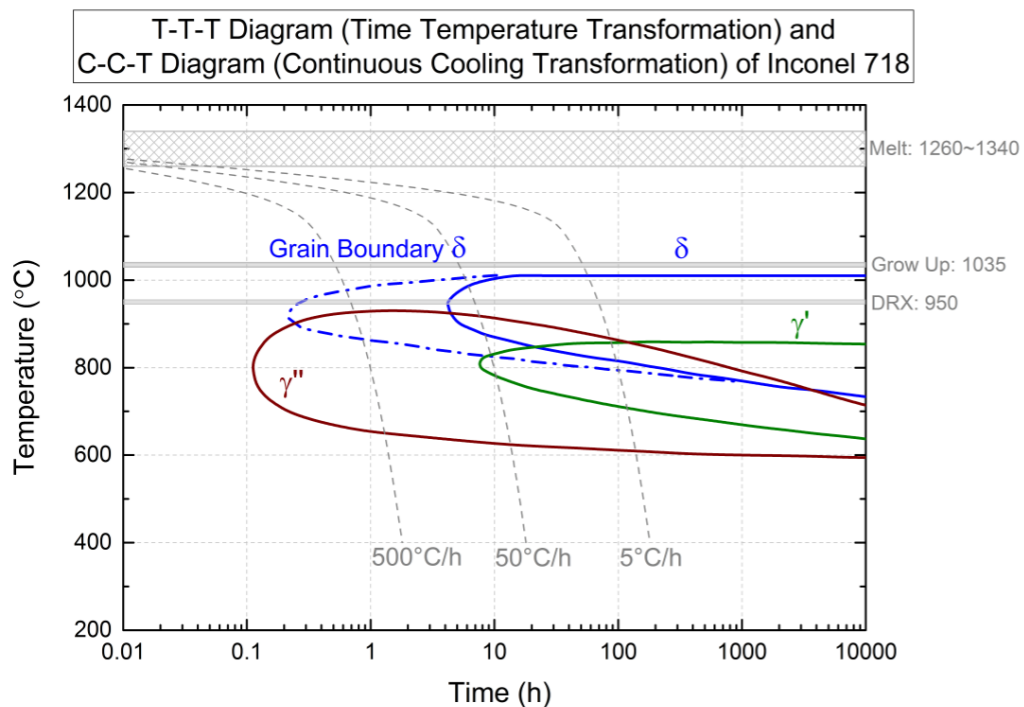
Figure 3.1 Precipitation Diagram of Different Phases of Inconel 718[125-127]

Phase γ, γ′ and γ″
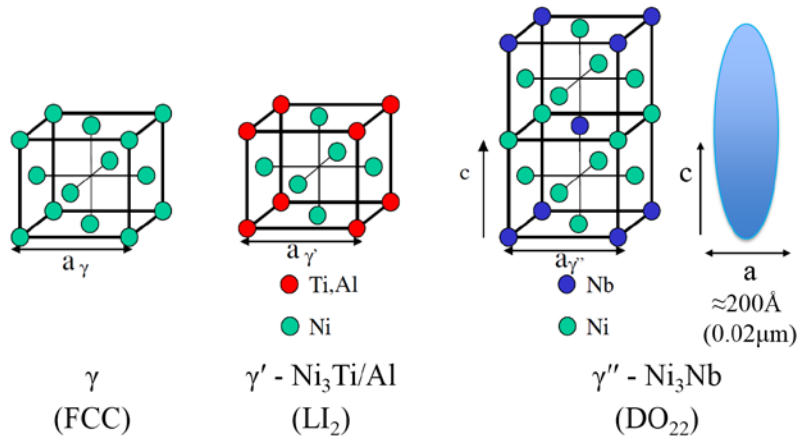
Figure 3.2 Phase γ, γ′ and γ″ Sketch in Inconel 718[128]

The strength of superalloy 718 comes from coherent solid state precipitates, which are small parts of γ′ (Ni_3Ti/Al), but mostly γ″ (Ni_3Nb), producing coherency strains in γ FCC matrix. The γ′ has unique morphology as round particle which can be smaller than 200Å, and γ″ is ellipsoid with length 5~6 times than its thickness. The resolution of SEM is not enough to observe them, need TEM[119, 120].

Phase δ

Non-strengthen orthorhombic phase δ (Ni_3Nb) is incoherent with γ matrix. Globularity / lenticular shaped δ distributes in the FCC matrix. Needle-wafer / lamellar shaped δ nucleates in grain boundary. It is used to control grain size in wrought material and seems to be also important for notch ductility[125].
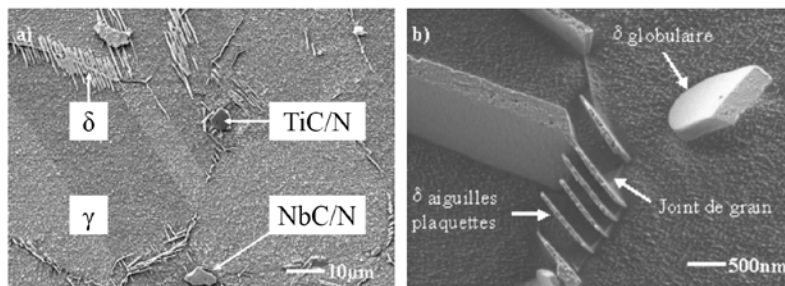
Figure 3.3 Phase γ and Precipitate Particle in Inconel 718[129, 130]

Carbides and nitrides are also important for superalloy, which provide some degree of matrix strengthen for achieving optimal strength properties, and for grain size control.

3.3.2 Characterization Technique

Etching

Metallographic sample is sliced by Al_2O_3 cut-off blade using very low feed speed 0.01 mm/s. Then it is polished by SiC emery paper from 80 to 2000 grit, and by 1/4 μm diamond paste for 30 minutes. All these steps are realized under water cooling to avoid temperature arising.

Sample is etched by Kalling's II (also called as Waterless Kalling) reagent in less than 30 minutes after polishing, avoiding the passive of smooth surface. Kalling's II is widely used for Nickel or Ni-Cu based superalloy. Immersing or swabbing several second up to minute permits to reveal grain boundary.

Table 3.4 Composition of Kalling's II Reagent

Ingredient	Proportion
37% HCl	100 ml
99% C_2H_5OH	100 ml
$CuCl_2$	5 g

SEM

Leica® DM ILM inverted light microscope with Baumer® TXG50c progressive scan camera (OM) and Jeol® JSM-6010Plus/LA scanning electron microscope (SEM) are chosen together to investigate the microstructure (phase, grain size, precipitate particle, etc.) of Inconel 718 after different heat treatment.
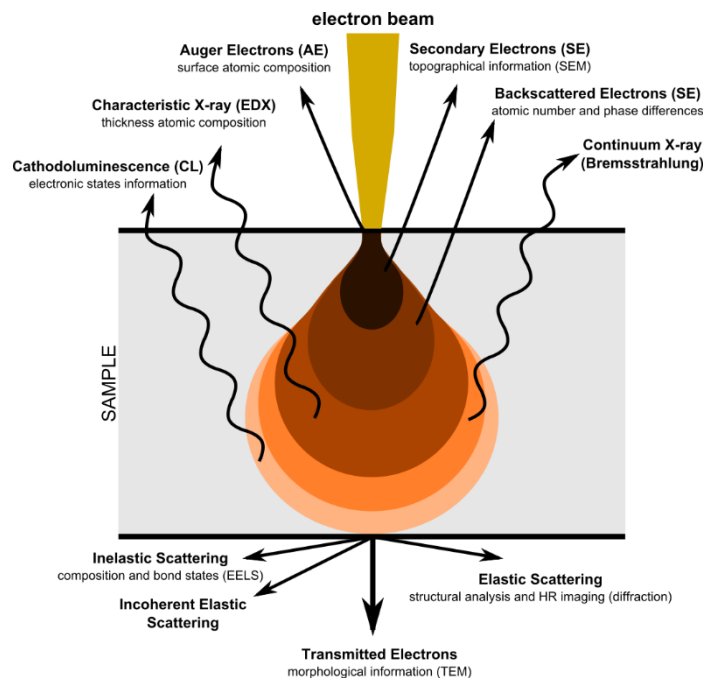
Figure 3.4 Electron Emitted from Different Interaction Volume

Electrons are emitted from tungsten (W) filament, and accelerated through high voltage of 50~100kV. The electron beam is focused by condenser lense to the spot between 5~10nm in diameter, with action depth ≈10 μm.

a) SEI

Secondary Electrons are used to create the surface topographical imaging. Only electron from the surface 5~10nm are emitted out of sample, due to its low energy less than 50 eV. Steep surface or edge shows brighter than flat surface, which resulted in image with well-defined 3D appearance.

b) BSE

Back Scattered Electrons are scattered from 50~100 nm with 10~20 keV, which produced the difference of atomic number imaging. The backscattered electron emission coefficient η is proportional to their Z atom number (Z<40). Higher atomic number zone appears brighter for smooth sample, while lower number atom shows darker.

BSE imaging is also influenced by surface geometry. There are two backscattered electron probes in our SEM, for distinguishing this kind of influence, shown in Figure 3.5. BEC Composition mode come from superposition of these two signals, highlighting the element feature. While BET Topology mode emphasizes geometry feature, close to SEI mode, is less widely used than BEC.

Comparison between SEI, BEC and BET imaging of as-received Inconel 718 are shown together in the Section 3.3.3.
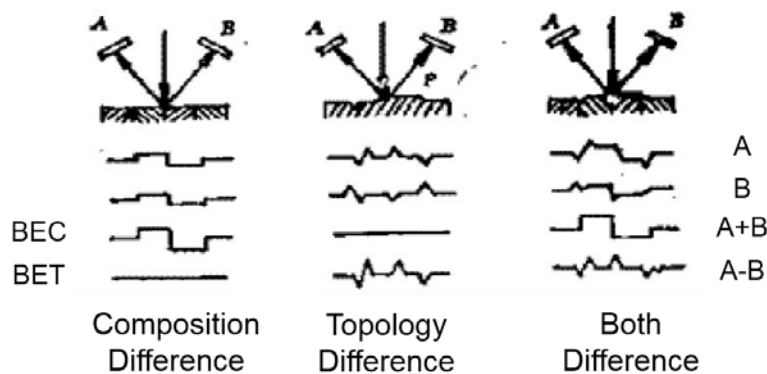
Figure 3.5 Working Principle of 2 Back-Scatter Electron Probes

c) EDS / EDX

Energy Dispersive X-Ray Spectroscopy is also used for chemical analysis. Characteristic X-rays are the critical information for element analysis. When incident electron strikes an electron out from the inner shell of the atom, it makes an electron hole. Another electron from outer shell fills up this hole, and then additional energy released by characteristic X-rays with specific energy generally between 1~15 keV.

On the opposite, continuum X-rays are emitted when primary electrons are decelerated by the strong electric field existing close to atomic nucleus. The energy of continuum X-rays comes from the kinetic energy lost during the deceleration. It has been observed as EDS spectrum background.
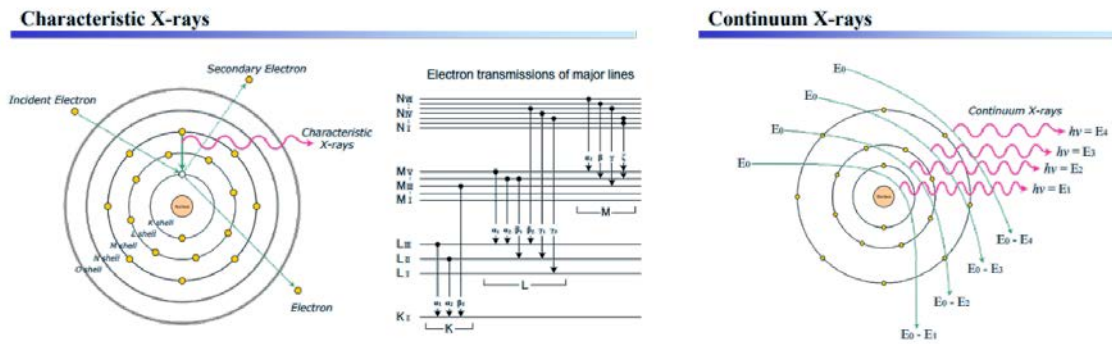
Figure 3.6 Characteristic and Continuum X-Ray Analysis

Table 3.5 Atomic Number and Characteristic X-Ray Energy of Main Elements in 718

Element	C	N	O		Al	Ti
Number	5	6	7		13	22
Kα (keV)	0.277	0.392	0.525		1.486	4.508

Element	Cr	Fe	Co	Ni	Nb	Mo
Number	24	26	27	28	41	42
Kα (keV)	5.411	6.398	6.924	7.471	16.581	17.441
Lα (keV)	0.452	0.705	0.776	0.851	2.166	2.293

Atomic number and characteristic X-ray energy of the main element in the Inconel 718 are shown in Table 3.5. For BEC imaging, automatic setting of brightness and contrast is based on the high weight limit elements (Ni, Cr, Fe), so that darker point indicates an area rich in C/N/Al/Ti, and lighter point is an area rich in Nb/Mo.

For EDS curve, Carbon, Nitrogen or Oxygen are difficult to be detected in some situation, due to their low characteristic X-ray energy (<1keV), comparing to the other elements.

EDS analysis imaging of Inconel 718 base matrix are shown in Figure 3.7. The measured zone combines with γ, γ', γ'' phases, without precipitation particles. The chemical composition is representative of all the 3 sets of materials (As-received, Directly Aged, DAHQ).

3 peaks for element Ni appear in this figure, at L_α=0.851 keV, K_α=7.471 keV, and K_β=K_α+L_α=8.322 keV. Same situation occurs for Cr and Fe. On the opposite, only 1 peak for element Al can be seen, and C/N/O cannot be detected.
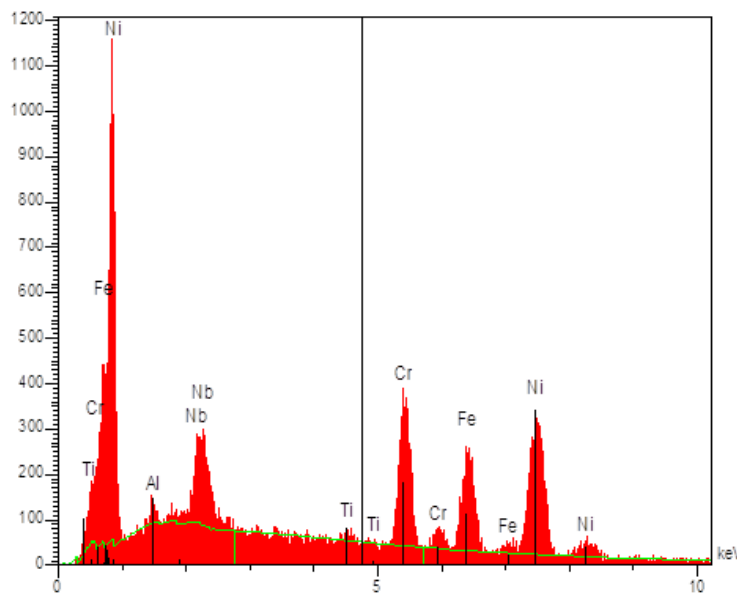
Figure 3.7 EDS Analysis of Inconel 718 Base Matrix (ONERA)

Chemical composition obtained by EDS for As-Received (AR), Directly Aged (DA), Directly Aged High Quality (DAHQ) samples are shown in Table 3.6. Element niobium, titanium, aluminum are concentrated into precipitation particles, leading to lower value than those from literature[102, 103].

Table 3.6 Limiting Chemical Composition (Mass %)

Element	Ni	Cr	Fe	Nb	Mo	Ti	Al
Manual	50~55	17~21	13~25	4.75~5.5	2.8~3.3	0.65~1.2	0.2~0.8
AR	51.14	19.56	20.15	4.91	2.59	1.14	0.51
DA	51.06	19.69	20.41	4.64	2.45	1.15	0.60
DAHQ	51.90	19.40	19.74	4.66	2.62	1.12	0.56

3.3.3 As-Received

Optic micrograph of as-received Inconel 718 metallographic sample is shown in Figure 3.8. The most obvious and important feature in this material is heterogeneous. It contains several "fine grain bands" (b) and lots of "non-recrystal" larger grains (c/d). Each band consists of large amount of fine grains up to hundreds, while the total length of these grains is still smaller than only one non-recrystal grain (>100μm). In another words, the length of the largest grain is more than 100 times than the smallest. This level of heterogeneity leads severe damage on the mechanical properties, especially for high frequency fatigue.

Except for these two kinds of abnormal grain, size of other grains remains in the range of 10~40μm (a). And the size of the precipitate particle is nearly 10μm, close to the base γ grain (f).
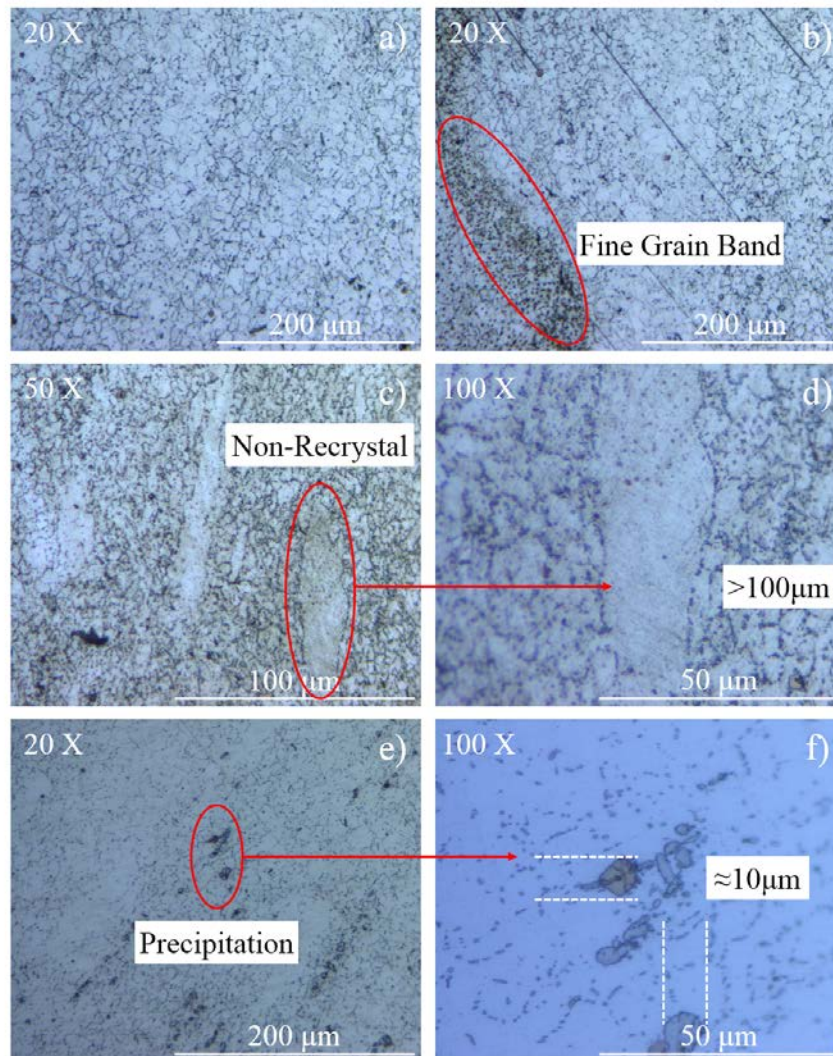
Figure 3.8 OM Imaging of As-Received Inconel 718
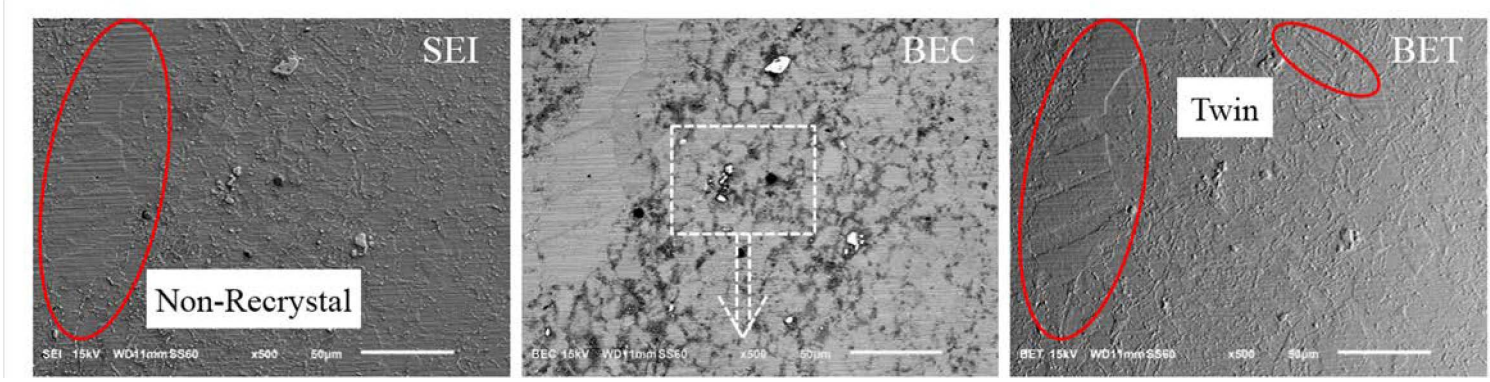
Figure 3.9 SEM Imaging of As-Received Inconel 718 (3 Modes of the Same Zone)
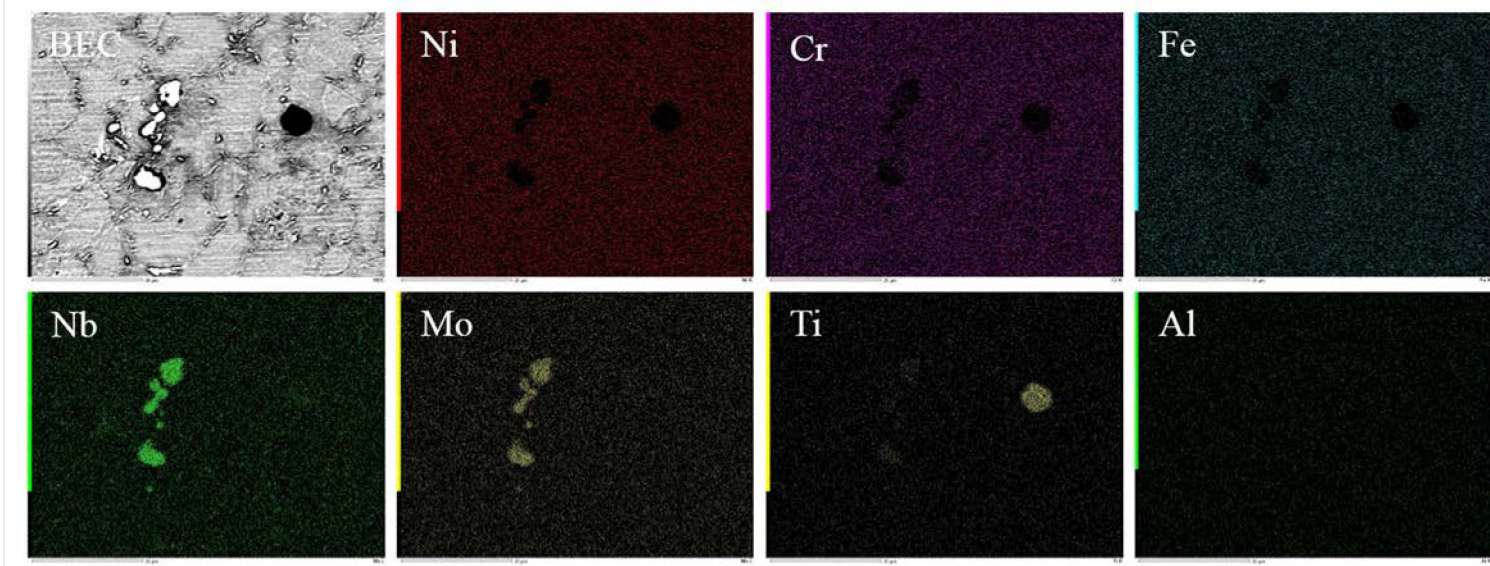
Figure 3.10 EDS Map Imaging of As-Received Inconel 718

Scanning electron micrograph of as-received Inconel 718 metallographic sample is shown in Figure 3.9. Under BET mode, it is clearly that large non-recrystal grain consists of several twins. The length of twin boundary is nearly 50μm. It seems to be the potential weakness initiation point for fatigue failure.

Energy dispersive X-ray spectroscopy (EDS) map of precipitate particles is shown in Figure 3.10. All of them are lack of elements Ni, Cr and Fe, which are the main elements of Inconel 718. Under BEC mode, the lighter particle is rich in Nb and Mo, and darker particle is rich in Ti and Al. (Al is not clear enough in this picture, but exists.)

According to the fundamental literature, these kind of precipitate particles could be carbides, nitrides or carbonitrides. However, C/N/O element is really difficult to detect with our present SEM, due to its low characteristic X-ray energy. (Detail data is in Table 3.5)

Micro-hardness test is applied on different kinds of grain or particle, for investigating the possible influence on fatigue strength, shown in Table 3.7. Only 25 grams force loading can be applied during the Vickers micro-hardness tests, because the indentation must keep inside the particle totally, in another words, it must keep smaller than 10μm. Hardness of "fine grain band" zone is slightly higher than non-recrystal, because the existence of the grain boundary. Precipitate particle is much harder than matrix, becoming another potential area of crack initiation.

Table 3.7 Micro Hardness of Different Phase in As-Received Inconel 718

	Non-Recrystal	Fine Grain Band	Dark Precipitation	Light Precipitation
$HV_m0.025/10$	268.8	319.2	523.5	>800
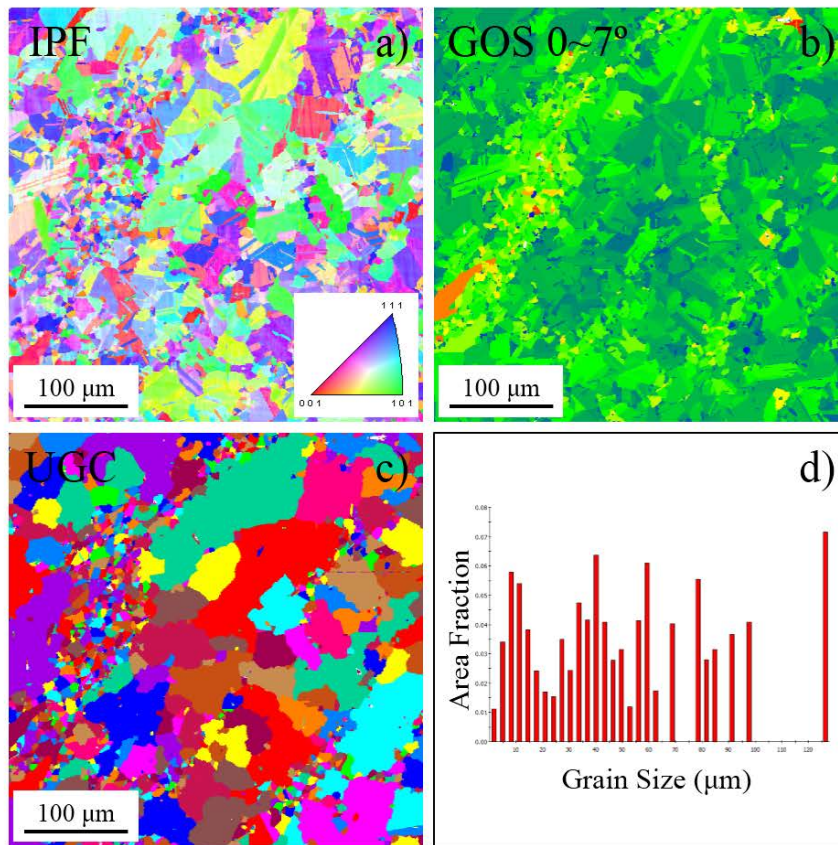
Figure 3.11 EBSD Imaging of As-Received Inconel 718

Inverse Pole Figure (IPF) micrograph of As-Received Inconel 718 is shown in Figure 3.11 (a). Plotting three Euler angles using an RGB color scheme is the best way of generating an orientation map, which is normally referred to Euler map. A different color scheme is used by the Inverse Pole Figure (IPF) color scheme, which can be interpreted easily and does not have considerable color changes with small orientation changes. It is clear that, there are long twin boundaries with length of nearly 100 μm in the non-recrystal grain.

Grain Orientation Spread (GOS) micrograph of As-Received Inconel 718 is shown in Figure 3.11 (b). The GOS is calculated as the average deviation of the orientation of each point in the grain from the average orientation for the grain. Most of grains with well-developed high angle grain boundaries are characterized by no internal structure and uniform orientation. Some of the grains do, however, possess internal orientation spread, but in those cases the GOS parameter value does not correspond to grain size. Several yellow and orange points appear in the "fine grain bands". It means that this kind of grain is not enough full developed, become the potentially dangerous point as crack initiation.

Unique Grain Colour (UGC) micrograph of As-received Inconel 718 is shown in Figure 3.11 (c). The UGC map is constructed by choosing distinct colors for each detected grain in order to visualize the grain boundary and subgrain etc.

Histograms of grain sizes is shown in Figure 3.11 (d). Horizontal axis is grain size, and vertical axis is the area fraction of these grains with same size. Obvious heterogeneity shows in this material sample. The grain sizes distribute in the range of 0~140 μm.

3.3.4 Directly Aged

OM micrograph of directly aged Inconel 718 metallographic sample is shown in Figure 3.12. "Fine grain band" disappears totally after aged treatment. "Non-recrystal grain" is also difficult to find in the vision of optic micrograph. It seems that there is light, unclear, discontinuous trace in some plate zones (c), which are similar to original non-recrystal grain. Maybe dynamic recrystallization happens in some special zones, even if temperature is not enough high.

Twin boundary is still found in the micrograph, while it is not in the large non-recrystal grain, and the length is less than 20μm.
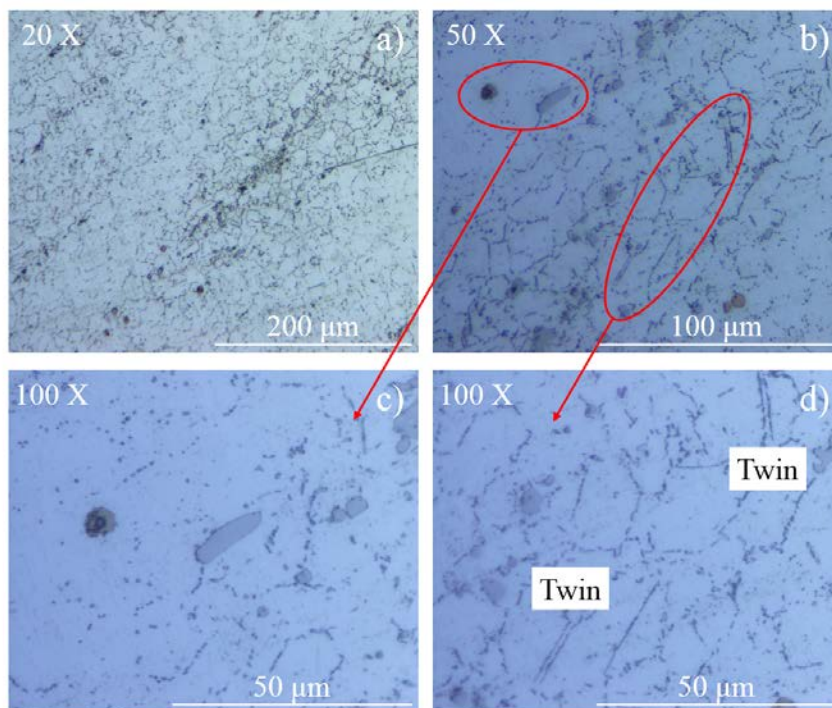
Figure 3.12 OM Imaging of Directly Aged Inconel 718

SEM micrograph of directly aged Inconel 718 metallographic sample is shown in Figure 3.13. Similar phenomenon can be observed from this imaging, "fine grain band" and "non-recrystal grain" disappear totally after aged treatment.

Grain boundary δ allows to identify the boundary between different grains, as well as the size of grains. The grain distributes in the range of 10~20μm after aged treatment, which is consistent with ASTM 8~10.
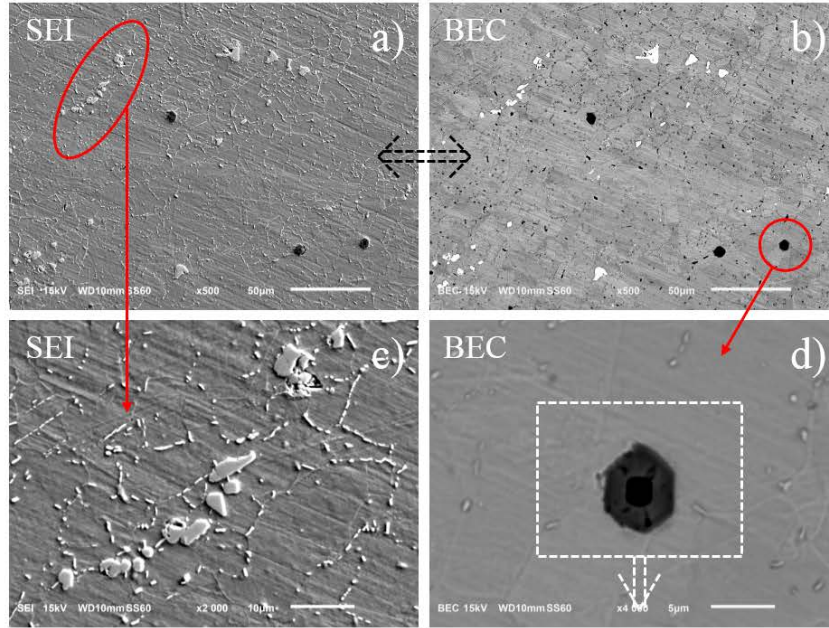
Figure 3.13 SEM Imaging of Directly Aged Inconel 718

EDS of the precipitate particles is shown in Figure 3.14. Comparing to the last imaging Figure 3.10, Al element is clear in the center of the dark particle.
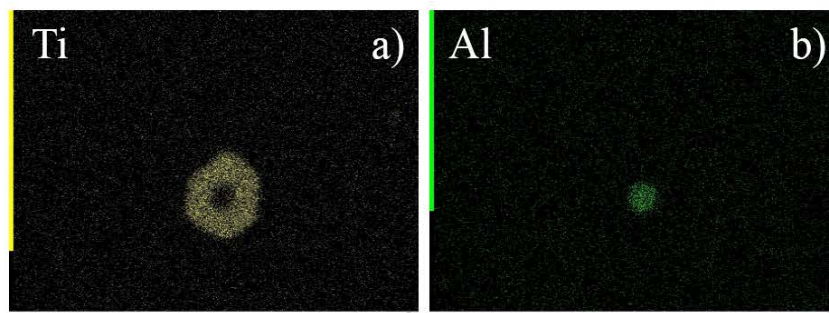
Figure 3.14 EDS Map Imaging of Directly Aged Inconel 718
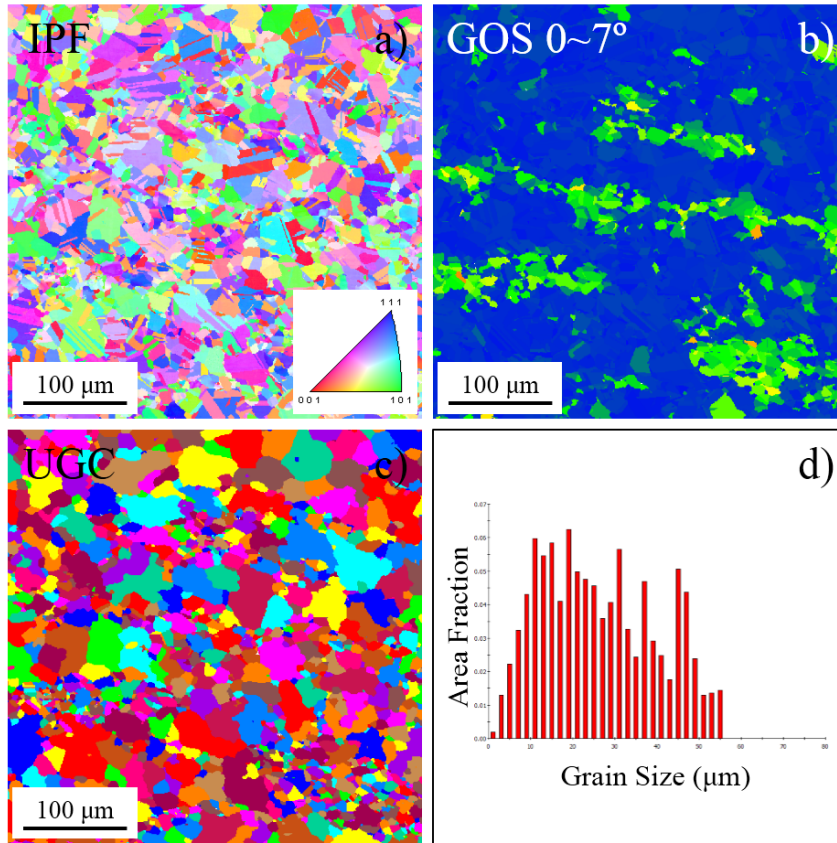
Figure 3.15 EBSD Imaging of Directly Aged Inconel 718

EBSD micrograph of Directly Aged Inconel 718 is shown in Figure 3.15. "Non-recrystal grain" disappears after long time aged heat treatment. Even if there is still some small grain in this sample (c), the size of them is concentered nearly 10 μm (d), instead of "fine grain band".

3.3.5 DAHQ (Directly Aged High Quality)

OM micrograph of DAHQ Inconel 718 metallographic sample is shown in Figure 3.16. Perfect homogeneity can be seen in this material. It is necessary to point out that δ phase not only exists in the grain boundary, but also diffuse in the based γ matrix in this edition of 718. It is not possible anymore to identify the grain size through this phase.

Another difference of this material is that, the size of dark precipitate particle is nearly 15μm, larger than previous edition 10μm, and ellipsoid shaped light precipitate appears, with length of about 25μm.
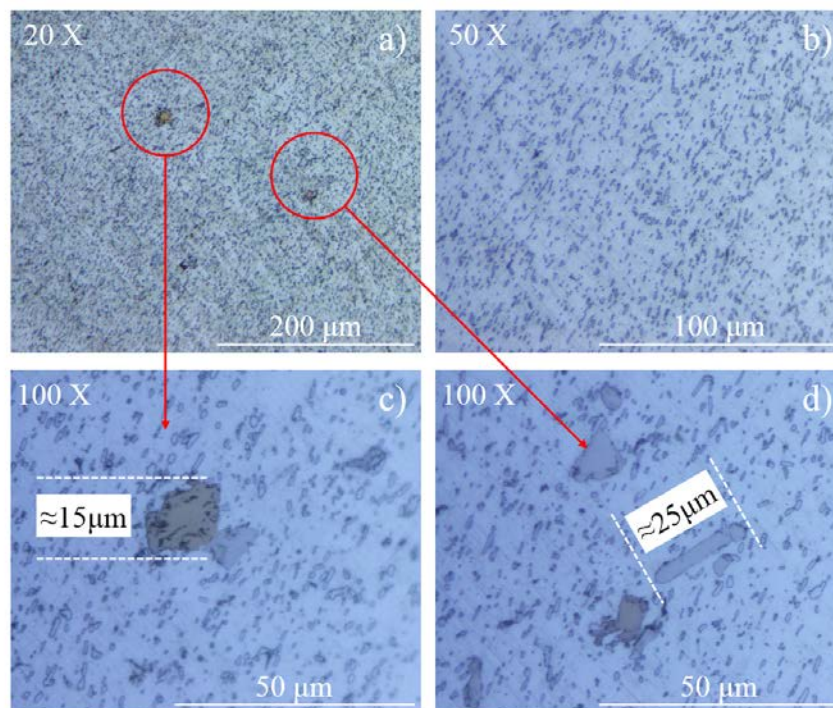
Figure 3.16 OM Imaging of DAHQ Inconel 718

SEM micrograph of DAHQ Inconel 718 metallographic sample is shown in Figure 3.17. Perfect homogeneity still exists under high magnification (c). From the back scatter imaging (part d), there is very subtle difference between different grains. It seems that the grain orientation will influence the backscattered electron emission coefficient. Grain size can be identified through this kind of colour difference. The grain distributes in the range of 6~10μm after aged treatment, which is consistent with ASTM 10~12.
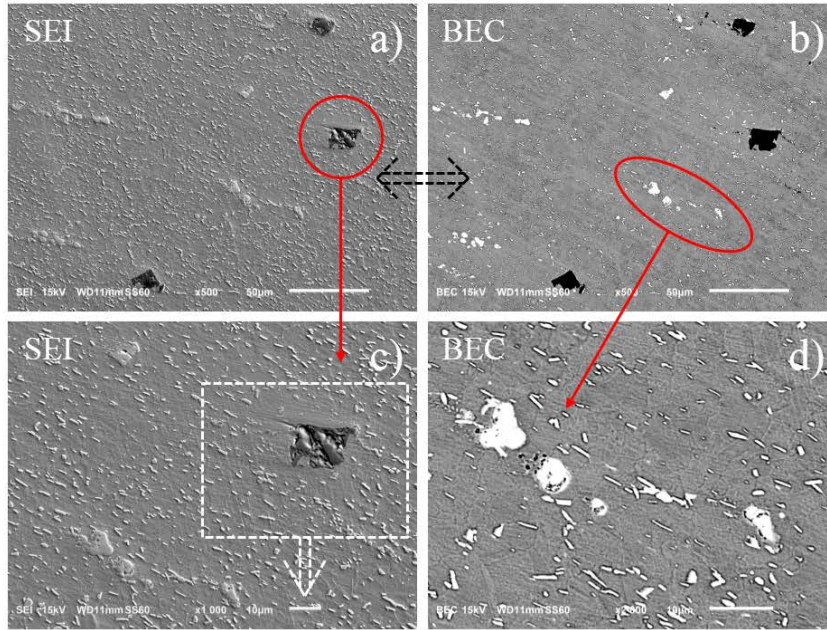
Figure 3.17 SEM Imaging of DAHQ Inconel 718

EDS of precipitate particles is shown in Figure 3.18. Comparing to the last image, Nb element is also rich in the dark particle.
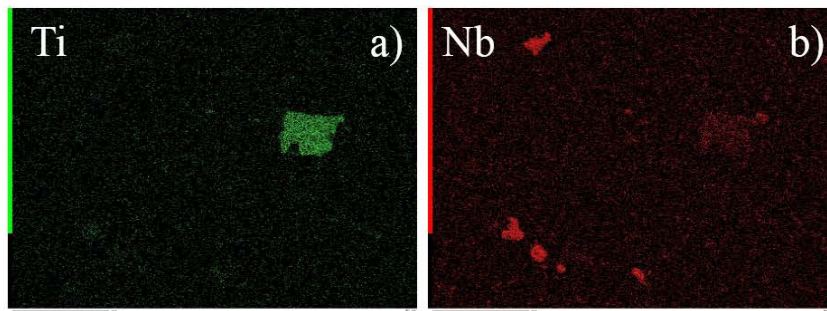
Figure 3.18 EDS Map Imaging of DAHQ Inconel 718

EBSD micrograph of DAHQ Inconel 718 is shown in Figure 3.19. Perfect homogeneity appears in this sample. Majority of grains distribute in the range of 6~10 um. The black points seem to be δ phase. It exists not only in the grain boundary, but also diffuse in the based γ matrix.

The proportion and size of δ phase could be an important influence factor of fatigue behavior[122, 131]. But it is not validated in this project, maybe in the future.
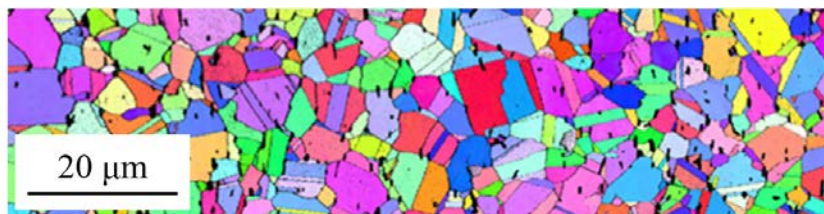
Figure 3.19 EBSD Imaging of DAHQ Inconel 718

102

3.4 Macroscopic Property of Inconel 718

MTS® Landmark™ 793 servo-hydraulic test system with 647 hydraulic wedge grips is chosen to investigate the mechanic properties of these 3 Inconel 718 (As-received, Directly Aged, DAHQ). At the same time, MTS® 634.31F extensometer with reference working length 10_{-2}^{+4} mm is positioned on the straight section of the specimen. It is clamped by metal spring for the strain monitoring.

Specimen has been originally designed for an old tensile machine with mechanical grip, in Figure 3.20 The shrink in the holding section becomes useless with new hydraulic wedge grip after precise calibration of centrality by MTS.

For cyclic response combined with tension and compression (R=-1), the shape of test section is determined as uniform cylinder, instead of plate. Diameter of the cylindrical section is 6mm, while length is only 12mm, to avoid bending during the compression processing, in Figure 3.20.

Compared with the standard tensile specimen with longer test section (A5, A20, A50...), the measured elongation using our shorter specimen seems to be larger and the area reduction seems to be slightly smaller. The shape influence on the yield strength, ultimate strength and elastic modulus could be ignored. For the shape of standard tensile specimen, ASTM E8-16a can be used as reference. (Standard Test Methods for Tension Testing of Metallic Materials)
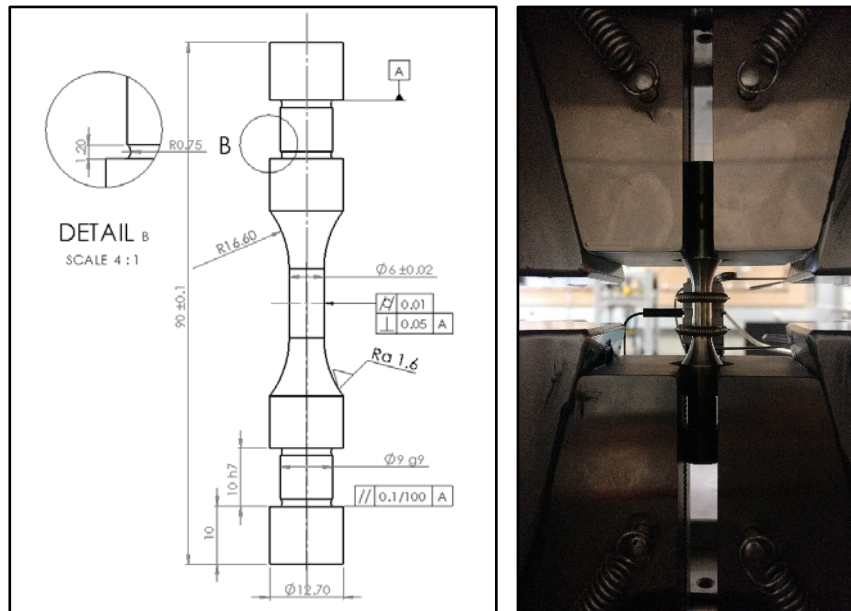
Figure 3.20 Geometry of Cylindrical Specimen and Extensometer

3.4.1 Quasi-Static Uniaxial Tensile

Quasi-static uniaxial tensile test under displacement control with loading speed of 0.05mm/min is carried out at room temperature. The stress-strain relation obtained during this test is shown in Figure 3.21. It is obvious that yield stress after aged treatment is nearly 1200 MPa, becoming more than twice 550 MPa of As-receive material. Same situation also happens on ultimate strength.

However, ductility becomes worse after heat treatment. Total strain at rupture of directly aged specimen is only 30%, while more than 55% is reached for As-received one. (The positive maximum limit of extensometer is 50%, the real strain should be more than 55%, according to the displacement tendency of grips.)

Considering hardness data given in the last section, As-received edition Inconel 718 combines low hardness, low yield strength (relatively) and high ductility. That is why commercial material billet, bar or plate is always sold in the original condition without any treatment.

The slope of linear rising part call as elastic modulus, it seems keeps nearly constant, independent from heat treatment.
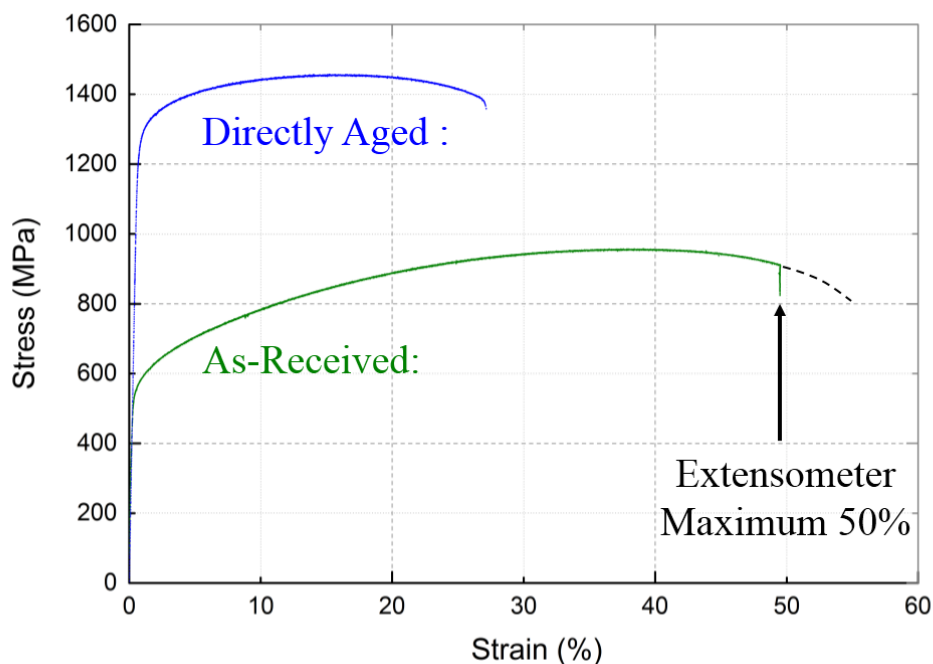
Figure 3.21 Quasi-Static Stress-Strain Curve of Inconel 718

Mechanical properties data are shown in Table 3.8. Another data from manual of Special Metal Corporation® are added in the bracket for fast comparison[102, 103]. It can be noticed that good agreement between these values.

Table 3.8 Mechanical properties after Different Heat Treatment

	E (GPa)	$\sigma_{0.2}$ (MPa)	σ_{UTS} (MPa)	δ/A (%)	ψ/Z (%)
As-Received	190.62	≈538.5 (324~496)	956.71 (758~869)	58.33 (45~62)	48.64 (47~65)
Directly Aged	201.46	≈1249.3 (1186~1310)	1456.65 (1420~1489)	29.17 (19~24)	27.75 (35~45)
DAHQ	Confidential	?	?	?	?

Fracture of uniaxial tensile specimen is shown in the Figure 3.22. The test section length of As-received specimen becomes much longer than before loading, and obvious necking happens at the center. The area of test section of directly aged specimen decreases uniformly, there is no necking at the center. It also means this material becomes more brittle than before heat treatment.
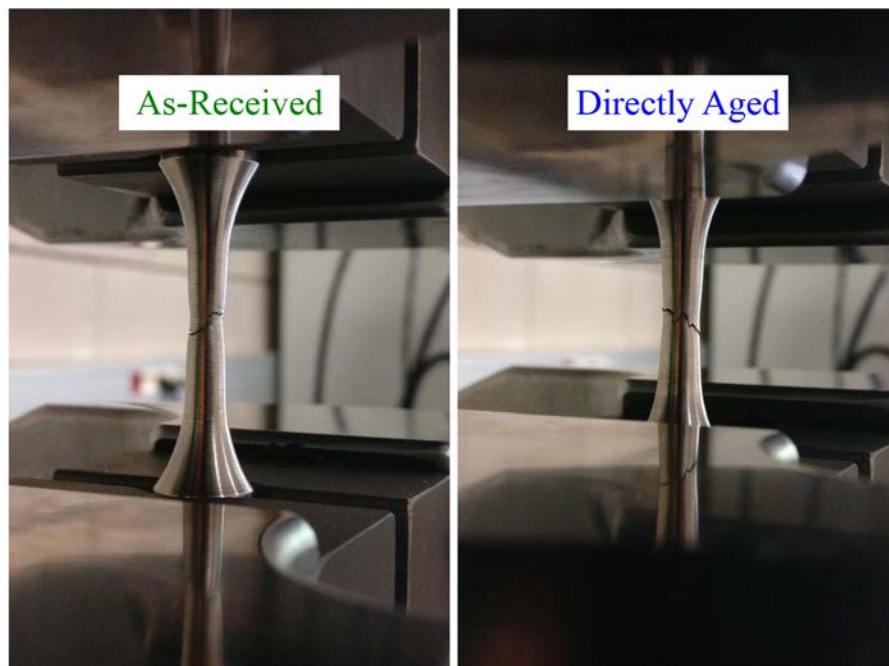
Figure 3.22 Fracture of Uniaxial Tensile Test of Inconel 718

3.4.2 Cyclic Stress-Strain Response

Full reversed tension-compression test under force/stress control (R_σ=-1) at 0.1Hz is carried out at room temperature. Usually, it is better to use strain control in this kind of test, while for avoiding the possible unstable during the past test, stress control is used in the test. At least 3 level of loading are chosen, totally elastic, slightly plastic and significantly plastic. The real specific value determines depend on the uniaxial tensile data in Section 3.4.1.

Cyclic response of As-received Inconel 718 is shown in Figure 3.23. Totally elastic behaviour happens until 300 MPa, slightly plastic begins to appear when loading reaches 400MPa.
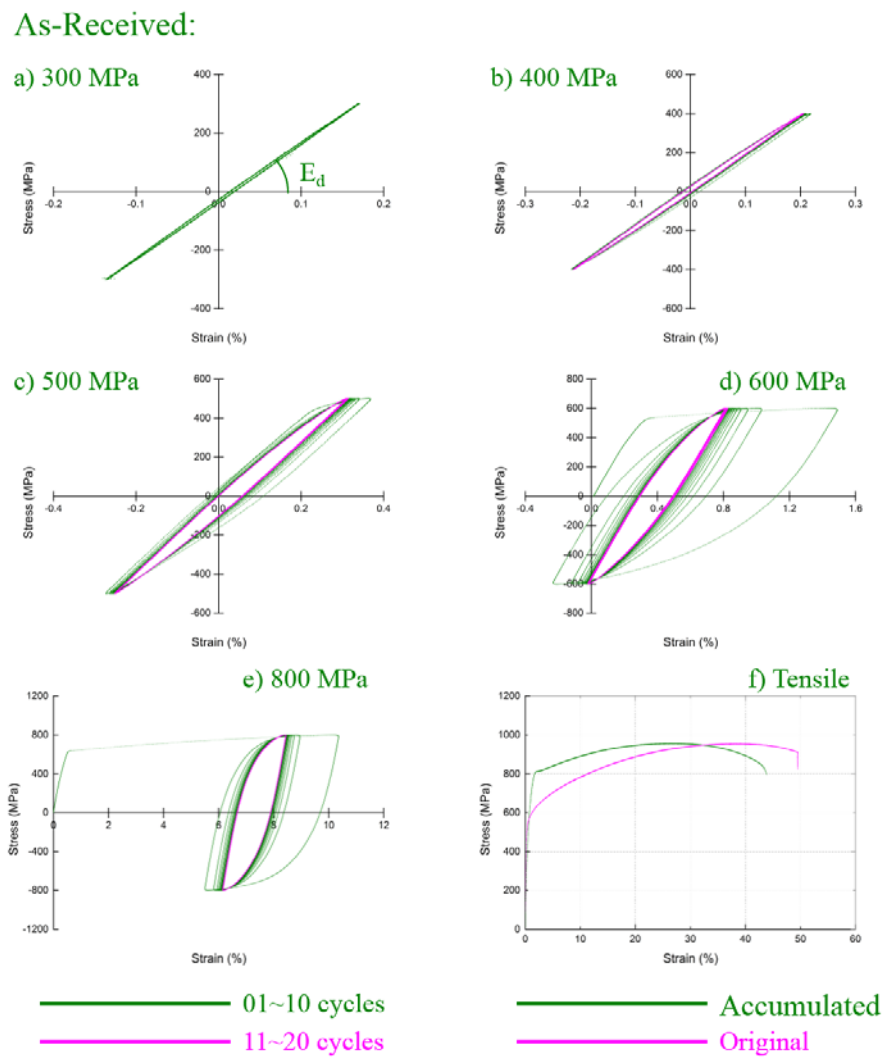
Figure 3.23 Hysteresis Loop of As-received Inconel 718

Hysteresis loop develops from wide to narrow (relatively). It means cyclic harden exists for the as-received material. And loop achieves and keep nearly constant after nearly 10 cycles, (highlighted by bright colour). Cyclic hardening phenomenon exists also in ultrasonic self-heating test, in Section 4.1.

After this significantly plastic test, an additional tensile test is applied until failure, in Figure 3.23 (f). The rising part of this curve is linear up to 800MPa, it seems follow the history of last cyclic test of 800 MPa, and then reaches the same ultimate stress with new specimen.

Cyclic response of Directly Aged Inconel 718 is shown in Figure 3.24. It keeps totally elastic up to 1000 MPa, and turns into plastic when loading over 1200MPa. Hysteresis loop develops from narrow to wide. It means slightly cyclic soften exists for the directly aged material. It reaches constant after 20 cycles at 1200 MPa, while keep diverging at 1300 MPa until break. Slightly cyclic softening exists also in the ultrasonic self-heating test, as shown in Section 4.1.
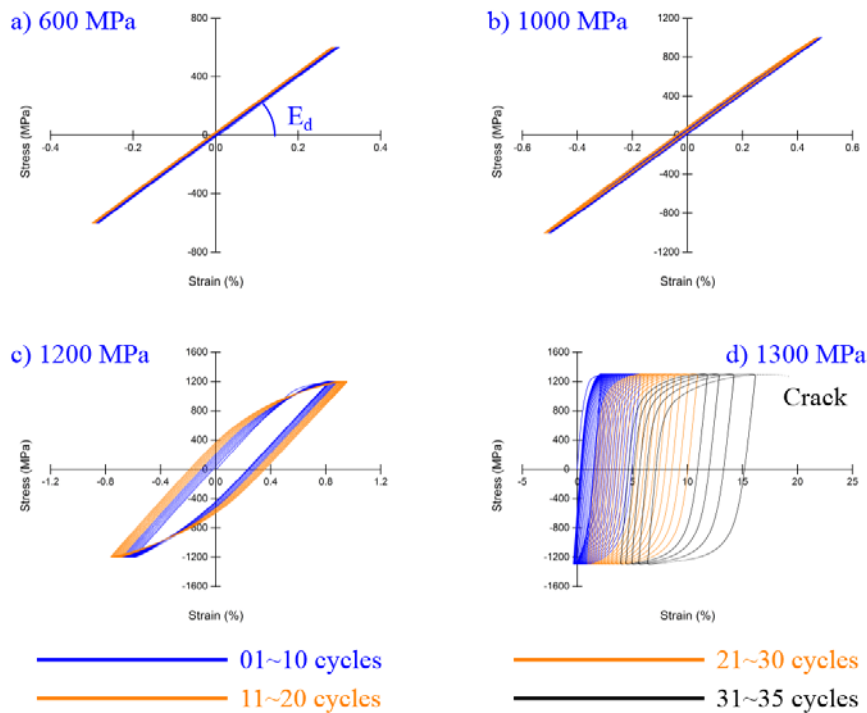
Figure 3.24 Hysteresis Loop of Directly Aged Inconel 718

The slope between stress and strain cyclic relation of linear condition is known as "dynamic modulus". It will increase slightly as the test strain rate increase, this value has shown in the following section.

Dynamic Modulus

Uniform cylindrical bar with diameter 20mm is chosen to determine the dynamic modulus of As-received Inconel 718 at 20 kHz. Length of 128mm is determined in order to resonance with piezo-ceramic convertor. Simple geometry can be manufactured accurately. Low stress amplitude coefficient of uniform cylinder shape ensures low self-heating during the test. Air cooling is also applied on the specimen for making sure nearly RT during all the test. In summary, the dynamic modulus of this cylinder is:

$$\rho_{cyl} = \frac{m}{V} = \frac{m}{\pi r^2 l} = \frac{329.5 \times 10^{-3}}{\pi * \left(10 \times 10^{-3}\right)^2 * 0.128} = 8191.6 \, kg\big/m^3 \tag{3.2}$$

$$\begin{aligned} E_d &= 4l^2 f^2 \rho \\ &= 4 * 0.128^2 * \left(19648 \sim 19651\right)^2 * 8191.6 * 10^{-9} \\ &= 207.25 \sim 207.31 GPa \end{aligned} \tag{3.3}$$

It is necessary to point out that the frequency used here is the resonance frequency of all the group, because it is really difficult to measure the nature frequency of specimen separately. Bigger volume and heavier mass of this cylinder than VHCF specimen makes sure these two frequencies enough close.

Theoretically, deformation response could be delayed under high frequency loading, so that dynamic modulus should be little higher than static value in general. Experimental data obtained with this cylinder validates this tendency.

Table 3.9 Elastic Modulus under Different Loading Frequency

	E Static (GPa)	E_d 0.1Hz	E_d 20kHz
As-Received	190.62	200.67	207.28
Directly Aged	201.46	209.70	?
DAHQ	Confidential	?	?

High Temperature Modulus

Young's modulus and Poisson ratio change slightly after heat treatment, while they are influenced obviously by temperature, shown in Table 3.10. All these data come from experimental test in ONERA. It decreases 11% at 400ºC, compared to RT. Nature frequency of this specimen decreases several hundred of Hz, due to the decreasing of modulus. This phenomenon explains why the group stop only by self-heating of the specimen, without breaking of specimen.

Table 3.10 Elastic Modulus under Different Temperature

Temperature (°C)	Young's Modulus (GPa)	Poisson Ratio (-)
20	206.892	0.294
200	196.587	0.280
350	187.999	0.272
400	185.137	0.272

Chapter IV Ultrasonic Fatigue Results

Self-heating phenomenon of Inconel 718 with different heat treatment studies experimentally in this chapter. Dissipated energy is calculated and modeled after. S-N curve until ultra long life regime (10^{10} cycles) is carried out. The prediction of fatigue life shows at the end.

4.1 Self-heating Phenomenon

Ultrasonic fatigue loading is energy dissipated process, accompanying temperature variation on the specimen surface. It is important to present the self-heating phenomenon results before the VHCF characterization.

Self-heating test of Inconel 718 at 20 kHz and room temperature without cooling are carried out using the same hourglass specimen for fatigue test, shown in Figure 2.22.

Maximum temperature obtained from all the specimen surface under different loading levels is shown in Figure 4.1. It increases rapidly after test start, and approaches nearly stable value after enough long time, for example 1000s. Relation between stationary temperature increase and loading level is given in part (d). Dissipated energy calculation and explanation are presented in the Section 4.2.
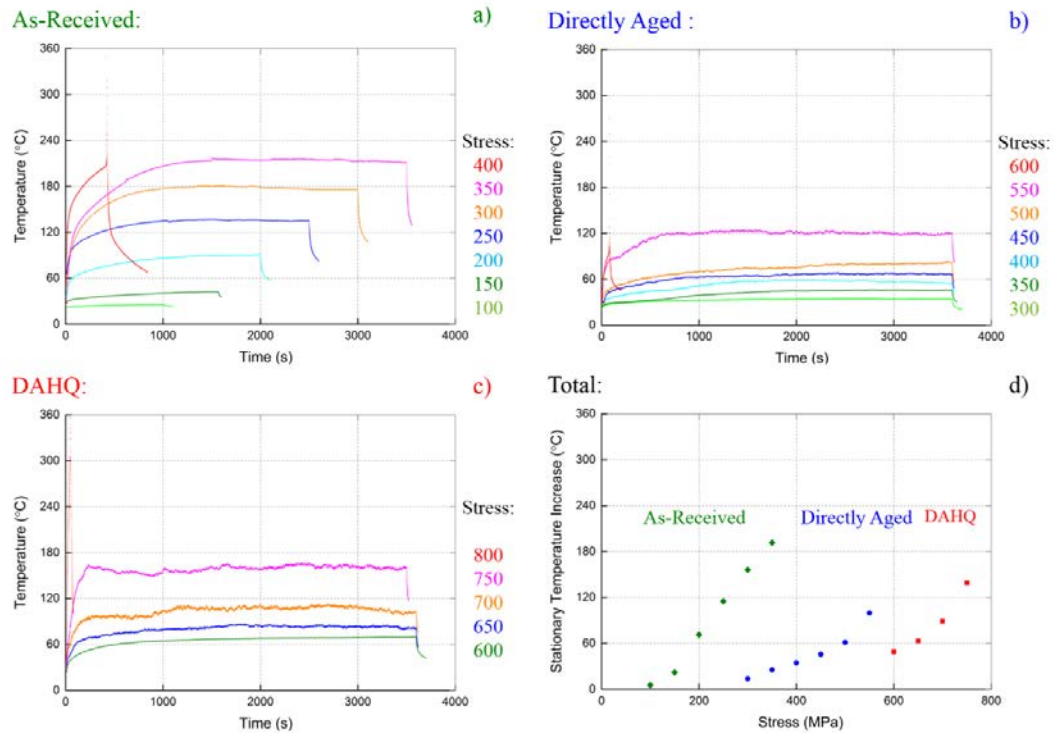
Figure 4.1 Self-heating Phenomenon of Inconel 718 at 20 kHz

It is necessary to point out that absolutely stable cannot reach. Another ultra long time monitoring shows, temperature decrease continuously 1~2ºC/h for As-received specimen (not clear in the curve). It indicated cyclic hardening of this material, similar to low frequency test in Figure 3.23. And it increases slightly for the Directly Aged material, indicating cyclic softening phenomenon, in Figure 3.24.

4.2 Energy Dissipation

0D hypothesis is chosen in the calculation of dissipated energy of Inconel 718 at 20 kHz and room temperature without cooling. The schema of 0D model is shown in Figure 4.2. Maximum temperature of surface used in this calculation.

It is not enough precise to use the 0D model, because all the heat transfer between specimen surface and surrounding is considered by only one constant τ, including conduction with the other part of the specimen, convention and radiation with environment atmosphere. (But it is different to solve this problem, only if change the shape into thin flat specimen with long uniform section. It is not been done in this section.)
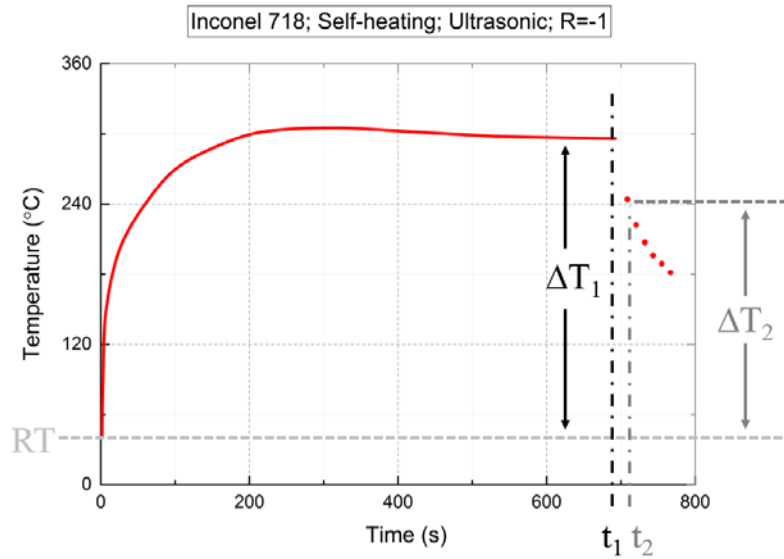
Figure 4.2 Schema of 0D Model for Energy Dissipation Calculation

$$\begin{cases} \rho C \dfrac{d(\Delta T_1)}{dt} = \dfrac{\Delta T_1}{\tau^{0D}} + d_1 = 0 \\[4mm] \rho C \dfrac{d(\Delta T_2)}{dt} - \dfrac{\Delta T_2}{\tau^{0D}} = d_2 = 0 \end{cases} \quad and \quad \Delta T_1 \approx \Delta T_2 \qquad (4.1)$$

So
$$d \approx \rho C \frac{\Delta T_1 - \Delta T_2}{t_2 - t_1} \qquad (4.2)$$

where d is dissipated energy, ΔT is the temperature increase at time t, ρ is density, and C is specific heat.

113

Dissipation of energy and fitting lines during the ultrasonic fatigue test of Inconel 718 at 20 kHz and room temperature are shown in Figure 4.3, The self-heating are calculated based on the data presented in Section 4.1. Dissipated energy always presents as the power per unit volume of the material. W/m^3, $J/(s \cdot m^3)$ and $J/(m^3 \cdot cycle)$ at 20 kHz are the same shaped units.
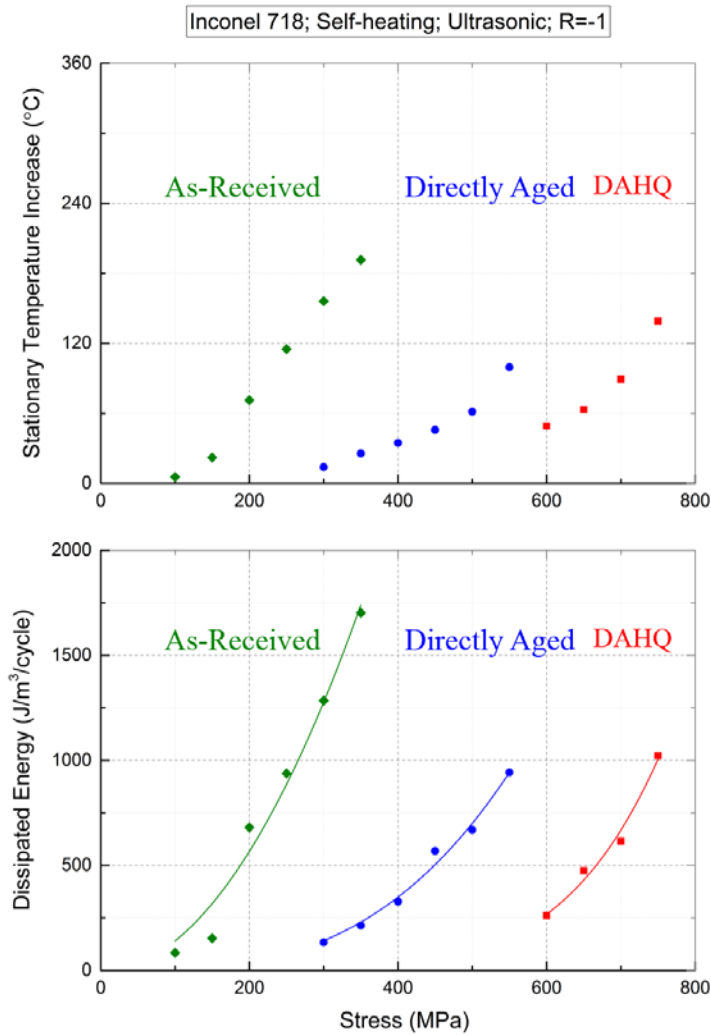
Figure 4.3 Stationary Temperature Increase and Dissipated Energy Fitting

Exponential function is chosen for the fitting of experimental data, due to the widely used in another references. Vertical axis Y is the dissipated energy per cycle and the horizontal axis X is the loading stress. The exponential fitting equation is given as Equation (4.3):

$$d = D \cdot \sigma^n \tag{4.3}$$

where **d** is dissipated energy, **σ** is loading stress, and **D/n** are fitting constants.

Fitting parameters for dissipated energy vs. stress curve of Inconel 718 at 20 kHz and room temperature are given in Table 4.1. Good agreement is obtained meaning that the dissipated energy during the ultrasonic fatigue test is related closely with the loading stress, and the calculation seems good, even using simplified 0D model, no matter for which material.

Table 4.1 Fitting Parameters of Dissipated Energy vs. Stress Curve

	D	n
As-Received	$1.352*10^{-2}$	2.0082
Directly Aged	$2.542*10^{-6}$	3.1269
DAHQ	$8.337*10^{-15}$	5.9415

Exponent n of these 3 kinds of material shows significant differences. For the As-received material, it is really close to number 2, which is widely used by another author in references, in self-heating simulation for ferrous metal. For the Directly Aged and DAHQ material, this index increases as the ultimate or fatigue strength increases. It seems more sensitive to the loading level. If compare the absolute value of dissipated energy at the same stress level, it decreases as the ultimate or fatigue strength increases.

Coefficient D is used for adjust the absolute value. In my opinion, it cannot reflect the difference between these materials, even if they pass more than 12 orders of magnitude.

4.3 VHCF Behaviour of Inconel 718

VHCF results of Inconel 718 under different heat treatment at 20 kHz and room temperature without any cooling has shown in Figure 4.4. The number of cycles shown here corresponding to the total fatigue life time. This number counts from the start of the group until its stop automatically, due to the frequency loss. Morphology of fracture is show in Section 5.2. Prediction of fatigue life and fitting of this test data are presented in the next Section 4.4.

It is clear that Inconel 718 specimen still breaks after the traditional endurance limit (10^7 for ferrous alloys like carbon steel, and 10^8 for non-ferrous metals). It seems to confirm that "There is no infinite fatigue life in metallic materials"[35].
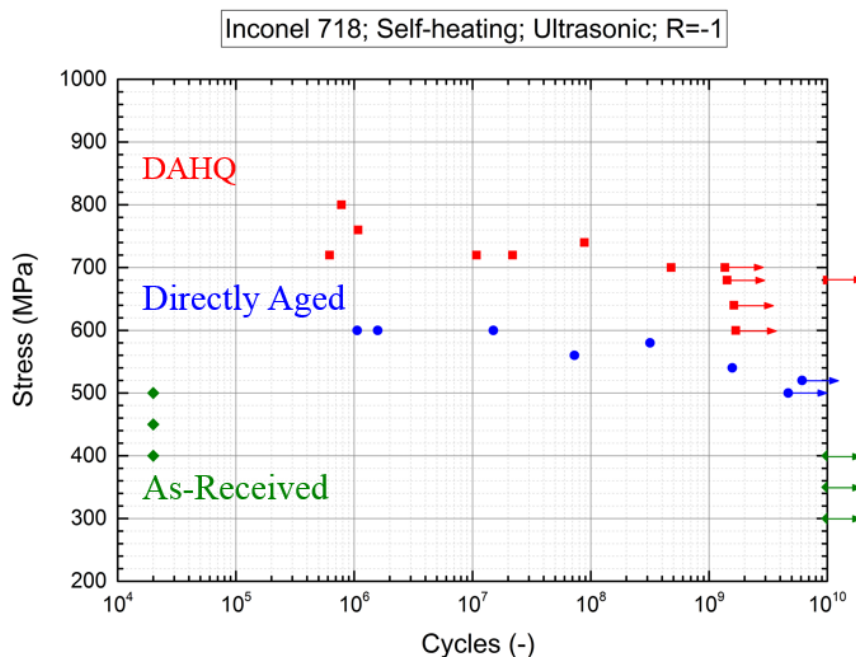
Figure 4.4 VHCF Behaviour of Inconel 718 at 20 kHz with Self-heating

For As-received material (olive), several remarks must emphasize here that, at the begging, 20000 or 10^{10} cycles is not the exact number of cycle when failure occurs, it only represents the minimum or maximum life time of this S-N curve, in order to avoid very long horizontal axis. Indeed, all the specimens which loaded over 400 MPa break immediately, even less than one second, before any stable vibration been detected. On the opposite, specimens never break when loaded under 400 MPa. While, under the exact 400 MPa loading level, several specimens break immediately and others never break. It seems that there is the threshold, but its activation also highly depends on other conditions, for example microstructure or environmental effects.

For Directly Aged material, fatigue life is sensitive to loading stress level. Only difference of 100 MPa (or 8.3% of yield strength) is found, corresponds to the fatigue life between 10^6 and 10^{10} cycles (10000 times). In another words, for civil or commercial engineering component, significant improvement could be achieved through minus some value, instead of divide the safety factor which always 2~3. (This idea is only obtained from this fatigue test result using simple specimen, maybe cannot be suitable for the real engineering component.)

For DAHQ material, fatigue life shows large scatter at some stress levels, for example 720 MPa. Nearly 3 orders of magnitude are reached under the same stress. Similar situation happens also at 700 MPa. Besides this, the tendency of S-N curve of DAHQ 718 is really close to last Directly Aged one. Corresponds to the fatigue life between 10^6 and 10^{10} cycles, the difference of loading stress is 100 MPa, as for Directly Aged material.

There is another thing need to explain that the points of 600 and 640 MPa seem meaningless to this curve. The presence of these two points coming from my error at the beginning of the test with this material. The first loading level is difficult to choose, due to the lack of fundamental information. But it should be better than aged by ourselves. So, the first loading setting has chosen the maximum for the aged group, 600 MPa, and then with relatively larger step of 40 MPa, instead of 20, until finding the first fatigue fracture at 720 MPa. That is why there are 4 points totally close to the 10^9 cycles without crack. This kind of waste should be avoided.

Directly Aged and DAHQ curves shows the same tendency or slopes, maybe indicates the same mechanism of fracture. It could assume that there may be horizontal asymptote after enough long time test. For example, at 680 MPa of DAHQ material, crack don't appear until even up to 10^{10} cycles. Or 500 MPa of directly aged material, because $6*10^9$ cycles test has already finished without crack. This is still waiting for validate in the future.

Fatigue strength can be normalized by divided yield strength or ultimate strength. But this don't been done in this article, because of the lack of basic mechanical properties of DAHQ material.

4.4 Life Prediction

Prediction of fatigue life and fitting of test data of Inconel 718 at 20 kHz and room temperature without cooling is shown in Figure 4.5. Scatter of the results of fatigue test is now accepted to be an experimental and physical fact. It is generally far too difficult or expensive to entirely remove some of the causes of experimental error. This is why statistical methods have to be used in order to experimentally determine the characteristics of the fatigue phenomenon.
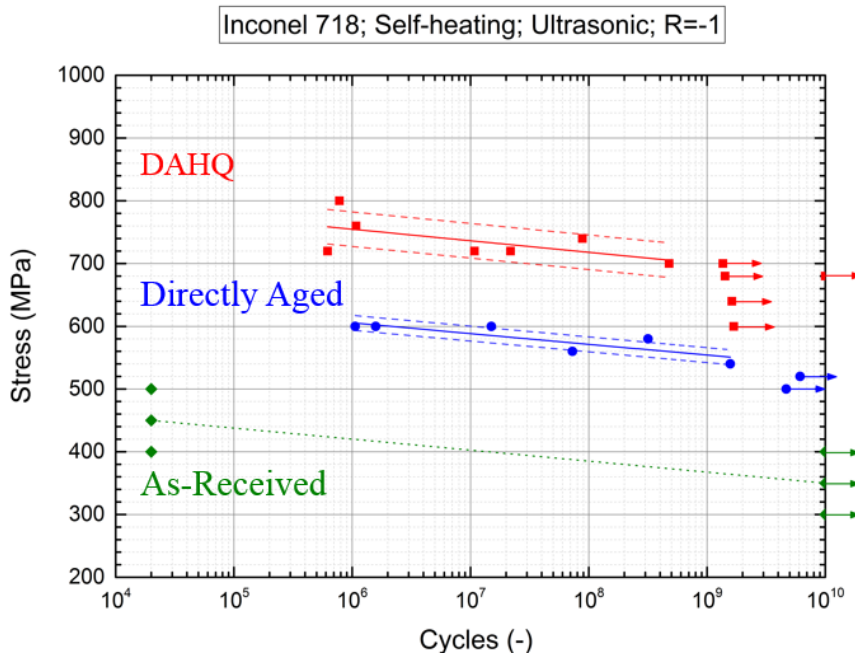
Figure 4.5 VHCF Experimental Data and Fitting of Inconel 718 at 20 kHz

Dengel or Basquin shaped model (4.4) without horizontal asymptote is chosen to fit the test data, due to the widely used in the literature:

$$\log_{10} N = \lg N = a - bS \qquad (4.4)$$

The original Equation (4.4) is rewritten into (4.5) in order to making that vertical axis Y is the stress and horizontal axis X is the common logarithm of the fatigue cycle number:

$$S = A \lg N + B \qquad (4.5)$$

where **S** is loading stress, **N** is number of life cycles, and **A/B** are fitting constants.

Fitting parameters of the S-N curve of Inconel 718 at 20 kHz and room temperature is shown in Table 4.2. It is necessary to indicate that 2 points at 600 and 640 MPa of the DAHQ material don't take into consideration for this fitting, because they are coming from my error of choice. The detail reason shows also in the Section 4.3. Good agreement means that the fatigue performance of directly aged and DAHQ edition Inconel 718 is really stable, and this equation is suitable for the fatigue life fitting.

Table 4.2 Fitting Parameters of S-N (Stress vs. Number of Life Cycle) Curve

	Sample Number	Standard Deviation	*A*	*B*
As-Received	/	/	/	/
Directly Aged	6	11.87	-17.17	708.68
DAHQ	7	27.55	-18.42	865.36

Slope *A* of these 2 kinds of material shows nearly the same tendency, maybe related to some basic characteristic of the material. Even if there are many differences between these 3 editions under different heat treatment, they are nickel based high temperature superalloy Inconel 718.

Intercept *B* maybe proportional with some mechanical parameters, like yield strength or ultimate strength. It is not discussed here, because there is not enough fundamental information about DAHQ material.

Assuming that the distribution of the loading stress for the given fatigue life cycle follows the normal distribution, also called as Laplace Gauss distribution. The fitting line shown above happens at the 50% probability of fatigue fracture. Therefore, the prediction of P-S-N curve (for example P=84% and 16%) can be obtained through addition and subtraction one standard deviation, shown by the dot line in Figure 4.5.

Chapter V Results Analysis

The influence factor on the fatigue life are preliminarily disclosed, through comparing our test results with literature under different condition by another team. Fracture morphology of Inconel 718 with different heat treatment are studied. Fracture mechanism are analyzed at the end of this chapter.

5.1 Influence Factor Analysis

Influence factors on the fatigue life, for example heat treatment, grain size, loading mode/frequency, test temperature, etc. are analyzed in this section through compared our monitored result with other cases from the literature. There is few published articles (less than 20) about the ultrasonic fatigue phenomenon under low stress and high frequency loading. Furthermore, there is no available results which allow to evaluate the influence of only one variable.

4 groups of data introduced in the Chapter I Literature Review are selected totally for comparison in this section. The test condition differences include:

- Directly aged vs. Typical heat treatment solution, quench and aged;

- Ultrasonic full reversed tension compression vs. Rotary bending;

- Self-heating without cooling vs. Pulse-pause mode.

Team Kawagoishi

In 2003[111], 2005[112], 2007[113], 2008[114] and 2010[115], team Kawagoishi from Japan investigated the influence of grain size and loading mode on the fatigue properties of Inconel 718. All the test points from these articles are grasped and combined with our data, in Figure 5.1.

The difference between these points and our data should be emphasized at the beginning. Typical heat treatment is used in this test, in other words, solution follow the step fast cooling water quench, then aged, shown also in Table 3.1.
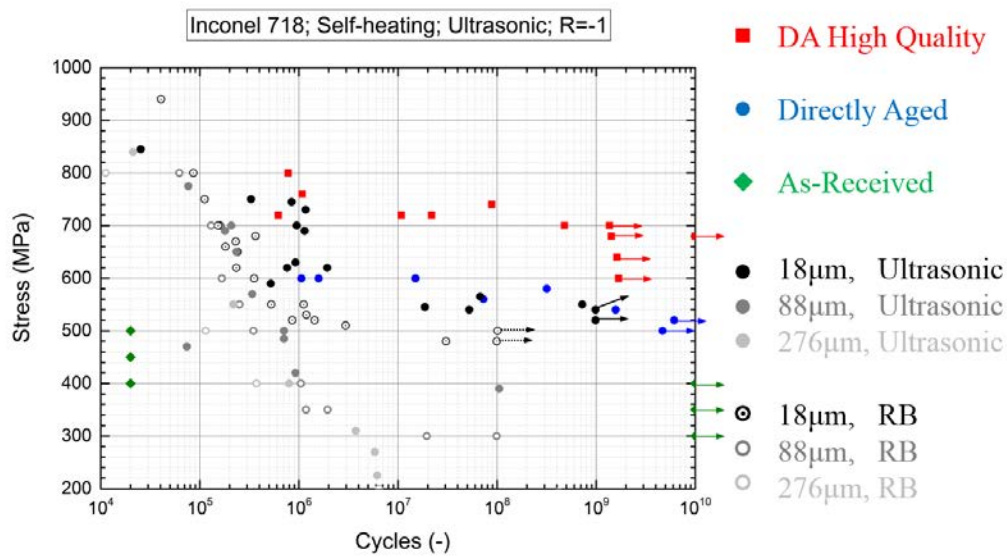
Figure 5.1 VHCF Property Comparison with Team Kawagoishi

All the points by ultrasonic loading are marked as solid point in this figure. Pulse-pause manner has applied in this test to minimize the temperature rise due to the internal friction of material. The pulse time varied in the range of 20~50ms, and the pause between 1000~2000ms. The maximum temperature increase at the test section of specimen has controlled below 5~8ºC during all the test, differ from the self-heating in our test.

Other results by rotary bending are marked by hollow circle. Loading frequency of rotary bending is always 52.5Hz in the most circumstances, because the standard speed of commercial motor is 3150 rpm. Self-heating phenomenon is insignificant under not high frequency (or strain rate), and specimen temperature is not indicated.

For the material with smaller average grain size 18μm (in black), it seems that there is a horizontal asymptote after enough long time loading, 10^8 cycles for rotary bending and 10^9 for ultrasonic. While, for the material with larger grain size, no matter 88μm (dark gray) or 276μm (light gray), S-N curve is straight line without inflection and mixed, in other words, fatigue life increases continuously as loading decreases without fatigue limit. It is not very clear due to the lack of test data in the ultra long life range.

Between 10^6 and 10^9 cycles, the test data of fine grain material (black points) is really close to our directly aged material data (25~27μm, blue points), even if test condition is different. It seems that the average grain size is the most important influence factor on the VHCF property. Besides, the pulse-pause mode, as well as the temperature caused by self-heating is not decisive factor. According to the self-heating result in Figure 4.3, maximum temperature of aged material under 500~600 MPa loading is less than 120ºC, which is not high for the Inconel 718 which design for the nearly 550ºC use condition.

Test data by rotary bending (black hollow circle) shows the same tendency with that by ultrasonic loading (black solid point), while lower of nearly 40 MPa. It can be explained by the stress distribution through the section, because maximum is only at the surface of specimen, and close to zero on the axis.

Team Duan and Shi

In 2010[116] and 2013[96], team Duan and Shi from China investigated the very high cycle fatigue behaviour of Inconel 718 by ultrasonic and rotary bending. All the test points are grasped and combined with our data, shown in Figure 5.2.

The difference between these points and our data should be emphasized, typical heat treatment is used in this test, with an average grain size around 10μm. Air cooling has applied during the whole process, making sure the approximate RT. (The geometry of specimen in this article is not indicated. Air cooling is not enough for my specimen with diameter φ5mm.)
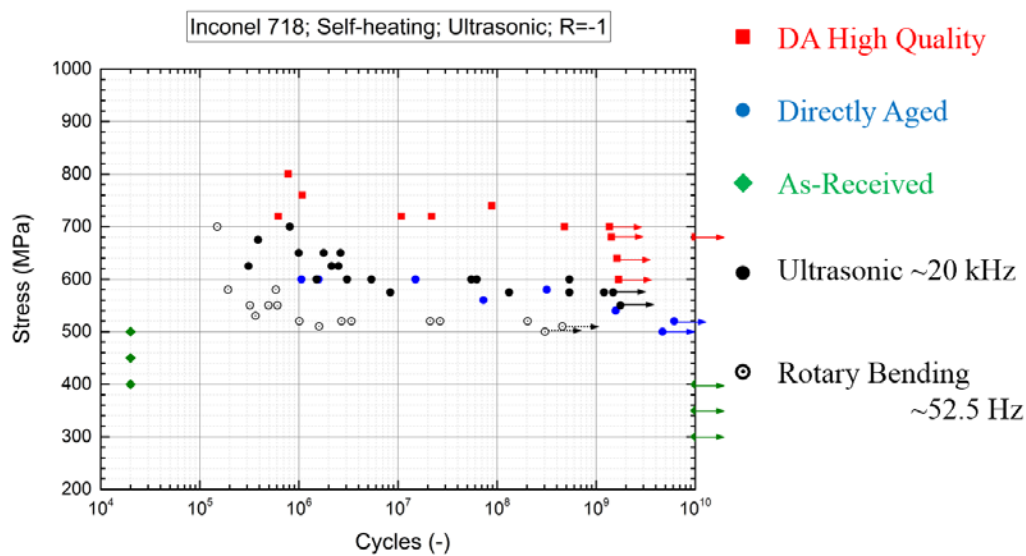
Figure 5.2 VHCF Property Comparison with Team Duan and Shi

Good agreement appears between these two groups of test data using ultrasonic loading (solid point). It can also validate that the temperature increase caused by self-heating is not significant factor in VHCF, as obtained in the previous section. No matter through pulse-pause mode or air cooling, the final purpose is to control the test temperature, if the corrosion influence can be ignored, these two modes are same.

Test data by rotary bending (hollow circle) shows the same tendency but lower of nearly 80 MPa.

Team Amanov

In 2015[121], Amanov investigated the very high cycle fatigue performance of aged and anneal Inconel 718 at RT and elevated temperature, shown in Figure 5.3. The difference between this test and our data is that diameter of specimen is 3mm, so that the area of test section is only 56% of our specimen with diameter 5mm. Air cooling is applied on the specimen for keeping the approximate RT.
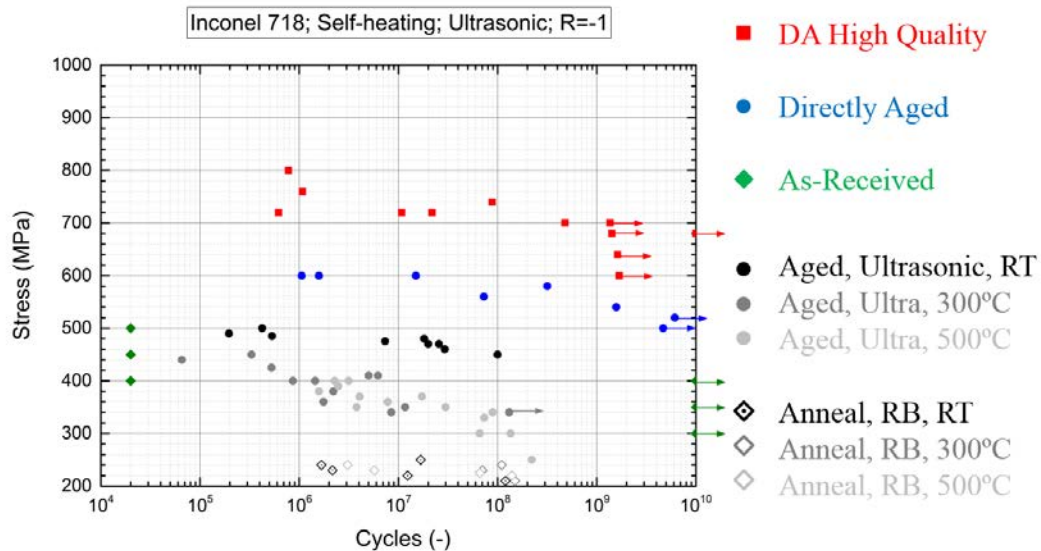
Figure 5.3 VHCF Property Comparison with Team Amanov

Fatigue strength of the aged material under ultrasonic loading (solid point) is obvious higher than anneal material by rotary bending (hollow diamond). The difference between them is over 100 MPa, but still lower than our test data.

For the aged material, fatigue strength at RT is higher than at elevated temperature, while there is no significant difference between for 300 and 500ºC. The tendency of RT data seems horizontal, while the S-N curve changes continuously without fatigue limit for high temperature, maybe accompanying with the change of crack mechanism.

For the anneal material, it may be close to our as-received material, containing ultra-fine grain or non-recrystal grain. But the test is applied by rotary bending with relatively low frequency 52.5 Hz, as well as not high self-heating. There is always fracture between 10^6 and 10^8 cycles.

Team Belan

In 2014[119] and 2015[120], Belan investigated the VHCF behaviour of Inconel 718 under ultrasonic pull push mode at room temperature, shown in Figure 5.4. Anneal follows the aged heat treatment step is applied, but without water quench. The average grain size is approximate 10μm. Fatigue strength in this article is obviously lower than our aged material, and the tendency of S-N curve decreased continuously without fatigue limit.
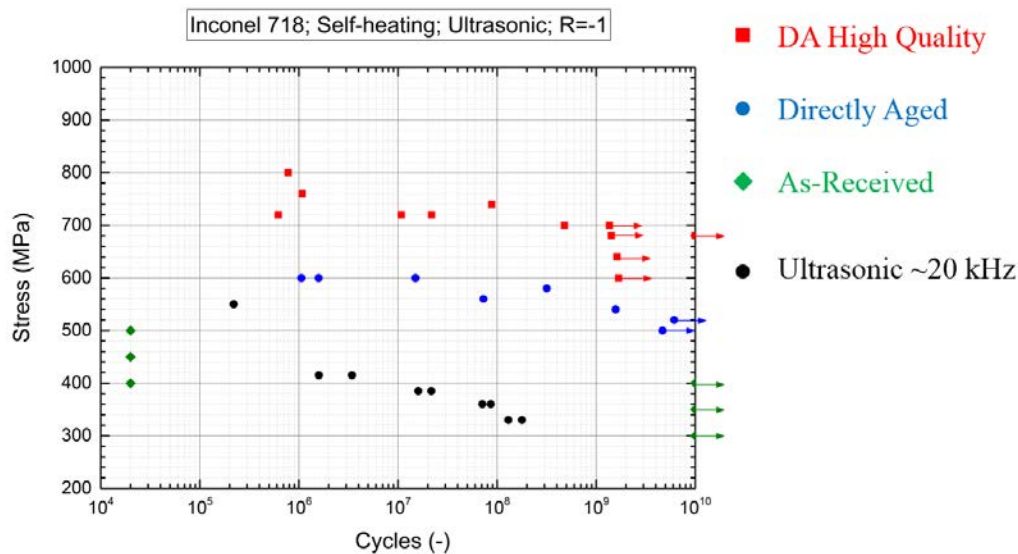
Figure 5.4 VHCF Property Comparison with Team Belan

Section Conclusion

Generally, the fatigue strength varied in the really big range of loading stress. The best performance is the directly aged high quality edition, fatigue strength at 10^6 cycles is 800 MPa and at 10^9 is 700 MPa.

Then the material aged in LEME, solution quench aged material of team Kawagoishi and Duan shows really close results between 10^5 and 10^9 cycles, but 100 MPa lower than the DAHQ group.

Afterward, aged material of team Amanov and Belan performs much worse than the last group, with difference of more than 120 MPa. The slope is also steeper, meaning that only ultra-low loading can be sustained for the ultra long life demand.

This kind of difference maybe comes from the test error. But it seems there is several editions of Inconel 718 in the market, even if the same name is used.

5.2 Fracture Morphology

Fracture surface (parallel or vertical to the specimen axis) are observed using optical camera (not microscope) and scanning electron microscope. Through comparing the morphology feature of fracture, the crack mechanism and the influence factor on fatigue life could be disclosed.

It is necessary to point out that all the specimens don't break into 2 parts automatically, in another words, machine stopped before the crack propagates to all the section, not like the situation of plate shaped specimen. The cracked specimen is been pulled by another tensile machine for the axial fracture image.

Before the classified discussion by heat treatment and total fatigue life range, some commonality of all the fracture can presented here. Only one single initiation site exists in all the situation, regardless of the heat treatment, loading level, temperature or fatigue life.

There is no "fish-eye" in all the fracture, which is the specific characteristic in some VHCF tests. In another words, all the initiation site is at surface or close to subsurface, not in the bulk of the specimen. Residual stress maybe the possible reason why initiation locates at subsurface instead of surface, but it is difficult to measure due to the hourglass shape.

The propagation duration distributes from several to tens of seconds, depends on the total life, and it is always less than 1%. The counting of the propagation life is based on the surface temperature. It will increase suddenly and greatly when crack propagated, and decrease immediately when machine stopped. This kind of counting can qualify only, but it is not suitable for quantify.

After the commonality, fracture can be classified with respect to heat treatment and total fatigue life range. Because there is some differences between them, like initiation zone or propagation trace. In this section, the total life in the range of 10^7 will be defined as relative "Short Life", while the fatigue life close to the level of 10^9 will be called as relative "Long Life". For each heat treatment material, only one point less than $5*10^7$ cycles life and another long life one will be chosen for the fracture analysis, shown in Figure 5.5 and Table 5.1.
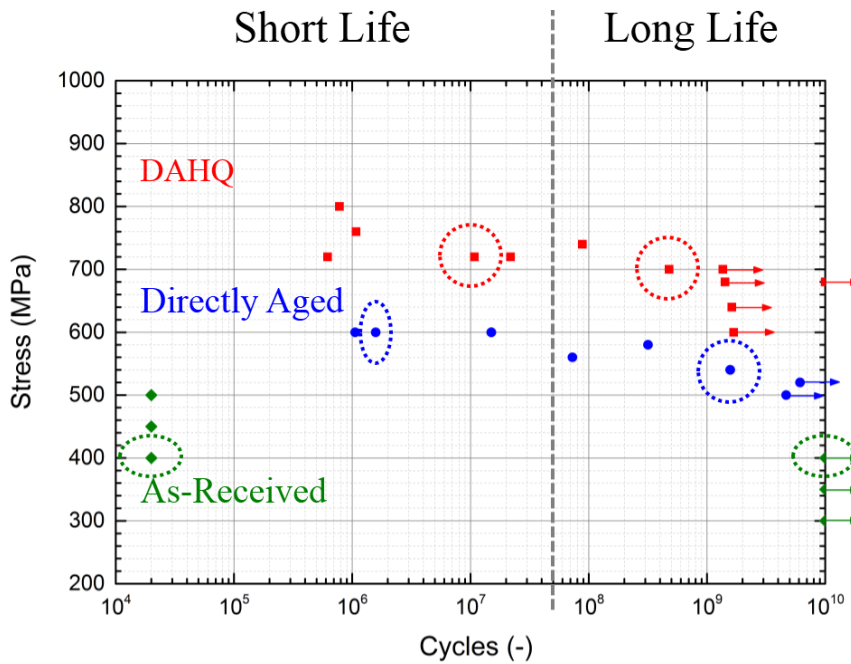
Figure 5.5 Points Chosen for Fracture Analysis

Table 5.1 Points Chosen for Fracture Analysis

	Short Life	Long Life
As-Received	400MPa; <1s	400MPa; never
Directly Aged	600MPa; $1.58*10^6$	540MPa; $1.57*10^9$
DAHQ	720MPa; $1.50*10^7$	700MPa; $4.78*10^8$

In the following, the analyses are given for As-received, Directly Aged, and DAHQ materials. The situation of As-received material is the most complicated than the others. Typical fatigue fracture doesn't exist in the as-received material, and it could be skipped over for definite and rigorous analysis.

5.2.1 As-Received

As mention before, for the As-received material specimen, all the test with loading level more than 400 MPa stop immediately, and the $2*10^4$ cycles (1 second) is only the approximate value to represent the minimum life in the S-N curve, not a precise value. At the same time, the specimen never breaks when loading is less than 400 MPa, 10^{10} means the maximum life of this S-N curve.

The most important and difficult situation is the 400 MPa loading. It seems that there is a threshold at 400 MPa to active some mechanism of fast crack initiation or propagation. But this kind of activation also highly depends on other environmental conditions. So, two specimens under the same 400 MPa loading, but with short and long life are chosen for the fracture analysis.
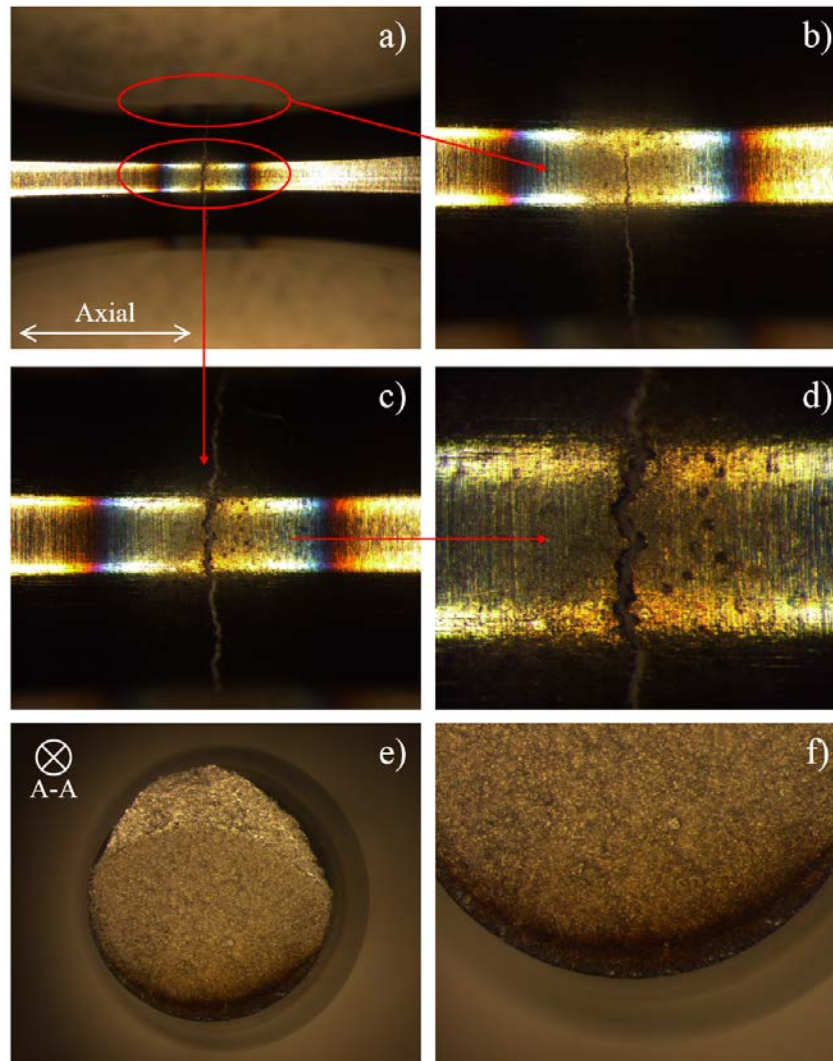
Short Life

Figure 5.6 Optical Imaging of As-received Inconel 718 (Short Life)

Optical imaging of short life specimen and fracture surface for As-received Inconel 718 is shown in Figure 5.6. It is clear that there is severe burn ring around the crack, and it doesn't disappear at the end of crack, shown in the part (b). It means that high temperature is reached during all the test section, and it is not only related to the crack propagation. Different colour inclines that high temperature gradient exists in the short section with axial length nearly 3mm. The limit of our infrared camera is 360ºC. According to the 2D infrared image, temperature of the blue/red zone is already over this limit, so that the temperature in the center should be much higher than 360ºC, maybe 500~600ºC. It must be denoted that the strength of Inconel 718 decreases extremely after 550ºC.

Lots of macro holes exist at the center of this ring, which is the highest temperature zone, shown in the part (d). This kind of holes appear during the test, due to the dropping of grains at the surface. It seems that the crack is the link between some holes. Axial fracture surface imaging (f) validate this point, because dark edge is much lower than the other plane, due to the block dropping.
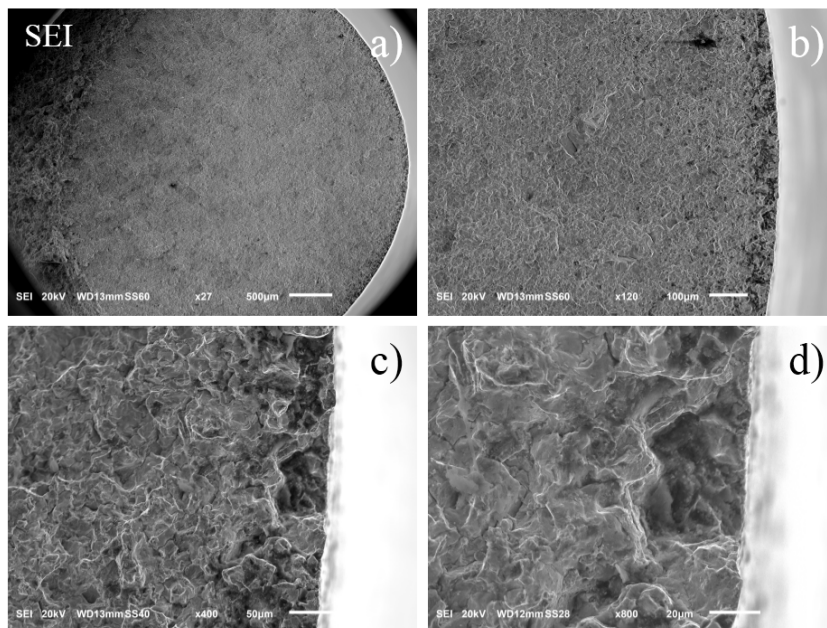
Figure 5.7 SEM Micrograph of As-received Inconel 718 (Short Life)

SEM micrograph of short life fracture surface for As-received Inconel 718 is shown in Figure 5.7. It seems not the typical fatigue fracture, because radial macro stair marks or circumferential beach marks or micro striations, which always appears together in the fatigue fracture, is missing. The radial depth of burn dark edge and holes is nearly 50μm. The mechanism of the formation of such holes is still not easy to explain.

Long Life

Optical imaging of long life no crack specimen for As-received Inconel 718 is shown in Figure 5.8. Same burn trace ring and dropping holes appear in the surface of specimen, while it not breaks after 10^{10} cycles. This no crack specimen has been cut at the center using the same processing with metallographic sample. Ultra low cutting and polishing speed with water cooling ensure that no additional change happens on the surface, shown in Figure 5.9.
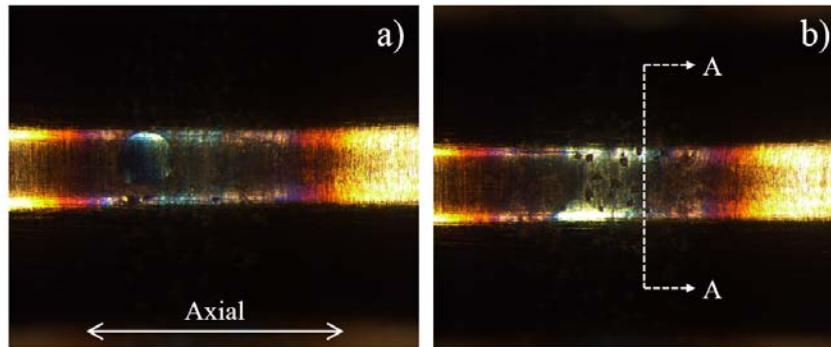
Figure 5.8 Optical Imaging of As-received Inconel 718 (No Crack)

Close to the aged material in Figure 3.12, "fine grain band" disappears and it seems that there is unclear, discontinuous trace in original "non-recrystal" grain. Maybe dynamic recrystallization happens in this situation under cyclic loading, even if temperature is not enough high.
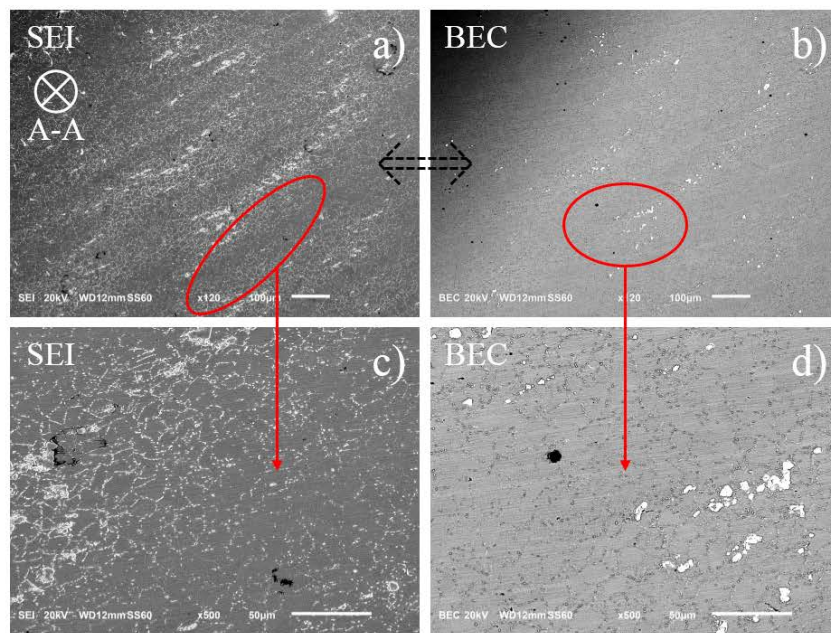
Figure 5.9 SEM Micrograph of As-received Inconel 718 (No Crack)

Accumulated

In order to validate the previous idea, another accumulated test is proposed. After the long test under loading 400 MPa over 10^9 cycles, tested loading is improved up to 450 MPa continuously without any pause, through adjust the voltage on the piezoceramic for changing the vibration displacement.

The specimen persists nearly 10 seconds, instead of crack immediately. This kind of phenomenon proves that there is really some change after the long time and high cycles of cyclic loading. The elevated temperature plays another important role for this kind of change, even if much lower than the dynamic recrystallization (DRX) temperature 950ºC.
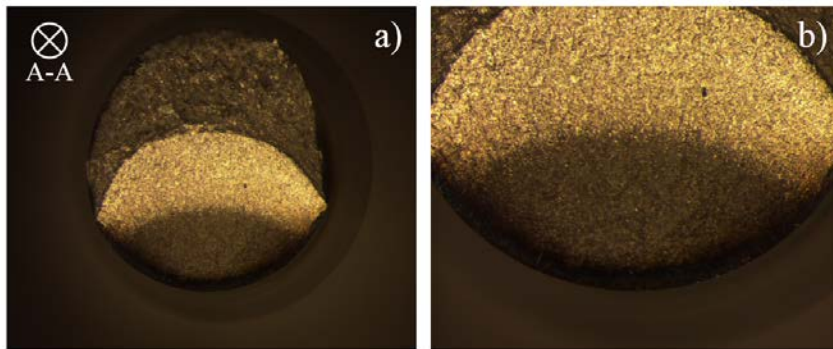
Figure 5.10 Optical Imaging of As-received Inconel 718 (Accumulated)

Optical imaging and SEM micrograph of accumulated loading fracture surface for As-received Inconel 718 is shown in Figure 5.10 and Figure 5.11. It is clear that another flat and smooth propagation area appears. Area I in Figure 5.11 (d) is similar to the unstable appearance, with Figure 5.7 (c). While the micro striations in area II inclines the stable quasi-cleavage crack propagation, like the directly aged material shown in Figure 5.13. The significant border implies the different mechanism, maybe associated with the change of stress intensity factor (SIF). The mechanism of the typical fatigue crack initiation and propagation will be presented in the next section.
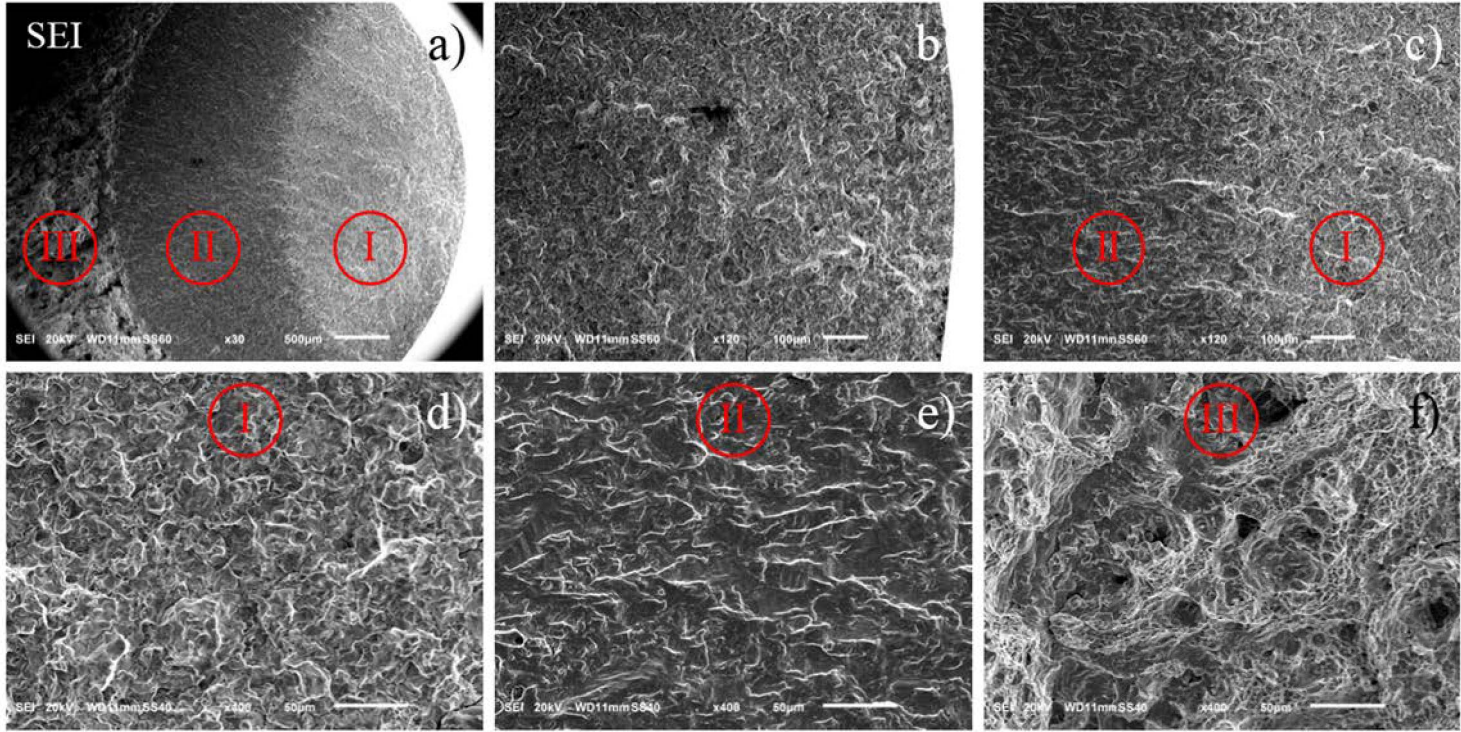
Figure 5.11 SEM Micrograph of As-received Inconel 718 (Accumulated)

5.2.2 Directly Aged

Optical imaging of specimen surface and fracture surface for Directly Aged Inconel 718 is shown in Figure 5.12. It is difficult to see the crack, because it is not open and there is no burn trace along it. It inclined that temperature don't increase too much during the test. But there is a visible crack indeed in the part (b), pointed by the white arrow.

Optic imaging of short life and long life specimens look really same, presented only once in Figure 5.12.
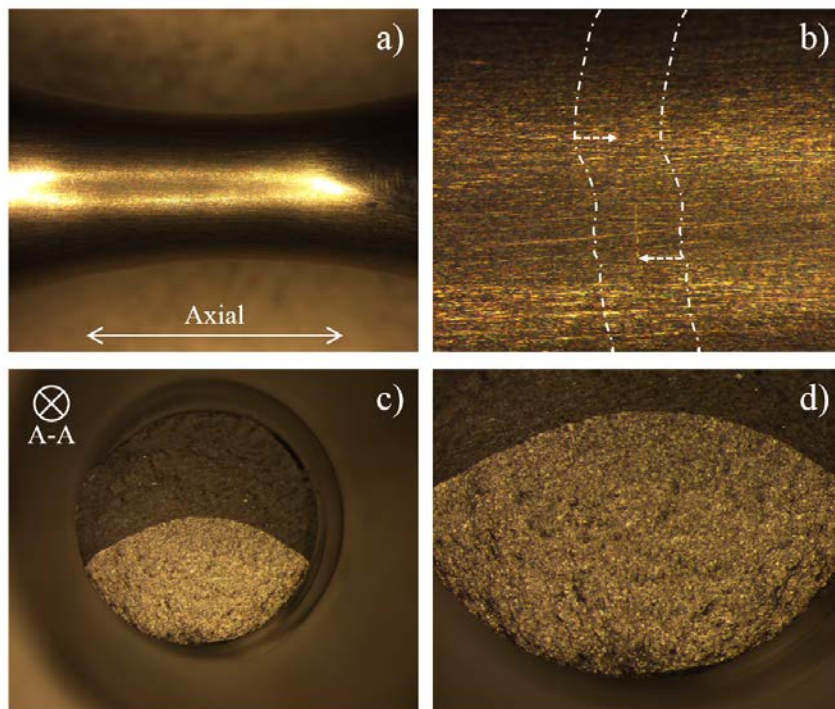
Figure 5.12 Optical Imaging of Directly Aged Inconel 718

Short Life

SEM micrograph of short life specimen fracture surface with Directly Aged Inconel 718 is shown in Figure 5.13. It's widely noted that in the ultrasonic fatigue test, the fracture surface can be generally divided into 3 typical areas, shown also in zone (a).

- I   Initiation area with relatively flat surface;

- II   Propagation area with distinctly rough area and with radial streaks along the crack propagation direction;

- III   dimples due to overload from another tensile machine.

In some literature, this kind of appearance can be also divided into 4 parts. Some authors separate area I into 2 parts, because the existence of fine granular area (FGA), also called as optically dark area (ODA), shown in the middle of part (b) and (d) of Figure 5.13. Other authors separate area II into several parts, according to the difference of crack growth rate (CGR): near threshold regime, Paris regime, and rapid propagation regime.

While, these kinds of difference, no matter FGA/ODA or regime, cannot exist in all the situation. So in this article, only 3 parts can be marked: initiation, propagation and dimples.

For this short life specimen with loading 600 MPa and total life $1.58*10^6$ cycles, the crack initiates at a subsurface smooth facet, shown in Figure 5.13 (c). The facet length is nearly 50μm and locates at 100μm from the specimen surface. According to the BSE imaging and EDS analysis of this zone (not shown in this section), the chemical composition of this facet is similar with the surrounding. It's good news that precipitate particle don't be the initiation, even if the micro hardness is much larger than the based matrix, shown in Table 3.7. Because the inclusion particle tends to decrease the fatigue strength seriously.

But meanwhile, the formation of such facet is not clearly explained up to now. Some authors explain that such fracture surface pattern comes from sliding plane. While, other authors propose twining mechanism to explain the very smooth surface. From my point of view, maybe it is grain boundary or twin boundary which already exist before test, or which are generated during the test.

Quasi-cleavage (or cleavage-like) circumferential beach marks, radial stair marks and micro fine striations appear together in the area II, with the increasing of stress intensity factor (SIF), which indicate the stable crack propagation.
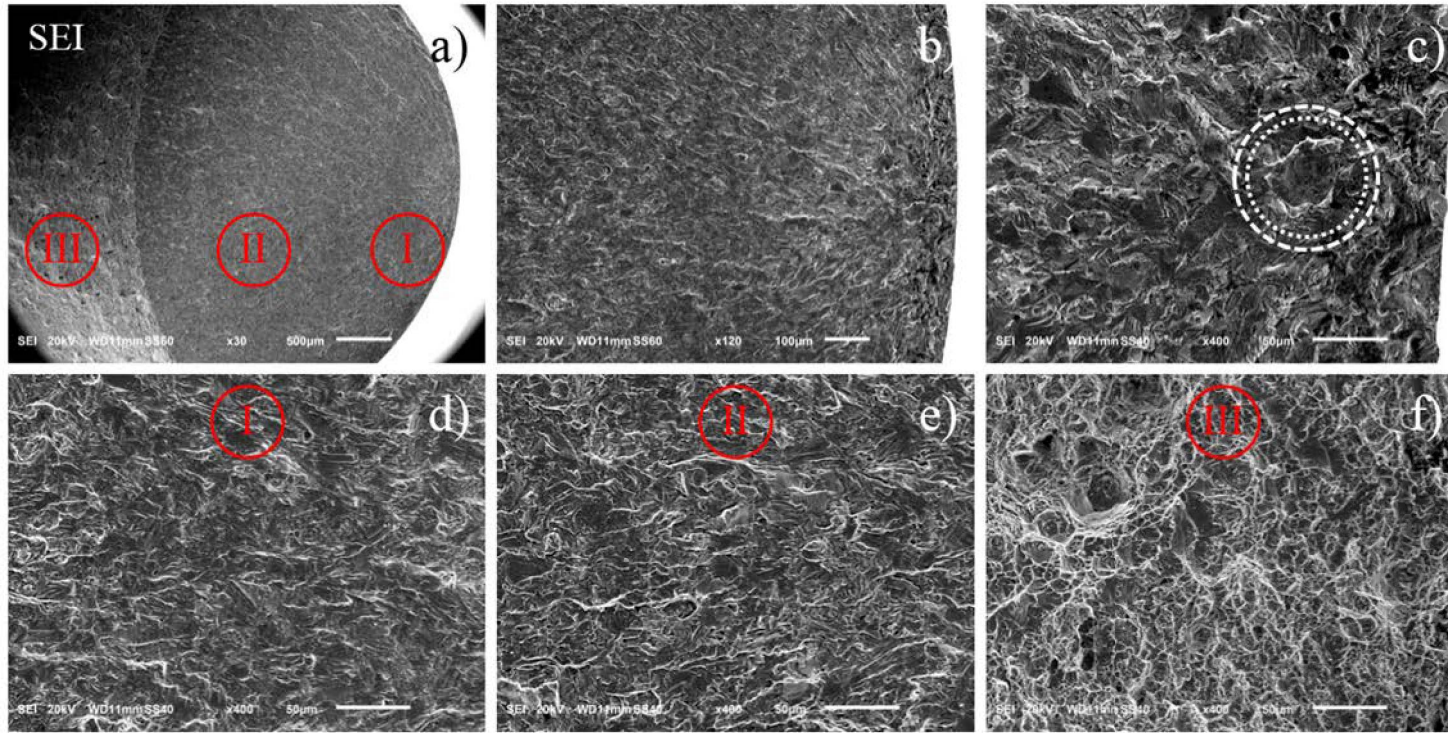
Figure 5.13 SEM Micrograph of Directly Aged Inconel 718 (Short Life)

Long Life

SEM micrograph of long life specimen fracture surface for Directly Aged Inconel 718, under loading of 540 MPa and total life $1.57*10^9$ cycles, is shown in Figure 5.14. The initiation zone (b) is really close to the last short life specimen, except there is no obvious particle or point at the center. The exact crack initiation position cannot be found for the present specimen.

The possible mechanism of nucleating and early growth of the micro crack is presented in the next Section 5.3, through compared with another team in-situ SEM tensile test.

It is necessary to point out that secondary crack in Figure 5.14 (d) (e) and (f), improves greatly the fatigue life. But the mechanism of the formation of such secondary crack is still unclear now. The presence of secondary crack maybe the evidence of extensive plastic deformation ahead of the crack tip.
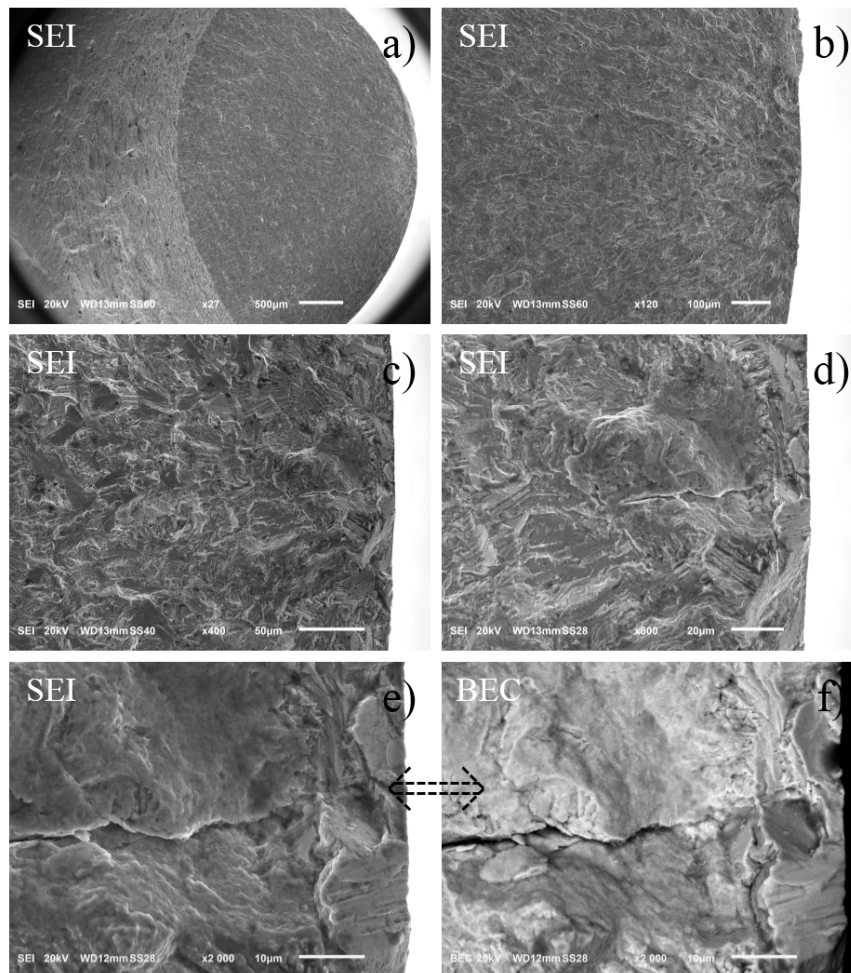
Figure 5.14 SEM Micrograph of Directly Aged Inconel 718 (Long Life)

5.2.3 DAHQ (Directly Aged High Quality)

Optical imaging of specimen and fracture surface with DAHQ Inconel 718 is shown in Figure 5.15. It is similar to aged specimen that there is no burn trace around the crack (a), so that it is difficult to see crack vertical to the specimen axis. For the imaging parallel to the axis, crack propagation area (b/c) seems exists 3 different stages, according to the smooth or coarse morphology, radial slow propagation, radial rapid propagation, and circumferential very rough ridge close to the surface. This kind of asymmetry could avoid the destructive macro crack in the engineering component. While in the VHCF test which focus on the crack initiation, it is not the important topic.

The crack initiation area cannot be analysis using these optical imaging, due to its low magnification. And these imaging of short life and long life specimen look really same, presented only once in Figure 5.15.
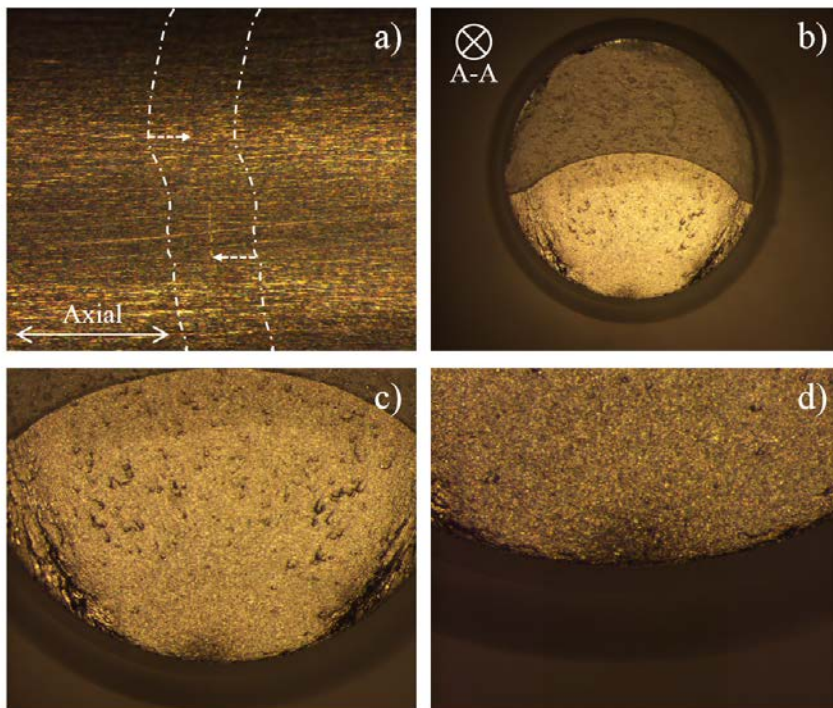
Figure 5.15 Optical Imaging of DAHQ Inconel 718

Short Life

SEM micrograph of short life fracture surface for DAHQ Inconel 718, under loading of 720 MPa and total life $1.50*10^7$ cycles, is shown in Figure 5.16. Like the aged specimen with short life, crack seems initiates at the subsurface particle in part (c), and the chemical composition of this is same with the surrounding according to the BSE imaging shown in part (d). Differ from the last situation, the "particle" could be a cluster of grains or only a big one, not facet, plays an important role in early stage of micro crack nucleate. The diameter of this cluster is nearly 30μm and locates at 50μm from the specimen surface.

The formation of such facet is not clearly explained up to now. As well known, the incomparability in strain between two neighbouring grains or two neighbouring phase can lead to fatigue crack initiation.
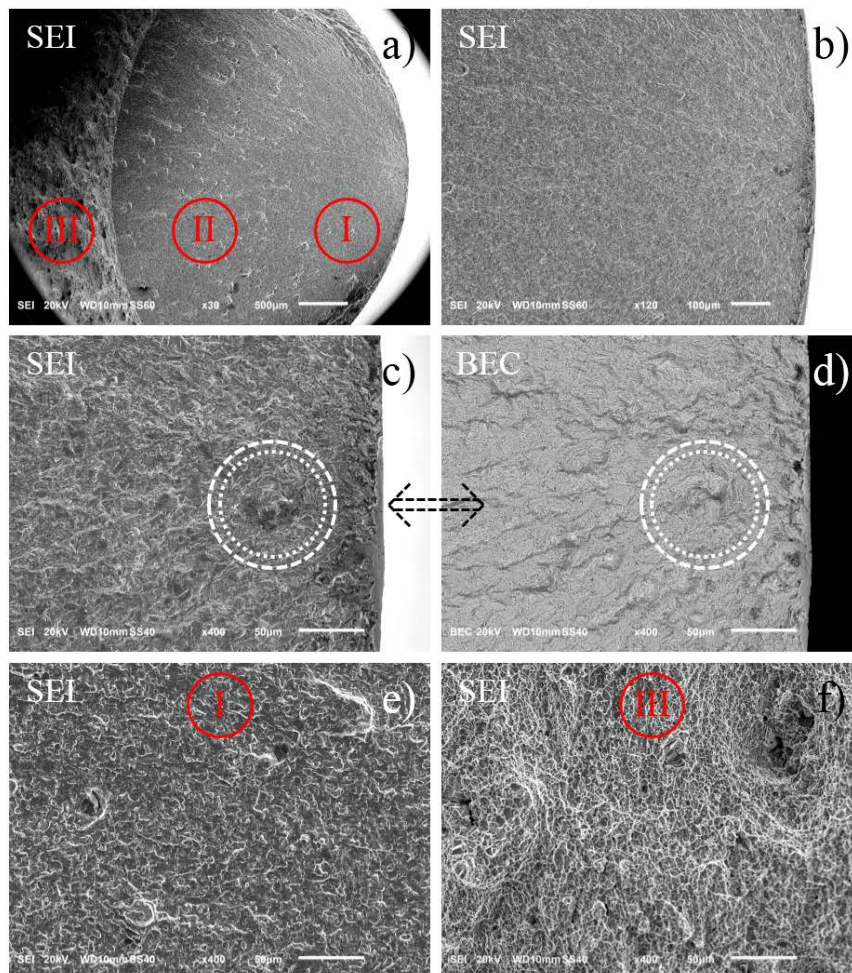
Figure 5.16 SEM Micrograph of DAHQ Inconel 718 (Short Life)

Long Life

SEM micrograph of long life fracture surface for DAHQ Inconel 718, under loading of 700 MPa and total life $4.78*10^9$ cycles is shown in Figure 5.17. The flat initiation zone (b) looks close to the short life situation, but without particle or cluster in the center.

Some large radial ridges can be observed and help us make sure the nucleating zone is close to the subsurface of the specimen. According to the comparison between SEI and BSE imaging for this zone part (e/f), another element seems exists in the tip of these ridges.

However, the EDS point analysis (not shown in this section) indicates the same chemical composition with the surrounding. So, the dark points in the part (f) comes from the shallow by these ridges. No back scattered electron can go into the detector, leading to the dark colour. While it also means that there is steep cliff at the tip of these ridges, which is not easy to see from the part (e).
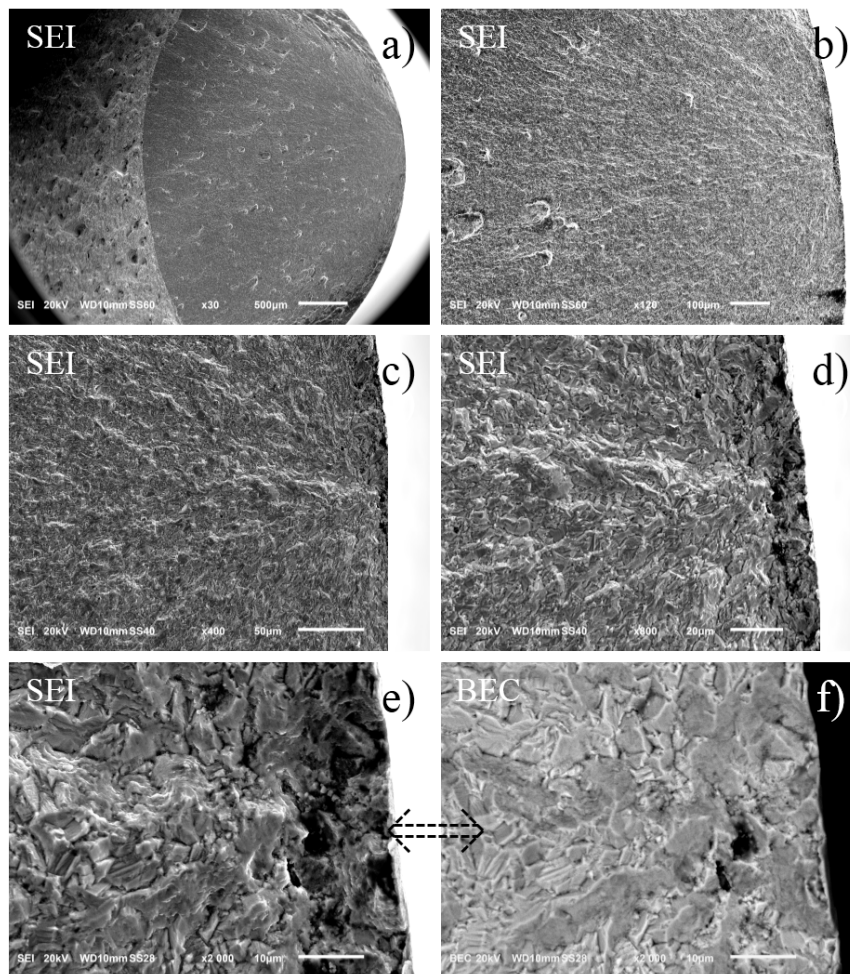
Figure 5.17 SEM Micrograph of DAHQ Inconel 718 (Long Life)

5.3 Fracture Mechanism

Fracture mechanism of Inconel 718 under ultrasonic loading is disclosed, through comparing our micrograph with another some in the literature. Small crack behavior and fracture of nickel based superalloy under ultrasonic fatigue[112] are investigated in the very high cycle domain in ambient air at room temperature.

Typical treatment is used in this test, in other words, solution follow the step fast cooling water quench, then aged. Test performs in pulse-pause manner with pulse length 20 ms and pause 1000 ms. The maximum temperature rise at the most stressed node section surface is controlled below 5~8ºC during the testing.

Surface damage evolution subjected to ultrasonic fatigue is monitored under optical microscope using replica technique, shown in Figure 5.18.
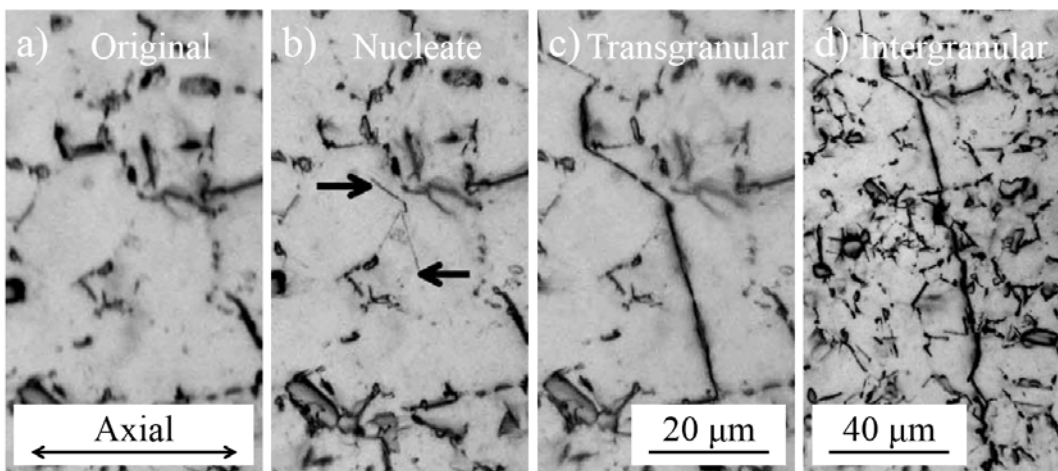
Figure 5.18 Optical Micrograph of Nucleation and Propagation of Small Crack[112]
Stress Amplitude 700MPa, after a) 0; b) $1.4*10^5$; c) $6.9*10^5$; d) $9.5*10^5$ cycles

Small crack nucleates from slip bands near grain boundary (b), then advances initially in transgranular manner (c), and tends to trace grain boundaries in intergranular manner after growing beyond ≈100 μm (d). More than 80% fatigue life spends in nucleating and developing small cracks up to 100 mm. Suppression of crack nucleation and early crack growth contribute primarily to life enhancement in ultrasonic loading[112].

Fracture surface perpendicular to axis is observed by scanning electron microscope, corresponding to the last optical micrograph of specimen surface, shown in Figure 5.19.

Cleavage fracture is emerged in the initial ductile crack growth area, after crack extending over several grains in depth (a), the white dotted line indicates the emerging of cleavage fracture.

Portion of cleavage fracture increases with crack extension at the distance of ≈70μm from nucleation site (b). The transition of fracture mode from transgranular ductile mode to cleavage dominated mixed mode is observed also at the other applied stress levels. Striations become more obvious approaching to final failure (c), implying the steady fatigue crack propagation.

Grain boundaries are often treated as weaker source to form persistent slip bands, irrespective of cyclic frequency and loading condition. PSB happens in the direction close to the maximum shear stress accumulates near twin boundary (d) and degenerates into main cracks.
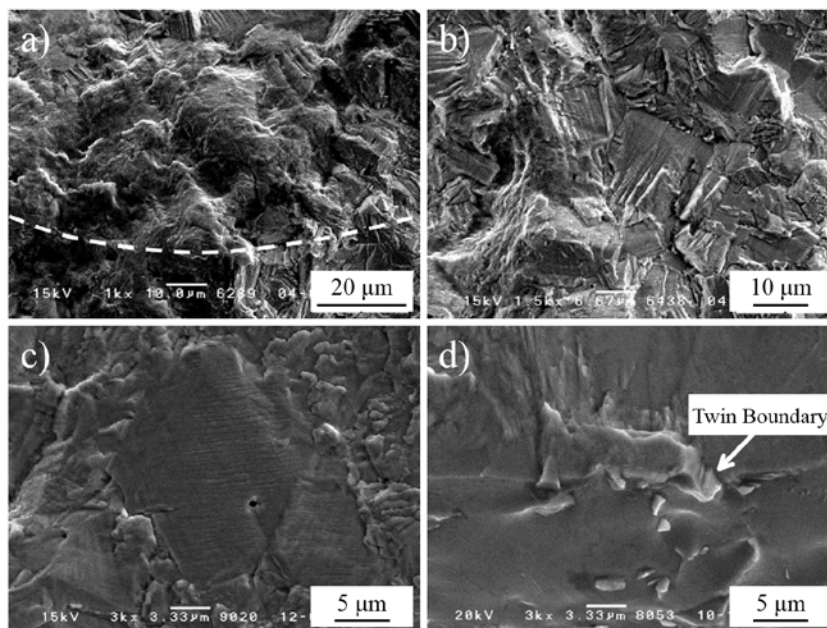
Figure 5.19 SEM Micrograph of Fracture Surface[112]

SEM micrograph of fatigue crack initiation zone for long life Directly Aged Inconel 718, under loading of 540 MPa with total life $1.57*10^9$ cycles, is shown in Figure 5.20. Total width of this image is 300μm, all the morphology in this image is the initiation zone, nothing about propagation.

There is no obvious particle in the center of nucleation zone (N), not like the short life specimen. The crack maybe originates from slip bands or grain boundary, which treated as weaker source. Secondary crack improves the fatigue life, but the mechanism of the formation of such secondary crack is still unclearly now. The presence of secondary crack maybe the evidence of extensive plastic deformation ahead of the crack tip.

Cleavage fracture advances initially in transgranular ductile mode in zone (T), after depth of 80μm from the specimen surface, marked by the smaller dot circle. The trace of gliding happened at 45º direction to the main crack.

Then the crack tends to trace grain boundaries in intergranular manner after growing beyond 150 μm by cleavage dominated mixed mode in zone (I), marked by the larger dot circle.
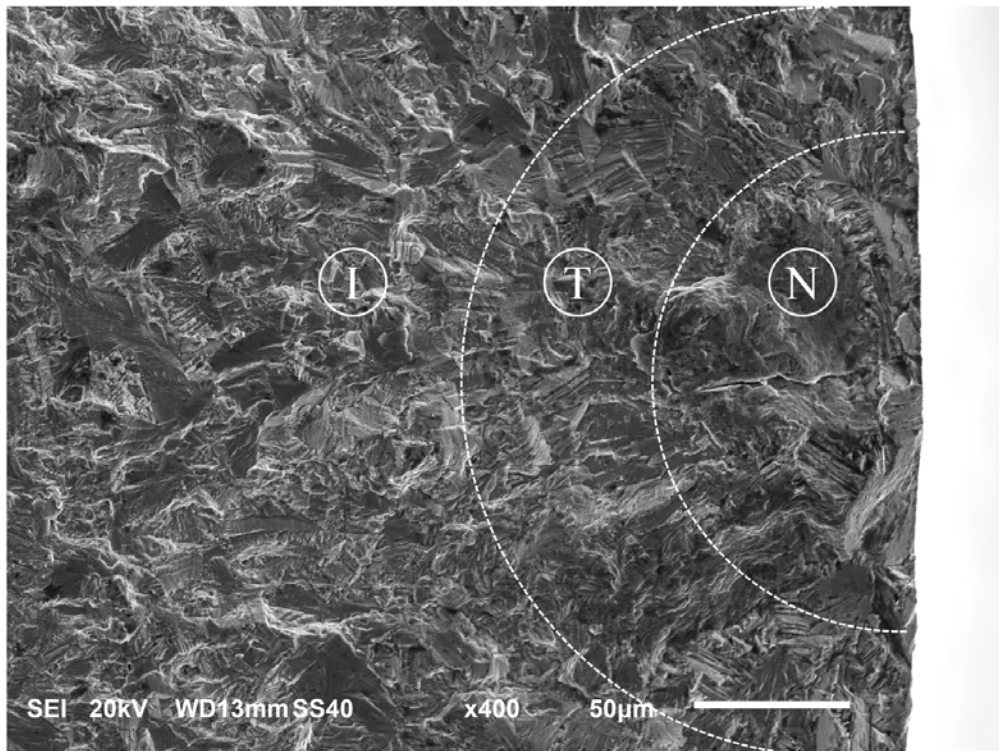
Figure 5.20 SEM Micrograph of Directly Aged Inconel 718 with Long Life

Conclusion and Prospect

Conclusion

Very high cycle fatigue (VHCF) behaviour of Inconel 718 with self-heating without any cooling is studied using ultrasonic test system at 20 kHz in this work. 3 sets of material with different heat treatment are compared. Self-heating phenomenon and S-N Curve is carried out. Fracture mechanism is revealed using optical camera (OM) and scanning electron microscope (SEM). Corresponding to the objective shown in the introduction, the main conclusion of present results can be listed as follows:

1. Acquisition system is improved using NI capture card with LabView for monitoring the frequency, temperature, displacement and so on during all the tests. Keyence® laser sensor with two probes at the top and bottom surfaces of the specimens is used to reveal the resonance frequency and vibration mode. The difference of mean values between these two probes is the elongation of the specimen caused by self-heating phenomenon. Flir® infrared camera is also applied to measure the temperature distribution of the specimen surface due to self-heating.

2. There are total 3 sets of materials with different heat treatment, As-Received (AR), Directly Aged (DA) and Directly Aged High Quality (DAHQ) are compared. The difference of grain size, phase, precipitate particle, etc. is investigated by metallographic micrograph using optical microscope (OM) and scanning electron microscope (SEM). Quasi-static uniaxial tensile property and cyclic stress-strain response is also proposed. Yield and ultimate strength increase obviously after aged heat treatment. The transition from cyclic hardening to cyclic softening also appears.

3. Self-heating phenomenon of Inconel 718 with ultrasonic loading at 20 kHz is significant (up to 300 ℃), because fatigue test is energy dissipated process. Stationary temperature increase of hourglass specimen surface is studied experimentally, it decreases after aged heat treatment. Absolutely stable temperature balance cannot reach, temperature decreases continuously 1~2℃/h for AR, while increases for DA 718, that validates the transition from cyclic harden to soften. Then, dissipated energy is calculated simply using 0D hypothesis.

4. The relation between loading Stress and Number of cycles (S-N Curve) of Inconel 718 at 20 kHz with self-heating is carried out. The propagation duration distributes from several to tens of seconds, depends on the total life, and it is always less than 1%. In another words, more than 99% of fatigue life is initiation life. The tendency of S-N curve is gradual, regardless the material. Only 100 MPa difference is found, corresponds to the fatigue life between 10^6 and 10^{10} cycles (10000 times). Fatigue strength increases obviously after aged heat treatment.

5. Influence factors on the fatigue life are analyzed through comparing our monitored result with other cases from the literature. Good agreement appears between our data of ultrasonic loading at 20 kHz with self-heating and others of rotary bending at 52.5 Hz with cooling. It means that the fatigue life of Inconel 718 is not sensitive to the loading frequency and self-heating phenomenon.

6. There is no "fish-eye" in all the fracture, in another words, all the initiation site is at surface or close to subsurface, not in the bulk of the specimen, regardless the heat treatment of material. For the short life specimen, the crack initiates at subsurface heterogeneous zone, like a smooth facet maybe grain boundary or the precipitation boundary, or like a coarse block maybe the cluster of ultra-fine grains. However, for the long life specimen, there is no obvious particle or point at the center of initiation zone. The exact crack initiation position cannot be found for this situation.

Prospect

Besides these results shown in this thesis, there are still some points can be done in the nearly future, for the better and deeper understanding of Inconel 718. The main prospects of future research can be listed as follows:

1. Ultrasonic piezoceramic test group could be improved for another conditions, like at room temperature (water cooling or pulse-pause mode), at elevated temperature (induction coil or chamber heater), corrosion surrounding or positive stress ratio (R=0.1/0.5/0.7), etc.

2. Self-heating test could be validated again using the standard flat specimen with uniform test section, and at much more stress level. Precise calculation could apply through 2D data by high precision infrared camera, instead of simple 0D hypothesis. Temperature distribution of specimen combined steady surrounding influence (gas flow) and self-heating phenomenon (blade vibration) is also interesting in the field of aeronautics.

3. Fatigue strength of Inconel 718 under actual use conditions is still waiting for complete, like under high temperature or the combination of fatigue and creep. Loading spectrum of aero-plane could be another reference in the future test. Then, the fatigue test of the real component, like turbine disk or blade, is also important topic.

4. Mechanism of crack initiation or propagation of Inconel 718 is still unclear. Quasi-static or In-situ test using flat specimen maybe the solution for this kind of fundamental knowledge.

Reference

[1] R. Royce. The Jet Engine [M]. : John Wiley & Sons, 1986.

[2] A. Pineau, S. Antolovich. High temperature fatigue of nickel-base superalloys–a review with special emphasis on deformation modes and oxidation [J]. *Engineering Failure Analysis*, 2009, 16(8): 2668-2697.

[3] W. Albert. Uber Treibseile am Harz. Archiv fur Mineralogie, Georgnosie [J]. *Bergbau und Huttenkunde*, 1837, 10: 215.

[4] J. Poncelet. Introduction à la mécanique industrielle, physique ou expérimentale [M]. : Thiel, 1839.

[5] F. Caron. Histoire des chemins de fer en France: 1883-1937. [J]. *Innovation*, 2005, 1(80): 11.

[6] S. Timoshenko. History of strength of materials: with a brief account of the history of theory of elasticity and theory of structures [M]. : Courier Corporation, 1953.

[7] W. Rankine. On the causes of the unexpected breakage of the journals of railway axles [C]. Minutes of the Proceedings of the Institution of Civil Engineers, 1843.

[8] A. Wöhler. Theorie rechtekiger eiserner Brückenbalken mit Gitterwänden und mit Blechwänden [J]. *Zeitschrift für Bauwesen*, 1855, 5: 121-166.

[9] A. Wöhler. Bericht über die Versuche, welche auf der Königl. Niederschlesisch-Märkischen Eisenbahn mit Apparaten zum Messen der Biegung und Verdrehung von Eisenbahnwagen-Achsen während der Fahrt angestellt wurden [J]. *Zeitschrift für Bauwesen*, 1858, 8(1858): 641-652.

[10] A. Wöhler. Über die Festigkeits-versuche mit Eisen und Stahl [M]. 1870.

[11] H. Gerber. Bestimmung der zulässigen spannungen in eisen-constructionen [J]. *Zeitschrift des Bayerischen Architekten und Ingenieur Vereins*, 1874, : 101-110.

[12] L. Spangenberg. Über das verhalten der metalle bei wiederholten anstrengungen, etc [M]. : Ernst & Korn, 1875.

[13] O. Basquin. The exponential law of endurance tests [J]. *Proceedings of the American Society for Testing and Materials*, 1910, 10(2): 625-630.

[14] J. Ewing, B. Humfrey. The fracture of metals under repeated alternations of stress [J]. *Phil Trans R Soc Lond A*, 1903, 200(321-330): 241-250.

[15] J. Ewing, W. Rosenhain. The crystalline structure of metals [J]. *Proceedings of the Royal Society of London*, 1900, 65(413-422): 172-177.

[16] M. Polanyi. Über eine Art Gitterstörung, die einen Kristall plastisch machen könnte [J]. *Zeitschrift für Physik*, 1934, 89(9-10): 660-664.

[17] G. Taylor. The mechanism of plastic deformation of crystals. Part I. Theoretical [J]. *Proceedings of the Royal Society of London Series A*, 1934, 145(855): 362-387.

[18] G. Taylor. The Mechanism of Plastic Deformation of Crystals. Part II. Comparison with Observations [J]. *Proceedings of the Royal Society of London Series A*, 1934, 145(855): 388-404.

[19] E. Orowan. Theory of the fatigue of metals [J]. *Proc R Soc Lond A*, 1939, 171(944): 79-106.

[20] N. Mott. A theory of the origin of fatigue cracks [J]. *Acta Metallurgica*, 1958, 6(3): 195-197.

[21] A. Head. The growth of fatigue cracks [J]. *The London, Edinburgh, and Dublin Philosophical Magazine and Journal of Science*, 1953, 44(356): 925-938.

[22] B. Langer. Fatigue failure from stress cycles of varying amplitude [J]. *Journal of applied mechanics*, 1937, 59: A160-A162.

[23] M.A. Miner. Cumulative damage in fatigue [J]. *Journal of applied mechanics*, 1945, 12(3): 159-164.

[24] G. Irwin. Analysis of stresses and strains near the end of a crack traversing a plate [J]. *J appl Mech*, 1957, : .

[25] D. Ryder. Some quantitative information obtained from the examination of fatigue fracture surfaces [J]. *Roy Aircraft Est, Tech Note Met*, 1958, 288.

[26] P. Paris. A rational analytic theory of fatigue [J]. *Trends Engin*, 1961, 13: 9-14.

[27] P. Paris, F. Erdogan. A critical analysis of crack propagation laws [J]. *Journal of basic engineering*, 1963, 85(4): 528-533.

[28] L. Coffin. Low Cycle Fatigue_ A Review [M]. : General Electric Co. Research Lab., Schenectady, NY, 1962.

[29] S. Manson. Fatigue Behavior in Strain Cycling in the Low and Intermediate Cycle Range [J]. *Fatigue-An Interdiscriplinary Approach, by burle, Reed and Weiss*, 1964, : 133-179.

[30] W. Elber. Fatigue crack closure under cyclic tension [J]. *Engineering Fracture Mechanics*, 1970, 2(1): 37-45.

[31] W. Elber. The significance of fatigue crack closure [J]. *Damage tolerance in aircraft structures*, 1971, : .

[32] S. Pearson. Initiation of fatigue cracks in commercial aluminium alloys and the subsequent propagation of very short cracks [J]. *Engineering Fracture Mechanics*, 1975, 7(2): 235-247.

[33] K. Miller. The short crack problem [J]. *Fatigue & Fracture of Engineering Materials & Structures*, 1982, 5(3): 223-232.

[34] T. Naito, H. Ueda, et al. Fatigue behavior of carburized steel with internal oxides and nonmartensitic microstructure near the surface [J]. *Metallurgical Transactions A*, 1984, 15(7): 1431-1436.

[35] C. Bathias. There is no infinite fatigue life in metallic materials [J]. *Fatigue and Fracture of Engineering Materials and Structures*, 1999, 22(7): 559-566.

[36] C. Bathias, L. Drouillac, et al. How and why the fatigue S–N curve does not approach a horizontal asymptote [J]. *International Journal of Fatigue*, 2001, 23, Supplement 1(0): 143-151.

[37] G. Hoskin, J. Provan, et al. The in-situ fatigue testing of a cast aluminum-silicon alloy [J]. *Theoretical and Applied Fracture Mechanics*, 1988, 10(1): 27-41.

[38] M. Buchanan, J. Provan, et al. An apparatus for four-point bending fatigue testing of materials in a scanning electron microscope and its application to nodular cast iron [J]. *Metallography*, 1987, 20(2): 125-143.

[39] W. Ludwig, J. Buffière, et al. Study of the interaction of a short fatigue crack with grain boundaries in a cast Al alloy using X-ray microtomography [J]. *Acta Materialia*, 2003, 51(3): 585-598.

[40] T. Marrow, J. Buffière, et al. High resolution X-ray tomography of short fatigue crack nucleation in austempered ductile cast iron [J]. *International Journal of Fatigue*, 2004, 26(7): 717-725.

[41] K. Khor, J. Buffière, et al. In situ high resolution synchrotron x-ray tomography of fatigue crack closure micromechanisms [J]. *Journal of Physics: Condensed Matter*, 2004, 16(33): S3511.

[42] K. Khor, J. Buffière, et al. High resolution X-ray tomography of micromechanisms of fatigue crack closure [J]. *Scripta Materialia*, 2006, 55(1): 47-50.

[43] A. Chrysochoos, H. Pham, et al. Energy balance of thermoelastic martensite transformation under stress [J]. *Nuclear Engineering and Design*, 1996, 162(1): 1-12.

[44] A. Chrysochoos, H. Louche. Analyse thermographique des mécanismes de localisation dans des aciers doux [J]. *Comptes Rendus de l'Académie des Sciences-Series IIB-Mechanics-Physics-Chemistry-Astronomy*, 1998, 326(6): 345-352.

[45] A. Chrysochoos, R. Peyroux. Analyse expérimentale et modélisation numérique des couplages thermomécaniques dans les matériaux solides [J]. *Revue générale de thermique*, 1998, 37(7): 582-606.

[46] A. Chrysochoos, H. Louche. An infrared image processing to analyse the calorific effects accompanying strain localisation [J]. *International journal of engineering science*, 2000, 38(16): 1759-1788.

[47] H. Xue, C. Bathias. Crack path in torsion loading in very high cycle fatigue regime [J]. *Engineering Fracture Mechanics*, 2010, 77(11): 1866-1873.

[48] C. Sonsino. Course of SN-curves especially in the high-cycle fatigue regime with regard to component design and safety [J]. *International Journal of Fatigue*, 2007, 29(12): 2246-2258.

[49] K. Asami, Y. Sugiyama. Fatigue strength of various surface hardened steels [J]. *Netsu Shori(J Jpn Soc Heat Treat)*, 1985, 25(3): 147-150.

[50] B. Claude, P. Paul. Gigacycle Fatigue in Mechanical Practice [M]. : CRC Press, 2004.

[51] W. Mason. Piezoelectric crystal and their application to ultrasonic [M]. : D. Van nostrand Company Inc, 1950.

[52] J. Tien, R. Gamble. The room temperature fatigue behavior of nickel-base superalloy crystals at ultrasonic frequency [J]. *Metallurgical Transactions*, 1971, 2(7): 1933-1938.

[53] S. Stanzl. A new experimental method for measuring life time and crack growth of materials under multi-stage and random loadings [J]. *Ultrasonics*, 1981, 19(6): 269-272.

[54] R. Morrissey, D. Mcdowell, et al. Frequency and stress ratio effects in high cycle fatigue of Ti-6Al-4V [J]. *International Journal of Fatigue*, 1999, 21(7): 679-685.

[55] S.A. Padula Ii, A. Shyam, et al. High frequency fatigue crack propagation behavior of a nickel-base turbine disk alloy [J]. *International Journal of Fatigue*, 1999, 21(7): 725-731.

[56] Q.Y. Wang, C. Bathias, et al. Effect of inclusion on subsurface crack initiation and gigacycle fatigue strength [J]. *International Journal of Fatigue*, 2002, 24(12): 1269-1274.

[57] B. Holper, H. Mayer, et al. Near threshold fatigue crack growth in aluminium alloys at low and ultrasonic frequency: Influences of specimen thickness, strain rate, slip behaviour and air humidity [J]. *International Journal of Fatigue*, 2003, 25(5): 397-411.

[58] L. Willertz. Ultrasonic fatigue [J]. *International metals reviews*, 1980, 25(1): 65-78.

[59] S. Stanzl, W. Hollanek, et al. Fatigue and fracture under variable-amplitude loading at ultrasonic frequency [C]. ICF6, New Delhi (India) 1984, 1984.

[60] C. Bathias. Piezoelectric fatigue testing machines and devices [J]. *International Journal of Fatigue*, 2006, 28(11): 1438-1445.

[61] H. French. Fatigue and the Hardening of Steels [J]. *Trans ASST*, 1933, 21: 899-946.

[62] C. Bathias, P. Paris. Gigacycle fatigue of metallic aircraft components [J]. *International Journal of Fatigue*, 2010, 32(6): 894-897.

[63] Q. Wang, J. Berard, et al. Technical note High‐cycle fatigue crack initiation and propagation behaviour of high‐strength sprin steel wires [J]. *Fatigue & Fracture of Engineering Materials & Structures*, 1999, 22(8): 673-677.

[64] A. Griffith, M. Eng. The phenomena of rupture and flow in solids [J]. *Phil Trans R Soc Lond A*, 1921, 221(582-593): 163-198.

[65] L. Kachanov. Time of the rupture process under creep conditions [J]. *Isv Akad Nauk SSR Otd Tekh Nauk*, 1958, 8: 26-31.

[66] N. Rabotnov. Creep problems in structural members [M]. : North-Holland Pub. Co., 1969.

[67] J. Lemaitre. How to use damage mechanics [J]. *Nuclear Engineering and Design*, 1984, 80(2): 233-245.

[68] J. Lemaitre. A continuous damage mechanics model for ductile fracture [J]. *Journal of engineering materials and technology*, 1985, 107(1): 83-89.

[69] J.L. Chaboche. Continuum damage mechanics: Present state and future trends [J]. *Nuclear Engineering and Design*, 1987, 105(1): 19-33.

[70] J.L. Chaboche. Continuum Damage Mechanics: Part I—General Concepts [J]. *Journal of applied mechanics*, 1988, 55(1): 59-64.

[71] J.L. Chaboche. Continuum damage mechanics: Part II—Damage growth, crack initiation, and crack growth [J]. *Journal of applied mechanics*, 1988, 55(1): 65-72.

[72] S. Antolovich, R. Armstrong. Plastic strain localization in metals: origins and consequences [J]. *Progress in Materials Science*, 2014, 59: 1-160.

[73] H. Mughrabi. Fatigue, an everlasting materials problem - still en vogue [J]. *Procedia Engineering*, 2010, 2(1): 3-26.

[74] H. Mughrabi. Specific features and mechanisms of fatigue in the ultrahigh-cycle regime [J]. *International Journal of Fatigue*, 2006, 28(11): 1501-1508.

[75] D.K. Felbeck, A.G. Atkins. Strength and fracture of engineering solids [J]. 1984, : .

[76] S. Suresh. Fatigue of materials [M]. : Cambridge university press, 1998.

[77] U. Essmann, U. Gösele, et al. A model of extrusions and intrusions in fatigued metals I. Point-defect production and the growth of extrusions [J]. *Philosophical Magazine A*, 1981, 44(2): 405-426.

[78] K. Differt, U. Esmann, et al. A model of extrusions and intrusions in fatigued metals II. Surface roughening by random irreversible slip [J]. *Philosophical Magazine A*, 1986, 54(2): 237-258.

[79] S. Nishijima, K. Kanazawa. Stepwise SN curve and fish-eye failure in gigacycle fatigue [J]. *Fatigue and Fracture of Engineering Materials and Structures*, 1999, 22(7): 601-608.

[80] T. Sakai. Review and prospects for current studies on very high cycle fatigue of metallic materials for machine structural use [J]. *Journal of solid mechanics and materials engineering*, 2009, 3(3): 425-439.

[81] K. Shiozawa, L. Lu, et al. S‑N curve characteristics and subsurface crack initiation behaviour in ultra‑long life fatigue of a high carbon‑chromium bearing steel [J]. *Fatigue & Fracture of Engineering Materials & Structures*, 2001, 24(12): 781-790.

[82] Y. Yu, J. Gu, et al. Very high cycle fatigue mechanism of carbide-free bainite/martensite steel micro-alloyed with Nb [J]. *Materials Science and Engineering: A*, 2009, 527(1-2): 212-217.

[83] Y. Yu, J. Gu, et al. Very high cycle fatigue behaviors of Mn–Si–Cr series Bainite/Martensite dual phase steels [J]. *Materials & Design*, 2010, 31(6): 3067-3072.

[84] Y. Yu, J. Gu, et al. Competition mechanism between microstructure type and inclusion level in determining VHCF behavior of bainite/martensite dual phase steels [J]. *International Journal of Fatigue*, 2011, 33(3): 500-506.

[85] K. Miller, W. O'donnell. The fatigue limit and its elimination [J]. *Fatigue and Fracture of Engineering Materials and Structures*, 1999, 22(7): 545-558.

[86] Z. Huang, D. Wagner, et al. Subsurface crack initiation and propagation mechanisms in gigacycle fatigue [J]. *Acta Materialia*, 2010, 58(18): 6046-6054.

154

[87] I. Marines-Garcia, P. Paris, et al. Fatigue crack growth from small to long cracks in VHCF with surface initiations [J]. *International Journal of Fatigue*, 2007, 29(9): 2072-2078.

[88] I. Marines-Garcia, P. Paris, et al. Fatigue crack growth from small to large cracks on very high cycle fatigue with fish-eye failures [J]. *Engineering Fracture Mechanics*, 2008, 75(6): 1657-1665.

[89] I. Marines-Garcia, P. Paris, et al. Fatigue crack growth from small to long cracks in very-high-cycle fatigue with surface and internal "fish-eye" failures for ferrite-perlitic low carbon steel SAE 8620 [J]. *Materials Science and Engineering: A*, 2007, 468–470: 120-128.

[90] Q. Wang, J. Berard, et al. Gigacycle fatigue of ferrous alloys [J]. *Fatigue & Fracture of Engineering Materials & Structures*, 1999, 22(8): 667-672.

[91] Y. Furuya, S. Matsuoka, et al. Gigacycle fatigue properties for high-strength low-alloy steel at 100 Hz, 600 Hz, and 20 kHz [J]. *Scripta Materialia*, 2002, 46(2): 157-162.

[92] E. Bayraktar, I.M. Garcias, et al. Failure mechanisms of automotive metallic alloys in very high cycle fatigue range [J]. *International Journal of Fatigue*, 2006, 28(11): 1590-1602.

[93] J. Yi, C. Torbet, et al. Ultrasonic fatigue of a single crystal Ni-base superalloy at 1000°C [J]. *Materials Science and Engineering: A*, 2007, 443(1–2): 142-149.

[94] G. Korth, G. Smolik. Status report of physical and mechanical test of alloy 718 [J]. *Report TREE*, 1978, : 1254.

[95] N. Kawagoishi, Q. Chen, et al. Fatigue strength of Inconel 718 at elevated temperatures [J]. *Fatigue and Fracture of Engineering Materials and Structures*, 2000, 23(3): 209-216.

[96] Y. Zhang, Z. Duan, et al. Comparison of the very high cycle fatigue behaviors of INCONEL 718 with different loading frequencies [J]. *Science China Physics, Mechanics and Astronomy*, 2013, 56(3): 617-623.

[97] M. Reger, L. Remy. High temperature, low cycle fatigue of IN-100 superalloy I: Influence of temperature on the low cycle fatigue behaviour [J]. *Materials Science and Engineering: A*, 1988, 101: 47-54.

[98] M. Reger, L. Remy. High temperature, low cycle fatigue of IN-100 superalloy II: Influence of frequency and environment at high temperatures [J]. *Materials Science and Engineering: A*, 1988, 101: 55-63.

[99] H. Lieurade. La pratique des essais de fatigue: méthodes expérimentales et analyse des résultats [M]. : Pyc édition, 1982.

[100]Reed, R. C. The superalloys: fundamentals and applications [M]. : Cambridge university press, 2008.

[101]M. Durand-Charre. The microstructure of superalloys [M]. : CRC press, 1998.

[102]http://www.specialmetals.com/assets/documents/alloys/inconel/inconel-alloy-718.pdf

[103]http://www.specialmetals.com/assets/documents/alloys/inconel/inconel-alloy-718spf.pdf

[104]J. Chaboche, D. Nouailhas, et al. Modeling of the cylic response and ratchetting effects on inconel-718 alloy [J]. *European journal of mechanics A Solids*, 1991, 10(1): 101-121.

[105]D. Jeong, M. Choi, et al. Effect of service exposure on fatigue crack propagation of Inconel 718 turbine disc material at elevated temperatures [J]. *Materials Characterization*, 2014, 95(0): 232-244.

[106]D. Fournier, A. Pineau. Low cycle fatigue behavior of inconel 718 at 298 K and 823 K [J]. *Metallurgical Transactions A*, 1977, 8(7): 1095-1105.

[107]Leo Prakash, M. Walsh, et al. Crack growth micro-mechanisms in the IN718 alloy under the combined influence of fatigue, creep and oxidation [J]. *International Journal of Fatigue*, 2009, 31(11–12): 1966-1977.

[108]M. Bache, W. Evans, et al. The effects of environment and loading waveform on fatigue crack growth in Inconel 718 [J]. *International Journal of Fatigue*, 1999, 21: S69-S77.

[109]A. Pineau. Mechanisms of creep-fatigue interactions [J]. *Advances in fatigue science and technology*, 1989, : 283-311.

[110]F. Alexandre, S. Deyber, et al. Modelling the optimum grain size on the low cycle fatigue life of a Ni based superalloy in the presence of two possible crack initiation sites [J]. *Scripta Materialia*, 2004, 50(1): 25-30.

[111]N. Yan, N. Kawagoishi, et al. Fatigue properties of Inconel 718 in long life region at elevated temperature [C]. Key Engineering Materials, 2003.

[112]Q. Chen, N. Kawagoishi, et al. Small crack behavior and fracture of nickel-based superalloy under ultrasonic fatigue [J]. *International Journal of Fatigue*, 2005, 27(10–12): 1227-1232.

[113]N. Kawagoishi, Q. Chen, et al. Fracture mechanism in fatigue of Nickel-based superalloy Inconel 718 at elevated temperatures [J]. *Journal of solid mechanics and materials engineering*, 2007, 1(6): 734-743.

[114]N. Kawagoishi. Effect of grain size on ultrasonic fatigue properties of Ni-base super alloy inconel 718 [J].   2008, : .

[115]N. Yan, N. Kawagoishi, et al. Effect of loading frequency on fatigue properties of Ni-base super alloy Inconel 718 [J]. *Structural Longevity*, 2010, 4(3): 145-152.

[116]X. Ma, Z. Duan, et al. Fatigue and fracture behavior of nickel-based superalloy Inconel 718 up to the very high cycle regime [J]. *Journal of Zhejiang University SCIENCE A*, 2010, 11(10): 727-737.

[117]M. Bruchhausen, P. Hähner, et al. Device for carrying out environmental very high cycle fatigue tests with ultrasonic excitation in asymmetric push–pull mode [J]. *International Journal of Fatigue*, 2013, 52(0): 11-19.

[118]M. Bruchhausen, B. Fischer, et al. Impact of hydrogen on the high cycle fatigue behaviour of Inconel 718 in asymmetric push–pull mode at room temperature [J]. *International Journal of Fatigue*, 2015, 70(0): 137-145.

[119]J. Belan. The Fractography Analysis of IN 718 Alloy after Fatigue Test [C]. Key Engineering Materials, 2014.

[120]J. Belan. High frequency fatigue test of IN 718 alloy–microstructure and fractography evaluation [J]. *Metalurgija*, 2015, 54(1): 59-62.

[121]A. Amanov, Y. Pyun, et al. Ultrasonic fatigue performance of high temperature structural material Inconel 718 alloys at high temperature after UNSM treatment [J]. *Fatigue & Fracture of Engineering Materials & Structures*, 2015, 38(11): 1266-1273.

[122]D. Texier, J. Cormier, et al. Crack initiation sensitivity of wrought direct aged alloy 718 in the very high cycle fatigue regime: the role of non-metallic inclusions [J]. *Materials Science and Engineering: A*, 2016, 678: 122-136.

[123]M.W. Tofique, J. Bergström, et al. Very high cycle fatigue crack initiation mechanisms in different engineering alloys [J]. *Procedia Structural Integrity*, 2016, 2: 1181-1190.

[124]A. Pineau, S.D. Antolovich. Probabilistic approaches to fatigue with special emphasis on initiation from inclusions [J]. *International Journal of Fatigue*, 2016, 93, Part 2: 422-434.

[125]J. Radavich. The physical metallurgy of cast and wrought alloy 718 [C]. Conference Proceedings on Superalloy, 1989.

[126]A. Oradei-Basile, J. Radavich. A current TTT diagram for wrought alloy 718 [J]. *Superalloys*, 1991, 718(625): 325-335.

[127]A. Thomas, M. El-Wahabi, et al. High temperature deformation of Inconel 718 [J]. *Journal of Materials Processing Technology*, 2006, 177(1): 469-472.

[128]I. Kirman, D. Warrington. The precipitation of Ni3Nb phases in a Ni−Fe−Cr−Nb alloy [J]. *Metallurgical Transactions*, 1970, 1(10): 2667-2675.

[129]Y. Huang, T. Langdon. The evolution of delta-phase in a superplastic Inconel 718 alloy [J]. *Journal of Materials Science*, 2007, 42(2): 421-427.

[130]A. Devaux, L. Nazé, et al. Gamma double prime precipitation kinetic in Alloy 718 [J]. *Materials Science and Engineering: A*, 2008, 486(1): 117-122.

[131]D. Texier, A. Gómez, et al. Microstructural Features Controlling the Variability in Low-Cycle Fatigue Properties of Alloy Inconel 718DA at Intermediate Temperature [J]. *Metallurgical and materials Transactions A*, 2016, 47(3): 1096-1109.